MICROSTRAIN PARTITIONING AND DAMAGE IN A QP980 STEEL

QUANTITATIVE ANALYSIS OF MICROSTRAIN PARTITIONING AND DAMAGE IN A COMMERCIAL QP980 AUTOMOTIVE STEEL

By

DIYAR SALEHIYAN, B. ENG.

A Thesis Submitted to the School of Graduate Studies in Partial Fulfillment of the Requirement for the Degree Master of Applied Science

McMaster University © Copyright by Diyar Salehiyan, September 2018

Master of Applied Science (2018) McMaster University

(Materials Science and Engineering) Hamilton, Ontario, Canada

TITLE	Quantitative Analysis of Microstrain Partitioning and Damage in a Commercial QP980 Automotive Steel
AUTHOR	Diyar Salehiyan, B.Eng. (Amirkabir University of Technology)
SUPERVISOR	Professor David S. Wilkinson
NUMBER OF PAGES	xx, 137

Abstract

Over the past decade, environmental concerns and safety regulation have led to increasing demand for vehicles with higher passenger safety and fuel economy. This has spurred intensive research on advanced high strength steels (AHSS). The quench and partitioning (Q&P) heat treatment is a novel approach that has led to development of one group of third generation AHSS alloys. In recent years most of the studies on the Q&P process were dedicated to the effect of the heat treatment parameters on microstructural evolution and mechanical properties. However, micromechanical deformation behavior of constituent phases and damage evolution in Q&P steels are not fully understood. In this study, damage micromechanisms in a commercial QP980 were investigated with the aid of in-situ tensile tests under a scanning electron microscope (SEM) followed by local strain mapping using microscopic digital image correlation (μ-DIC) analysis so as to quantify the microstructural deformation of constituent phases. Nano-hardness measurements were conducted to correlate the amount of plastic deformation of each phases to its strength. Ex-situ tensile tests coupled with electron back scattered diffraction (EBSD) and X-ray diffraction (XRD) were conducted to study the influence of transformation induced plasticity (TRIP) of the retained austenite phase on microstructural damage and deformation.

It was found that average local true strain in ferrite was approximately two times and three times greater than that of martensite and blocky retained austenite respectively, which was with the good agreement with nano-hardness measurements showing that

retained austenite blocks was three times and two times harder than martensite and ferrite respectively. Damage in both ferrite and martensite starts at the same total strain; however, damage growth is faster in martensite leading to the formation of large cavities. The average local true strain ratio of ferrite to martensite decreases after total true strains higher than 0.1 and the reduction is more pronounced in regions with higher martensite volume fraction. EBSD results showed that at total true strain of 0.07 some of the retained austenite blocks located at the ferrite and martensite interfaces were almost fully transformed to martensite. According to XRD results at the point of necking 57% of retained austenite transformed to martensite. There is evidence of brittle cracking of large blocky retained austenite in regions with strain localization starting at relatively low strains but appear to have little impact on the final failure process. The good deformation ability of QP980 is attributed primarily to co-deformation of ferrite and martensite and secondarily to the TRIP effect.

Acknowledgement

To begin with, I would like to express my gratitude to my supervisor Dr. David S. Wilkinson for his invaluable guidance, patience, expertise, constructive feedbacks during group meetings and his positive supervisory attitude that gave me freedom to pursue my own ideas.

I am deeply grateful to Dr. Javad Samei for his valuable suggestions, discussions and patience to bear with me throughout this work.

I also would like to thank the following people:

- Ms. Victoria Jarvis for XRD measurements at Brockhouse Institute for Materials Research
- Mr. Chris Butcher for SEM training at Canadian Center for Electron Microscopy
- Mr. Andy Dulf for SEM tensile tester Maintenance
- Ms. Linfeng Zhou for SEM in-situ tensile test training
- Dr. Michael Bruhis for mechanical testing and ARAMIS software training
- Mr. Jim Cleaver for machining the samples at the Faculty of Engineering Machine shop
- Mr. Douglas Culley and Mr. Xiaogang Li for at MSE labs
- Dr. Elizabeth McNally for her assistance at McMaster Automotive Research Center

I especially want to thank my family for their support and encouragement to pursue my goals and my best friend, Mr. Mukesh Sharma, for the fun moments, memorable experiences, useful talks and the lunch breaks.

Table of content

List of figures

List of tables

List of abbreviations

AFM	Atomic Force Microscopy
AHSS	Advance High Strength Steel
APT	Atom probe tomography
CC	Cross Correlation
CP	Complex Phase
CPE	Constrained Paraequilibrium
DIC	Digital Image Correlation
DP	Dual Phase
FIB	Focus Ion Beam
LSCM	Laser Scanning Confocal Microscopy
MART	Martensitic
MEMS	Microelectromechanical
NN	Number of Nearest Neighbor
OIM	Orientation Image Microscopy
OPS	Colloidal Silica Suspension
Q&P (QP)	Quench and Partitioning
RD	Rolling Direction
ROI	Region of Interest
SEM	Scanning Electron Microscopy

SIP	Shear Band Strengthened
SSD	Sum Squared Difference
STM	Scanning Tunneling Microscope
TD	Transverse Direction
TRIP	Transformation Induced Plasticity
TWIP	Twinning Induced Plasticity
UM	Untempered Martensite

1 Introduction:

In recent years there have been lots of interest to improve vehicles fuel efficiency and occupant safety as automakers are challenged to satisfy environmental concerns and safety regulations. This has led to intensive research and development related to advanced high strength steels (AHSS) (1-6).

Transformation induced plasticity (TRIP) steels, low alloy dual phase (DP) steels, martensitic (MART) steels and complex phase (CP) steels and are among the first-generation advanced high strength steels which have been successfully implemented in body-in-white. Their microstructures are primary ferritic-based (7-10). Tensile property combinations (i.e. strength and ductility) of different generations of AHSS can be compared using uniform elongation vs. ultimate tensile strength chart based on tensile tests, as shown in Figure 1-1 (9).

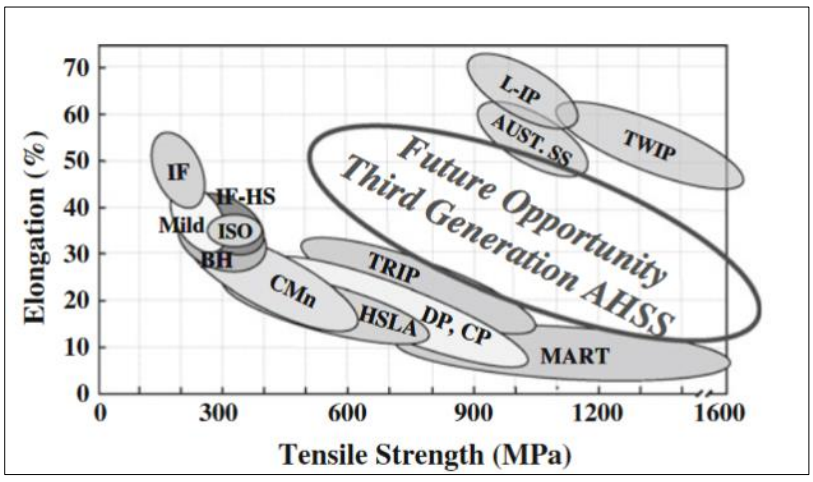

Figure 1-1 Elongation/tensile strength combination for various generation of advanced high strength steels (9).

The second generation of AHSS alloys includes highly alloyed products such as twinning induced plasticity (TWIP) steels, shear band strengthened (SIP) steels and Al-added light weight steels (7, 9, 10). They provide enhanced combinations of strength and ductility as they are located towards the upper right portion of the uniform elongation-tensile strength chart (Figure 1-1). However, their applications are limited due to the high cost associated with their processing and the increased amount of alloying required (7, 9, 10).

Third generation AHSS alloys emerged to provide a lower cost alternative to the second generation steels due to their reduced alloying content; while still possessing significantly higher combinations of strength and ductility than first generation AHSS steels (7, 9-11). Quench and partitioning (Q&P) steels, ultra-fine DP steels, carbide free bainite, super bainite steels and modified TRIP steels are classified as third generation AHSS as they possess minimum uniform elongation and tensile strength which can satisfy the requirements of third generation of AHSS as depicted in Figure 1-1 (9). Combination of retained austenite and martensite can produce a desired microstructure to obtain the required mechanical properties to satisfy the third generation AHSS criteria (9).

The Q&P heat treatment is an innovative and promising approach that has led to the development of third generation steels with a superior combination of strength and ductility (12). In 2003, the Q&P heat treatment concept was first proposed by Speer et.al (13). In 2012, a Q&P steel with ultimate strength of 980 MPa (QP980) was successfully

commercialized by Bao Steel Corporation (13). Figure 1-2 shows a B-pillar reinforcement made from QP980 steel.

Figure 1-2 B-pillar reinforcement made from QP980 steel (13).

Q&P heat treatment can be applied to a wide range of steels in order to stabilize austenite at room temperature (14). Figure 1-3 shows schematic illustration of Q&P heat treatment and carbon content evolution of retained austenite during Q&P process.

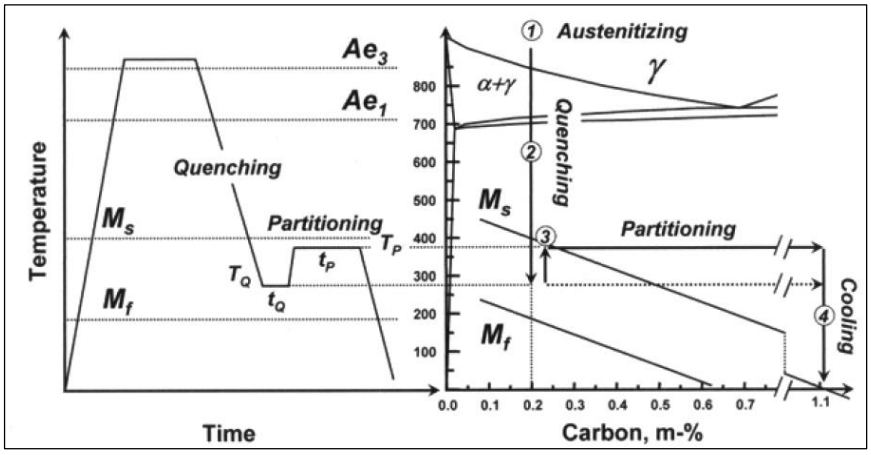

Figure 1-3 Schematic illustration of Q&P heat treatment and carbon content evolution of retained austenite (15).

It starts with full or partial austenitization followed by a first quench to a temperature between M_s and M_f to obtain a specific amount of austenite and martensite. The material is then subjected to an isothermal heat treatment at the same or higher

temperature which allows carbon partitioning from martensite to untransformed austenite in the absence of carbide precipitation. Finally, the material is quenched or cooled to room temperature to obtain carbon enriched retained austenite and carbon depleted martensite (16-18). The final microstructure contains martensite, retained austenite, ferrite (in the case of intercritical annealing) and bainite if the partitioning temperature is located close to bainitic transformation temperature (19).

It is well-known that mechanical properties depend on micromechanical behavior of the constituent phases, e.g. ferrite, martensite and retained austenite in the Q&P steels. Among the AHSS most of the research works have been conducted on micromechanical behavior and damage mechanisms of DP steels (20-26). However, there is a lack of understanding in micromechanical behavior of the constituent phases in Q&P steels since most of studies on Q&P steels have been focused on optimizing the processing parameters such as the effect of quenching temperature, partitioning time and temperature on microstructural evolution and mechanical properties (14, 27-30). Therefore, the aim of the current study is to investigate damage micromechanisms in a commercial QP980 steel using in-situ tensile tests coupled with scanning electron microscopy (SEM) followed by quantification of microstructural deformation using digital image correlation (DIC). Ex-situ tensile tests coupled with EBSD and XRD were used to investigate the TRIP effect in QP980 steel. Nano-hardness measurements were performed to correlate the strength of each phase to the amount of plastic deformation measured using DIC.

The following layout is adopted in this thesis: Chapter 2 presents fundamentals of the Q&P process and reviews studies on the effect of Q&P heat treatment parameters and alloying elements on the microstructure and mechanical behavior of these steels, mechanical stability of retained austenite, background of damage micromechanisms in advance high strength steels and basic concepts of the DIC method. Chapter 3 describes the experimental approaches used in this research. Chapter 4 presents the the results achieved along with a discussion of their significance. Finally, chapter 5 summarizes the main findings of this research.

2 Literature review:

In this section, fundamentals of Q&P heat treatment including constrained paraequilibrium is discussed. Studies on the alloying effect, Q&P heat treatment parameters that affect the mechanical properties and final microstructure of the Q&P steels and mechanical stability of retained austenite are reviewed. Background on damage micromechanisms in advanced high strength steels and most importantly, DP steels is presented. Finally, basic concepts of the 2D DIC method is presented.

2.1 Quench and partitioning heat treatment

2.1.1 Constrained paraequilibrium:

Constrained paraequilibrium (CPE) is based on a model developed by Speer et al. (31) to calculate the endpoint for carbon partitioning between martensite and untransformed austenite in the absence of carbide precipitation (primarily transition metal carbides and cementite). Other reactions that compete with carbon partitioning such as carbon trapping at dislocations or interfaces in martensite are not considered in this model. In other words, all the carbon in martensite is available to stabilize austenite at room temperature. Austenite decomposition to bainite is also restricted. This model assumes that in the presence of slow diffusing substitutional atoms such as Si, the ratio of iron to substitutional elements in each phase i.e., martensite and untransformed martensite, is fixed. Thus, there is a stationary interface between them and there is no change in martensite and austenite fraction during carbon partitioning. Once the endpoint is reached, carbon diffusion between the two phases

is completed and there is no carbon chemical potential gradient. The term paraequilibrium refers to the fact that this model cannot satisfy the orthoequilibrium condition in which chemical potential of iron is the same in both phases (as shown in Figure 2-1) and the term constrained refers to stationary interface of the two phases (31).

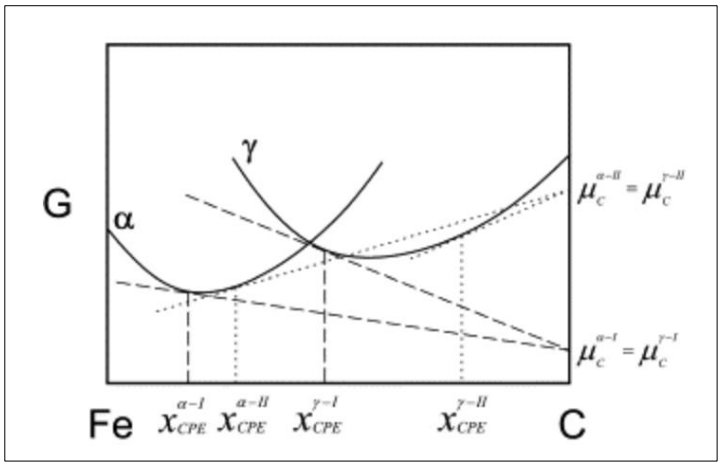

Figure 2-1 Gibbs free energy versus chemical composition diagram depicting two series of ferrite and austenite chemical compositions obeying carbon paraequlibrium condition as they have same carbon chemical potential but different iron chemical potential (31).

Optimum quenching temperature can be predicted with the aid of this model where the retained austenite volume fraction is maximized using the following procedure. First, volume fraction of martensite and austenite is calculated using the Koistinen–Marburger relationship (32) at the quenching temperature determined according to equation (2-1):

$$f_m = 1 - e^{-1.1\times10^{-2}(M_s - QT)} \qquad (2\text{-}1)$$

Where f_m is the austenite fraction that transforms to martensite, QT is the quenching temperature and M_s is martensite start temperature. M_s can be estimated using published correlations such as equation (2-2) (33):

$$M_s(°C) = 539 - 423C - 30.4Mn - 7.5Si + 30Al \qquad (2\text{-}2)$$

where the alloy levels are in wt%.

In the case of intercritical annealing it can be assumed that all the carbon is in austenite prior to the initial quenching step since the solubility of carbon in ferrite is very low. Then M_s temperature and austenite volume content are calculated again using the final carbon content of the partitioned austenite obtained from the CPE model and it should satisfy the condition that no fresh martensite forms and all the austenite is stabilized at room temperature (17).

At quenching temperatures above the optimum quenching temperature, significant amount of untransformed austenite remains at the partitioning step however carbon migration from lower volume of martensite is insufficient for austenite stabilization at room temperature. This leads to formation of so-called fresh martensite during the second quench which is not desirable. On the other hand, initial quenching to temperatures below the optimum quenching temperature results in low volume fraction of austenite at the first quenching step which even in a case of a successful partitioning process, leads to lower retained austenite volume fraction after the second quench to room temperature. Quenching to the optimum quenching temperatures leads to the correct amount of martensite to enrich

the untransformed austenite to the carbon level that yields the maximum volume fraction of retained austenite after the final quenching step by reducing the M_s temperature to room temperature (17).

2.1.2 Effect of alloying elements on the Q&P steels properties

Carbon, Silicon and Manganese are the main alloying elements needed in Q&P Steels. As mentioned in the section 2.1.1, silicon is a critical alloying element that prevents carbide precipitation during partitioning. High amount of silicon in AHSS produces a highly stable adherent oxide layer during rolling that causes surface finish problems during hot dipping which is known as the bare-spot defect (34). Aluminum as an alternative to silicon can be used to prevent carbide precipitation (35) since it shows a lower tendency to produce an oxide layer that degrades surface wettability during zinc coating (9). However, aluminum is less effective than silicon to prevent carbide precipitation and it is found to promote austenite decomposition to bainite. Manganese and carbon lead to austenite stabilization by lowering the M_s temperature and they also increase the hardenability. Molybdenum is found to delay the austenite decomposition process kinetics (36).

De Moor et al. (37, 38) conducted Q&P heat treatments on three different CMnSi steels with chemical compositions of Fe-0.2C-3Mn-1.6Si, 0.3C-3Mn-1.6Si, and Fe-0.2C-5Mn-1.6Si to investigate effect of carbon and manganese variation on mechanical properties of the Q&P steels. Quenching temperatures, partitioning temperatures and

partitioning times were between 70-250°C, 400-450°C and 10-100 s respectively. Both intercritical annealing and full austenitization were performed on the steels. The results are summarized in the Figure 2-2.

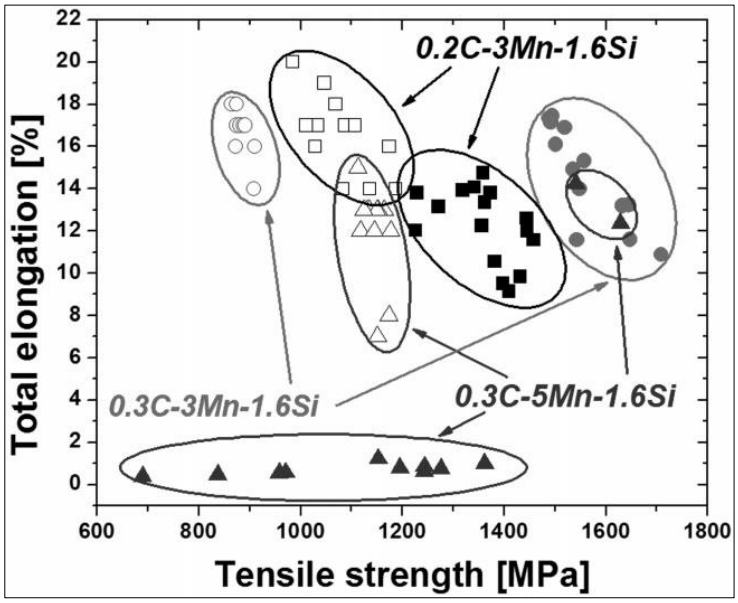

Figure 2-2 Total elongation/tensile strength properties for samples with different chemical compositions subjected to Q&P process with the initial full austenitization (solid symbol) or initial intercritical annealing (open symbol) (37).

According to the total elongation-tensile strength graph (Figure 2-2), in the case of intercritical annealing, addition of carbon and manganese led to decreasing of total elongation without increasing tensile strength; however, addition of carbon in the case of full austenitization increased both elongation and tensile strength. Addition of manganese in that case caused degradation of elongation which the authors suggested may be related to high fraction of un-tempered martensite or fresh martensite. They concluded that novel

properties can be obtained from 0.2C-3Mn-1.6Si and 0.3C-3Mn-1.6Si steels after full austenitization and they mentioned that there is a need to better understand the structure/property relationship in Q&P steels and optimize the quench and partitioning parameters for the 0.3C-5Mn-1.6Si sample (37, 38).

Twin substructure is usually observed in lenticular martensite in high carbon and medium carbon steels. However, the formation of lath martensite with twin substructure has been reported after Q&P heat treatment of low carbon steel (7, 39). Lath martensite with the twin substructure describes the morphology of isothermal martensite. Isothermal martensite can form in three ways, i.e., nucleation and growth in retained austenite, growth of pre-existing athermal martensite and nucleation and growth beside athermal martensite (40). It can be concluded that if the carbon enrichment of retained austenite is not enough for its stabilization at room temperature it can transform to lath martensite with twin substructure or so called fresh martensite (7, 39).

Mahesvari et al. (41) subjected three alloys with different variations of C-Si-Mn and Al to Q&P heat treatment in order to investigate effect of alloying elements on the mechanical properties and microstructural evolution in Q&P steels. All the samples were full austenitized at 1060/1000 °C for 1 h. Quenching temperature, partitioning temperature and partitioning time were 240°C, 350°C and 60 s respectively. They studied the microstructure using transmission electron microcopy (TEM) and measured retained austenite volume fraction before and after fracture using XRD. Chemical compositions of the steels are listed below:

Table 2-1 Chemical composition of the samples subjected to Q&P heat treatment.

Notation	C	Mn	Si	Al
Steel A	0.29	1.22	1.65	1.62
Steel B	0.26	1.57	1.06	0.98
Steel C	0.22	1.85	0.41	1.46

Engineering stress-strain curves for the three samples are shown in Figure 2-3.

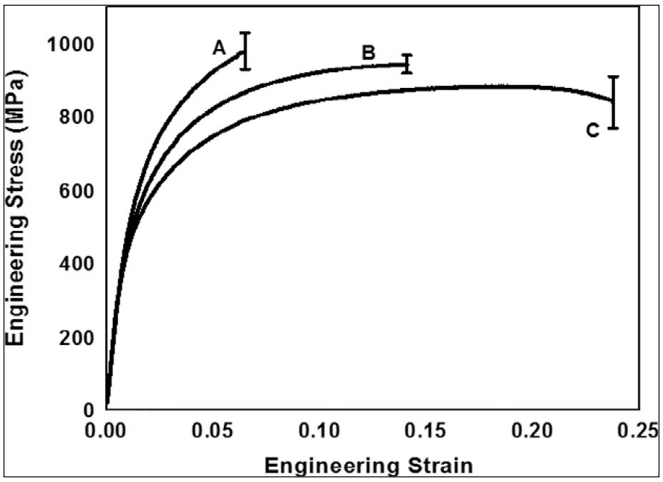

Figure 2-3 Engineering stress-strain curves for the samples with different variation of chemical composition subject to Q&P heat treatment (41).

The authors reported that sample A with higher amount of Carbon, Silicon and Aluminum and lower amount of Manganese showed higher ultimate strength but lower elongation with brittle fracture characteristics. They related the higher strength to the Hall-Petch effect due to the small lath thickness, refined martensite colony size and high

contiguity of martensite phase. They suggested that low ductility happened because of low stability of blocky retained austenite and its early transformation to martensite where the austenite retention was 50 percent. Sample C showed good combination of strength and ductility compared to other steels. They related the improved properties in Steel C to higher fraction of interlath film-type austenite present in the microstructure, small austenite grain size and refinement of lath thickness and martensite colony size. The austenite retention was reported to be 60 percent for steel C. The steel B tensile strength and elongation ranged between those of steel A and C. They reported that lower contiguity value compared to Steel C and possibly the austenite morphology can be responsible for Steel B properties (41).

Nayak et al. (8) performed Q&P heat treatment on a set of medium carbon and high carbon steels with different variation of chromium, manganese and silicon to enhance their understanding of Q&P process. They reported that increasing silicon content in medium carbon steel led to transitional carbide precipitation. Figure 2-4 shows a TEM micrograph of the medium carbon steel with 1.5 and 1.7 wt. % silicon content quenched and held at 100°C and 200 °C for 20 s respectively and then partitioned at 350 °C for 10 s and 250 °C for 60 s (8).

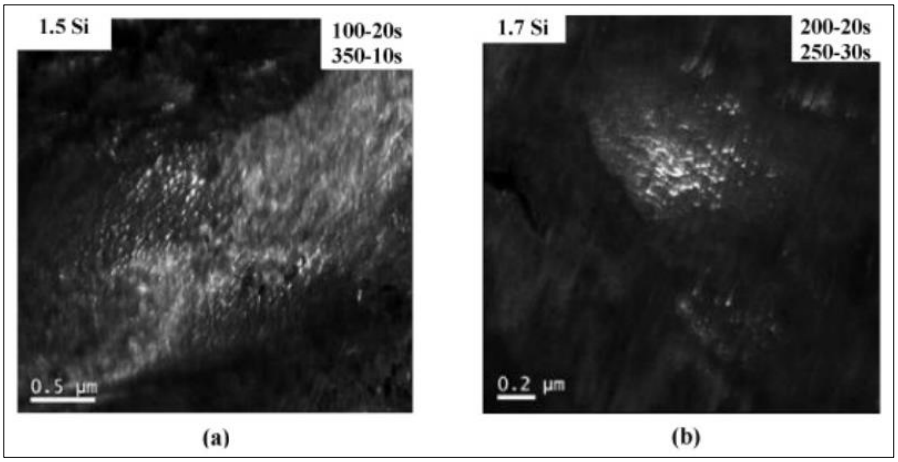

Figure 2-4 Dark field micrograph obtained using (0 2 0) ε-carbide reflection for the sample a) containing 1.5% Si, quenched at 100 °C, held for 20 s and subjected to partitioning heat treatment at 350°C for 10 s and b) containing 1.7% Si, quenched at 200 °C, held for 20 s and subjected to partitioning heat treatment at 250 °C for 30 s (8).

As observed from Figure 2-4, even with lowering the partitioning temperature and increasing the quenching temperature in order to decrease the initial martensite volume content, the transitional carbide was formed in the microstructure which indicated the shift in epsilon carbide time-temperature-transformation (T-T-T) curve to a lower temperature (8).

Despite the fact that silicon can retard the formation of cementite during martensite tempering, it can lead to stabilization of epsilon carbide (17). The suppression of cementite precipitation is usually explained by the rejection of silicon into surrounding ferrite due to its low solubility in cementite and slowing down the reaction kinetics (17, 42). Higher solubility of silicon in transitional carbide was thought to be the reason for epsilon carbide precipitation in the presence of silicon during tempering; however, atom probe tomography

(APT) investigations have not shown a high enrichment level of silicon in transitional carbide (17).

2.1.3 Effect of heat treatment parameters on microstructure and mechanical properties of Q&P steels:

In recent years, most of the studies on Q&P steels have been focused on the investigation of quenching and partitioning heat treatment parameters including quenching temperature, cooling rate, partitioning temperature and time on the mechanical properties and microstructural evolution during thermomechanical processing. In this section some of these studies are briefly presented.

Zhong et al. (43) obtained 1500 MPa tensile strength with 15% elongation by subjecting an Fe–0.2C–1.5Mn–1.5Si–0.05Nb–0.13Mo steel to Q&P and tempering heat treatment process. Figure 2-5 shows the influence of partitioning-tempering time on the mechanical properties of the steel.

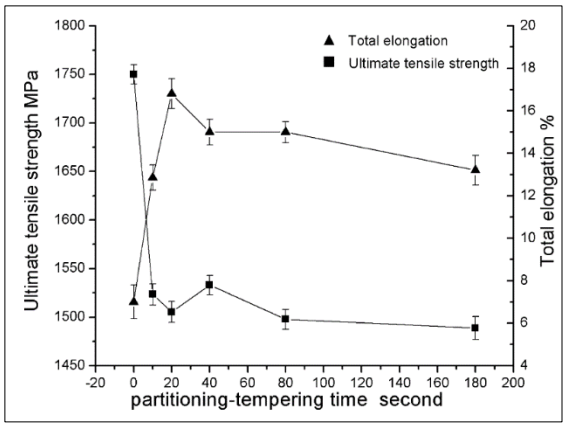

Figure 2-5 Ultimate tensile strength (UTS) and total elongation of Nb microalloyed steel as a function of partitioning-tempering time (43).

As it is shown in the Figure 2-5, tensile strength and elongation of the as-quenched sample was 1750 MPa and 7% respectively. After partitioning for 20 s the UTS of the steel dropped to 1500 MPa; however, there was a significant improvement of elongation to 17 %. With further isothermal heat treatment by the so-called partitioning-tempering process the tensile strength increased to 1550 MPa and elongation decreased to 15%. This was confirmed by TEM investigation to be the result of carbide precipitation strengthening. Further partitioning-tempering heat treatment up 180s led to degradation of both tensile strength and elongation of the steel (43).

Santomifia et al. (35) studied the achieved microstructure from a Q&P heat treatment with an initial annealing step on a low carbon steel. They reported that the obtained volume fraction of ferrite was approximately two times greater than the value calculated using thermodynamic databases (MTDATA). They attributed this discrepancy

to the formation of epitaxial ferrite due to an inappropriate cooling rate of 100 °C/s. They reported that even though epitaxial ferrite formation led to decrease in austenite volume fraction, it increased the austenite carbon content which led to its retention at room temperature. Figure 2-6 shows carbon content in retained austenite (measured with XRD) versus partitioning time for different partitioning temperatures. Maximum carbon content at 175 °C, 150 °C and 125 °C achieved after 100 s, 10 s and 3 s respectively which indicates the faster retained austenite carbon enrichment at higher temperature due to faster carbon partitioning. The decrease in carbon content after the maximum value was related to the carbide precipitation and segregation during the partitioning step (35).

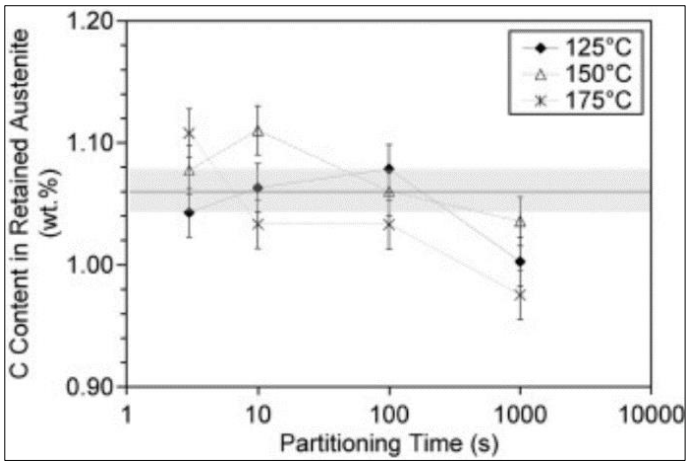

Figure 2-6 Retained austenite carbon content versus partitioning time for the samples subjected to partitioning heat treatment at various temperatures (35).

Zhang et al. (44) studied the effect of pre-quenching heat treatment before Q&P process on microstructure and mechanical properties of a steel with chemical composition of Fe-0.18C-1.48Si-1.44Mn-0.15Al-0.025Nb. Pre-quenched samples were subjected to

first quenching from 900 °C to room temperature and then Q&P heat treatment started from intercritical annealing at 850 °C for 3 min followed by quenching to 220 °C. Samples were partitioned at 400 °C for a duration ranging from 5 to 500 s and quenched to room temperature. The same Q&P heat treatment, without the pre-quench, was performed on the second group of samples.

The authors reported that the pre-quenching step led to finer microstructure and higher volume fraction of retained austenite that resulted in higher ultimate strength and elongation compared to the samples without pre-quenching step as shown in Figure 2-7.

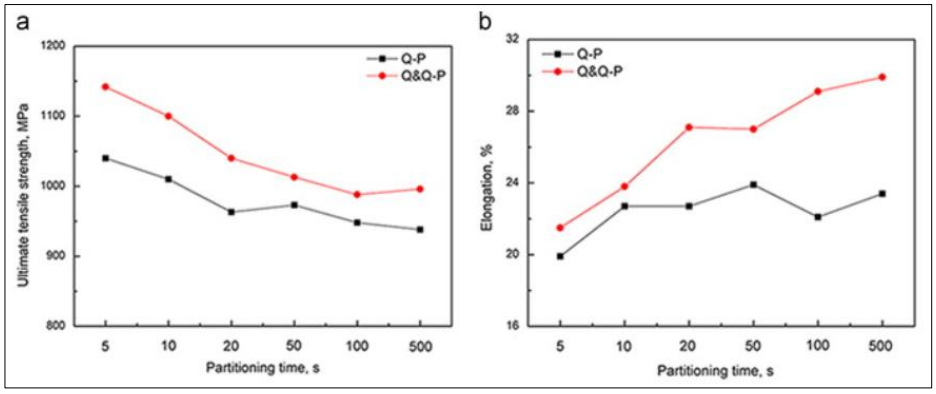

Figure 2-7 Comparison of tensile properties achieved with Q&P and Q-Q&P heat treatment. a) UTS versus partitioning time, b) Elongation versus partitioning time (44).

Sun et al. (11) studied microstructural evolution during Q&P heat treatment on a TRIP steel with a chemical composition of Fe–0.2C–1.5Si–1.9Mn. Figure 2-8 shows dilatometry curves for the samples quenched at different temperatures and subjected to a partitioning heat treatment at 400 °C for 1000 s.

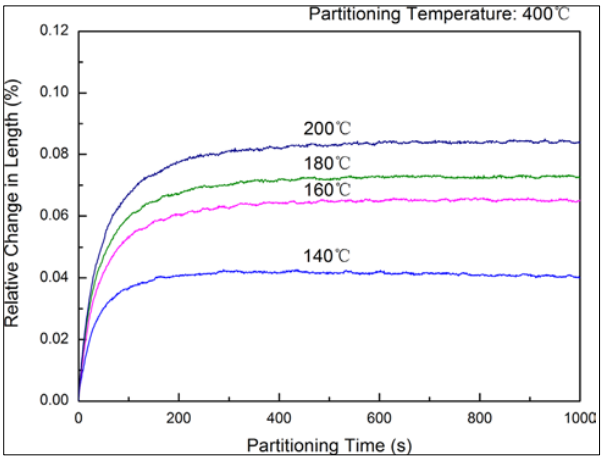

Figure 2-8 Dilatometry curves of the samples quenched at different temperatures and partitioned at 400 °C for 1000 s (11).

As observed from Figure 2-8, samples quenched at the higher temperature showed higher volume expansion which was related to higher volume fraction of untransformed austenite that transformed to bainite during the partitioning step. SEM micrographs confirmed the formation of bainite in the microstructure in preliminary stage of partitioning step (11).

Clarke et al. (45) performed Q&P heat treatment on a steel with chemical composition of Fe-0.19C–1.59Mn–1.63Si–0.036Al. Samples were intercritically annealed at 820 °C for 180 s, quenched to temperatures between 200-260 °C, held for 10 s and partitioned at 400 °C for 10, 30, 100, 1000 s. Figure 2-9 shows austenite volume fraction and carbon content measured with XRD versus partitioning time for samples quenched at different temperatures. Results showed that samples quenched at 260 °C reached the retained austenite volume fraction maximum value after partitioning for 100 s while the

maximum value for the sample quenched at 240 °C was obtained after partitioning for 10 s. This confirms that optimum partitioning time depends on quenching temperature or initial volume fraction of retained austenite. After 1000 s there was a significant reduction in retained austenite volume fraction which was related to effect of carbide precipitation and austenite decomposition to ferritic bainite. Maximum carbon level for all the samples with different quenching temperatures were reached after 100 s as shown in Figure 2-9 (45). In the opinion of this thesis author, this can be related to ignoring the effect of bainite formation on the enrichment of austenite during 100 s and 1000 s. Including more data points between 100 s to 1000s can change the corresponding partitioning time for the maximum carbon level of samples quenched at higher temperature.

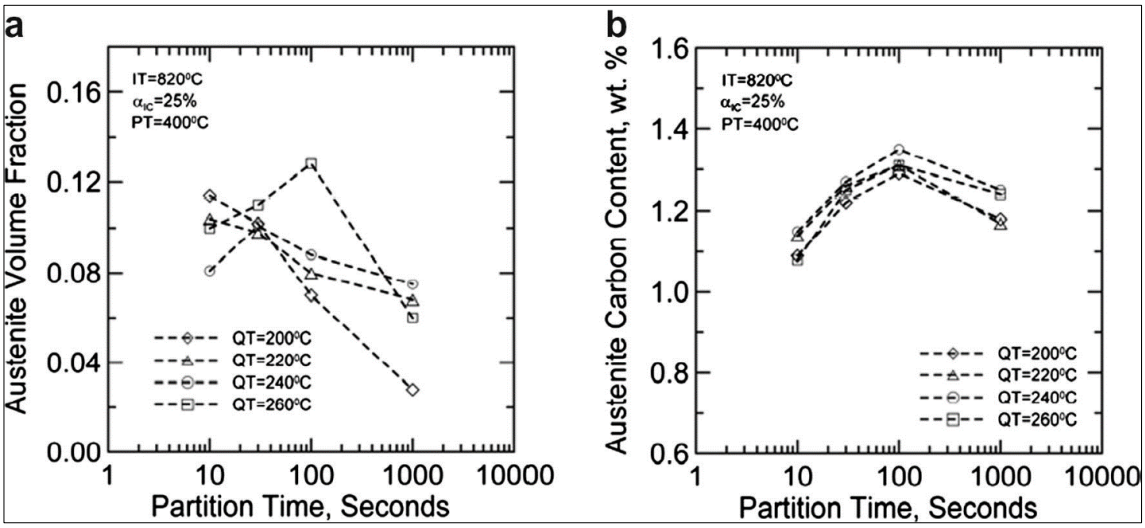

Figure 2-9 a) austenite volume fraction versus partitioning time and b) austenite carbon content wt.% versus partitioning time measured with XRD for the samples initially quench into various temperatures (45).

Li et al. (46) studied bainite transformation during Q&P heat treatment of a steel with chemical composition of Fe-0.41C-1.27Si-1.30Mn-1.01Ni-0.56Cr. Q&P heat treatment parameters included full austenitization at 820 °C for 10 s, first quench to 180 °C and hold for 60 s, partitioning treatment at the temperature of 300 °C for 10–900 s and finally last quench to room temperature.

They divided the partitioning process into three stages based on the changes of the mechanical properties during the above mentioned two step Q&P heat treatments as shown in Figure 2-10 (46).

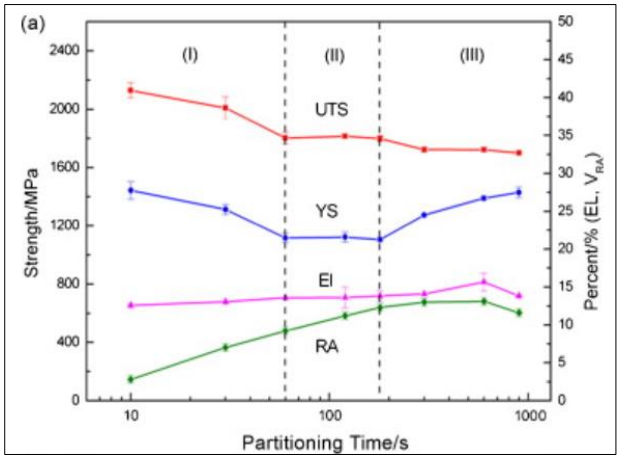

Figure 2-10 Variation of tensile properties and retained austenite volume fraction with partitioning time at partitioning temperature of 300 °C (46).

In the first stage of partitioning process (between 10-60 s) there was a noticeable increase in volume fraction of retained austenite (from 2.8 to 9.2 %); however, yield strength and ultimate strength decreased which was attributed to softening of martensite due to the reduction in martensite carbon supersaturation and carbon migration into

untransformed austenite. According to their SEM investigation very little austenite decomposition to bainite and carbide precipitation was observed in this stage and the effect of bainite formation on carbon enrichment of austenite was negligible (46).

In the second stage of partitioning process (between 60-180 s), yield strength and tensile strength of steel was almost constant and there was a slight increase in retained austenite volume fraction. They suggested that thermal stabilization of retained austenite happened not only due to the carbon partitioning but also due to the austenite decomposition to bainite that counteracted the effect of martensite softening during partitioning step and led to stable trend in UTS and yield strength (46).

In the third stage of partitioning process (between 180-900 s), UTS started to degrade again however yield strength started to increase and retained austenite volume fraction decreased. They related the increase in yield strength and decrease in UTS to the rapid increase in bainite volume fraction and to the carbon depletion of martensite respectively. They mentioned that carbon homogenization of austenite happens in this stage (46).

2.1.4 Mechanical stability of retained austenite

Mechanical stability of retained austenite has a great influence on the mechanical properties of advanced high strength steel. Here mechanical stability is defined as the resistance of retained austenite to the TRIP effect under the influence of stress (47). If

retained austenite is too stable it does not transform and therefore cannot contribute to work hardening which is critical to protect the steel against the necking instability. On the other hand, if TRIP occurs at small plastic strain it also does little to enhance work hardening (48). Figure 2-11(a) shows predicted uniform elongation versus tensile strength for the ferrite and austenite mixture based on the different hypothetical mechanical stability of retained austenite shown in Figure 2-11(b). Low stability of retained austenite (condition D) leads to mechanical properties similar to ferrite and martensite mixture located out of third generation advanced high strength steel region as depicted in Figure 2-11-a) (9).

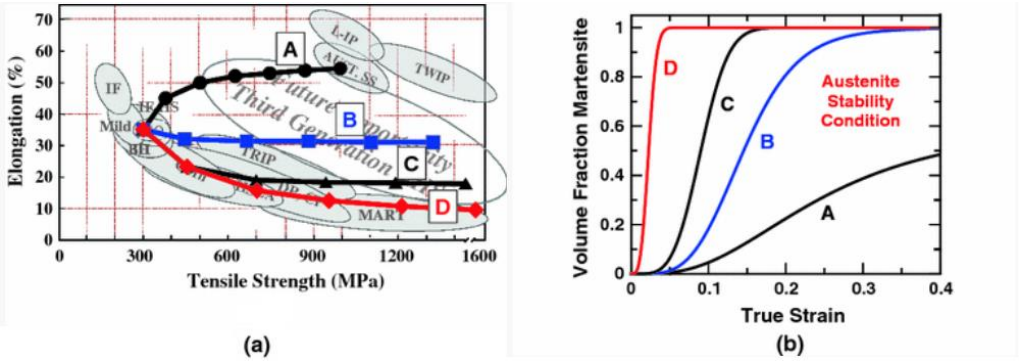

Figure 2-11 a) Predicted combinations of uniform elongation/ tensile strength for different mechanical stability of retained austenite shown in b)austenite stability as a function of true strain (9).

Sun et al. (7) categorized retained austenite morphology into three types as shown in Figure 2-12. First morphology includes film-like retained austenite with approximately 100 nm width existing between martensite laths. Second morphology includes retained austenite blocks dispersed in the ferrite matrix and third morphology is retained austenite

films of 20-30 nm thickness located between bainitic ferrite in carbide-free bainite microstructure (7).

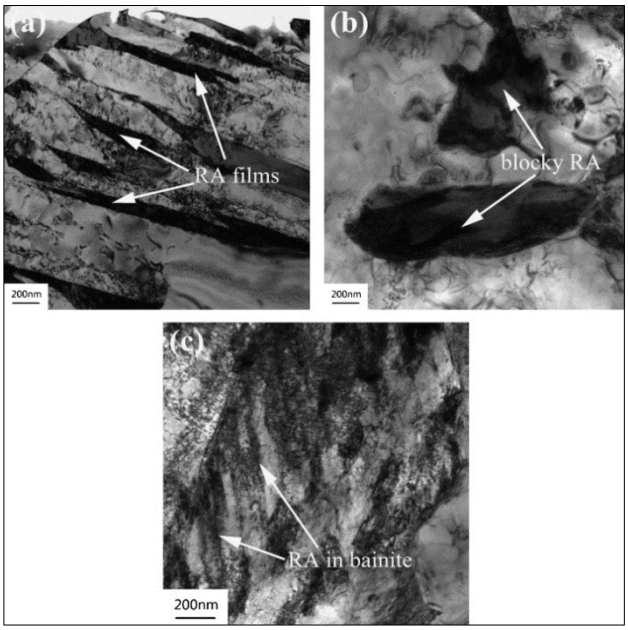

Figure 2-12 TEM micrographs showing different morphology of retained austenite a) film-like retained austenite between martensite laths, b) blocky retained austenite and c) ultrafine retained austenite located in carbide free bainite (7).

Blonde et al. (49) investigated the mechanical stability of retained austenite grains in low-alloyed TRIP steel using synchrotron X-ray diffraction during tensile loading. They concluded that this depends on their carbon content, orientation and volume fraction. They reported that blocky type retained austenite with lower carbon content showed lower mechnical stabilty than film-like retained austenite and austenite grains with the highest Schmid factors showed the least mechanical stability during deformation.

Xiong et al. (50) employed synchrotron x-ray diffraction and TEM to investigate the effect of retained austenite morphology on its mechanical stability in a Q&P steel with chemical composition of Fe–0.22C–1.40Si–1.8Mn. As shown in the plot of normalized intensity vs. x-ray diffraction angle (2θ) for austenite (Figure 2-13), austenite peak (black curve) could be deconvoluted into two different peaks with higher and lower lattice parameter resulting in estimated carbon content of 1.14 and 0.64 wt.% respectively. Although higher carbon content in austenite can increase its thermal stability by lowering the M_s temperature, the synchrotron x-ray diffraction results (Figure 2-13) showed that the higher carbon content retained austenite (red curve) transformed to martensite faster than lower carbon retained austenite (blue curve) during deformation (50).

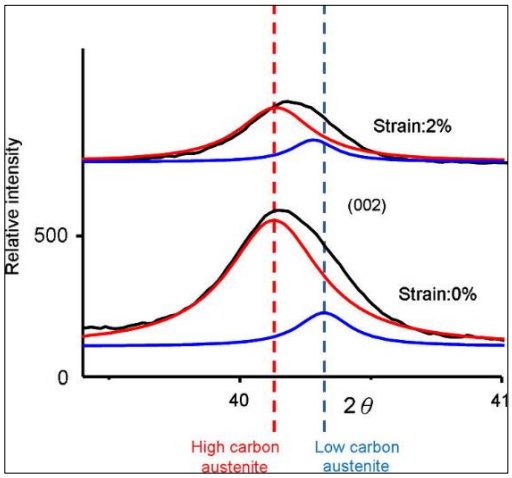

Figure 2-13 Relative intensity versus two theta angle X-ray diffraction of austenite peak for two different strain values (50).

TEM observation of the microstructure of the investigated Q&P steel revealed that retained austenite existed in two morphologies including blocky retained austenite and

film-like retained austenite. They mentioned that film-like retained austenites were found within martensite/retained austenite islands and blocky retained austenites were surrounded by proeutectoid ferrite. Figure 2-14 shows the bright field and dark field images of blocky retained austenite and film-like retained austenite obtained at different strain levels. They reported that all of the blocky retained austenite transformed into twinned martensite in all of the electron transparent zones at 12% strain while many film-like retained austenite regions existed in the sample (50).

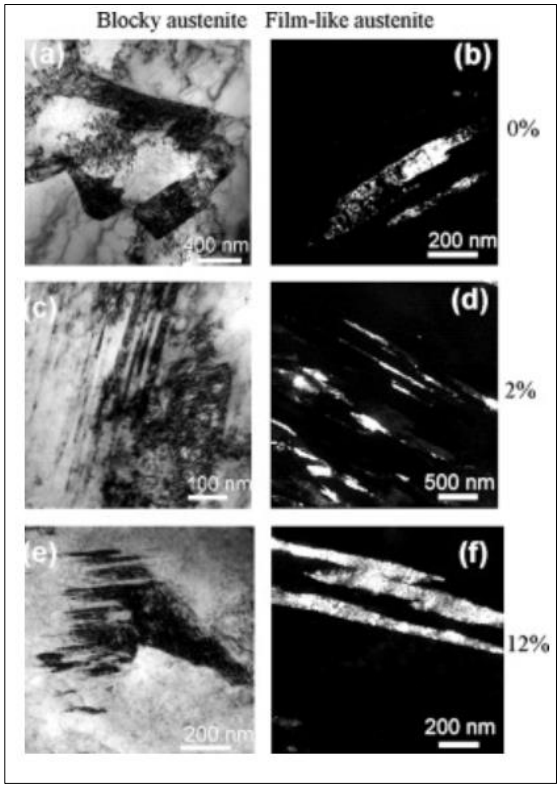

Figure 2-14 Bright field and dark field TEM micrograph of film-like and blocky retained austenite at different strain levels (50).

Jacque et al. (51) investigated the effect of interactions, i.e. stress partitioning, between constituent phases on the mechanical stability of retained austenite in TRIP steels. Two steels with different silicon content were heat treated in such a way that grain size and volume fraction of retained austenite were the same for both steels. However, retained austenite carbon content was lower in the TRIP steel with lower silicon content due to carbide precipitation. The volume fraction of untransformed retained austenite was measured as a function of uniaxial tensile test strain. Results showed that in the samples with lower silicon content transformation occurred faster than in samples with higher silicon content. They concluded that solid solution strengthening of ferrite by silicon in the high silicon steel led to higher stress partitioning toward ferrite rather than martensite, which led to retained austenite stability during deformation. They mentioned that thermal martensite that formed in low silicon TRIP steel as a result of low carbon enrichment of austenite during bainitic holding treatment increases the work hardening of ferrite which results in lower stress partitioning toward retained austenite and can compensate for its low stability (51).

2.2 Damage micromechanisms in advanced high strength steels:

Most studies of damage micromechanisms in advanced high strength steels are based on DP steels and there is little research on damage in other advance high strength steels including TRIP and Q&P steels. Therefore, the studies reviewed in this section are based on the available research on DP steels, except for the following research:

Diego-Calderón et al. (52) studied the effect of Q&P heat treatment parameters on the final microstructure and mechanical properties of steel microconstituents using nano-hardness testing and in-situ SEM tensile tests coupled with DIC method. They subjected a steel with a chemical composition of Fe-0.25C–3Mn–1.5Si–0.023 Al to Q&P heat treatment starting with full austenitization at 850 °C followed by quenching to 244 °C at the cooling rate of 20 °C/s. Samples were reheated to the partitioning temperature of 300 °C or 400 °C with the heating rate of 10 °C/s for the partitioning time of 100 or 500 s and finally quenched to room temperature at 20 °C/s. Three samples were generated with heat treatment parameters given in Table 2-2.

Table 2-2 Q&P heat treatment parameters applied on investigated steel (52).

sample	Partitioning temperature	Partitioning time
QP3-500	300	500
QP4-100	400	100
QP4-500	400	500

They investigated the final microstructure with orientation imaging microscopy (OIM) and reported that it consists of retained austenite (RA), tempered martensite and fresh or untempered martensite (UM). Low indexation and pattern quality areas were assumed to be untempered martensite. They reported that according to the strain maps calculated with DIC, strain localization occurred at bands located at 45-60 degrees with respect to the loading axis. The amount of the strain accommodated in each phase was inversely proportional to Nano-hardness. Figure 2-15 shows an SEM micrograph of QP4-

500 before deformation and after 22% global strain. They reported that higher strength of the harder phase (untempered martensite) led to local deformation and slight rotation of softer tempered martensite phase as depicted with rectangle 1 and 2. Local rupture inside the necking area close to phase boundary was shown with rectangles (52).

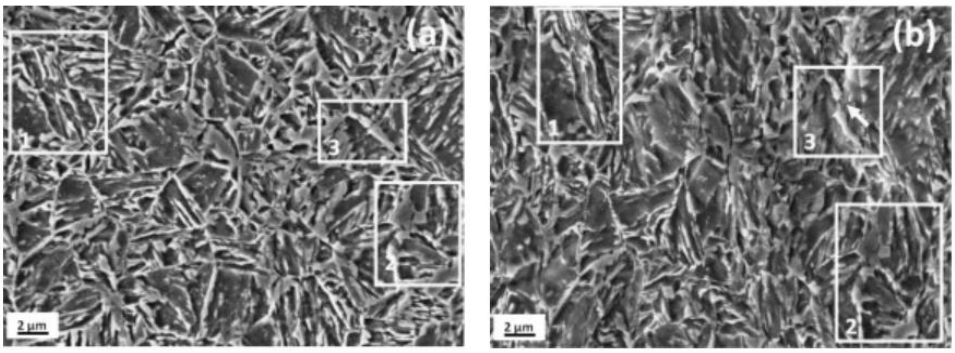

Figure 2-15 SEM micrograph of QP4-500 steel a) before deformation b) at global strain of 22% (52).

Figure 2-16 shows a comparison of strain partitioning between constituent phases in the investigated samples at the global strain of 12.5%. As it can be observed, the strain partitioning was more pronounced in QP4-500 than the other samples. This phenomenon was attributed to the lower mechanical stability of blocky retained austenite and its early transformation to martensite that caused volume expansion in the previously retained austenite blocks and increased the local plastic strain in tempered martensite (52).

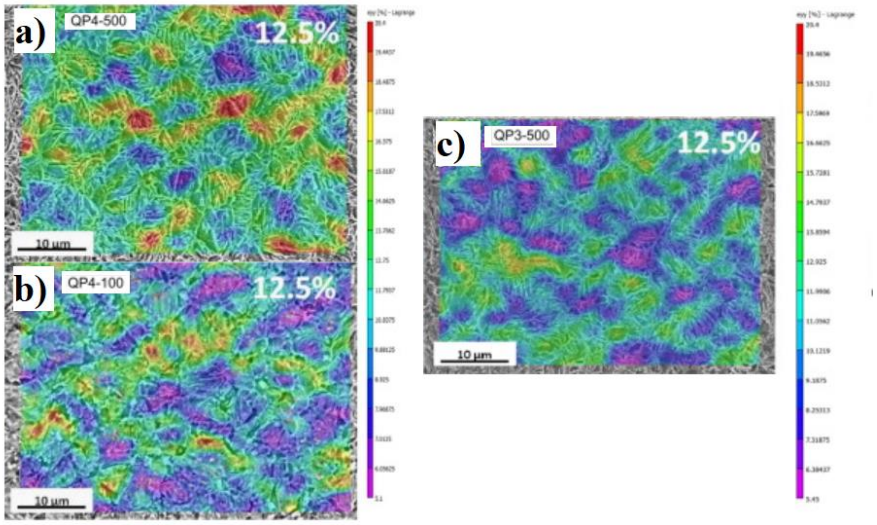

Figure 2-16 Local strain maps of a)QP4-500, b)QP4-100 and c)QP3-500 at global strain of 12.5% (52).

2.2.1 Damage micromechanisms in DP steels:

DP steels have attracted signification attention due their desirable combination of work-hardening, ductility, formability and high strength to weight ratio (53). The above-mentioned characteristics of DP steels result from their unique microstructure consisting of martensite (hard phase) dispersed in ferrite (the soft matrix). Despite their name, DP steels can also contain bainite, retained austenite and pearlite; among them retained austenite and bainite can lead to strengthening of DP steels. Martensite provides DP steels with high tensile strength and ferrite phase enables the low yielding stress and good formability which makes them an ideal choice for automotive sheet-forming operations (20).

Martensite volume fraction and morphology are the main factors that controls the strength and ductility in DP steels. Finely dispersed martensite in the ferrite matrix leads to

improvement in both strength and ductility. Increasing martensite volume fraction decreases the ductility. Besides the difference in final microstructure, heat treatment history and chemical composition may influence the failure mechanisms of DP steels. Lowering the carbon content of martensite as a result of tempering or changing the chemical composition leads to significant deformation of martensite due to its effect on martensite strength (26).

It is reported that for a coarse martensite microstructure, void formation mechanism includes initial cracking at martensite islands at very low strain followed by martensite-ferrite decohesion at higher strain. The size of voids is suggested to be related to the size of the martensite islands. During deformation, ferrite undergoes significantly more deformation than martensite. This strain incompatibility leads to ferrite and martensite separation at the interface (26).

Plastic strain heterogeneity of ferrite is dependent on the morphology, distribution and fraction of martensite. In other words, more ferrite areas can contribute to plastic deformation in a case of fine martensite islands distributed homogeneously throughout ferrite. However, in the case of martensite with a large and blocky morphology even with the lower volume fraction, only a few ferritic grain can participate in plastic deformation and strain accommodation capacity of ferrite phase cannot be fully achieved (54).

Depending on the volume fraction of martensite three types of void nucleation mechanisms including martensite-ferrite interface decohesion, ferrite-ferrite interface decohesion and martensite cracking were observed in DP steels. With low volume fraction

of martensite, deformation occurs in only the ferrite phase with no substantial deformation in martensite. However increasing the martensite volume fraction leads to transformation of deformation mechanisms to martensite-ferrite shearing and martensite island deformation (55).

Three kinds of particles including martensite particles, carbide particles and inclusion particles influence the failure mechanisms of DP steels among them non-metallic inclusions have the lowest interface strength due to the pre-existing cracks and the martensite-ferrite interface has the highest strength due to ferrite matrix reinforcement during tempering process as a result of carbon migration from martensite to ferrite (55).

Kadkhodapur et al. (55) studied the void nucleation, growth and coalescence in a commercial DP800 steel using ex-situ tensile testing coupled with SEM investigation and optical microscopy on three specimens with different strain levels, i.e. after diffuse necking, immediately before failure and after failure. They reported two types of void formation mechanisms in commercial DP800 including void nucleation in ferrite-ferrite long grain boundaries near martensite particles which led to elongated voids and void nucleation due to the separation of martensite-ferrite grain boundaries in the locations where only a few ferrite grains were located between martensite grains that caused spherical voids. Figure 2-17 shows the martensite-ferrite interface separation and void nucleation in ferrite grain boundary in different engineering strain levels (55).

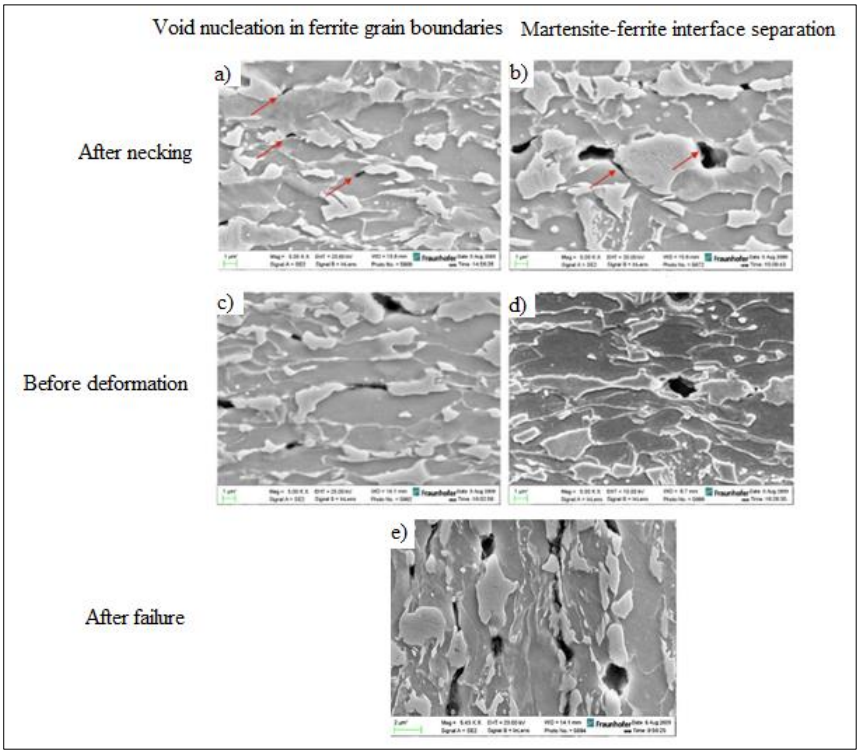

Figure 2-17 Void nucleation mechanisms reported for DP800 in three different deformation stages (55).

They related the first mechanism to strain incompatibilities of martensite and ferrite that caused stress concentration perpendicular to loading direction and second mechanism to high hydrostatic stress existing between the martensite particles from the observation of spherical shape voids (55).

Ghadbeigi et al. (56) investigated the local plastic deformation evolution in DP1000 using in-situ tensile tests under SEM coupled with DIC method. According to local strain maps (Figure 2-18), strain localizations occurred at bands formed at 45 degrees with respect to the loading direction. The bands formed initially inside the ferrite regions but developed

across the martensite islands. The highest local strain value (130%) was recorded inside ferrite but close to ferrite-martensite interface. They observed damage nucleation at ferrite phase, damage initiation at martensite-ferrite interface and crack propagation in martensite phase.

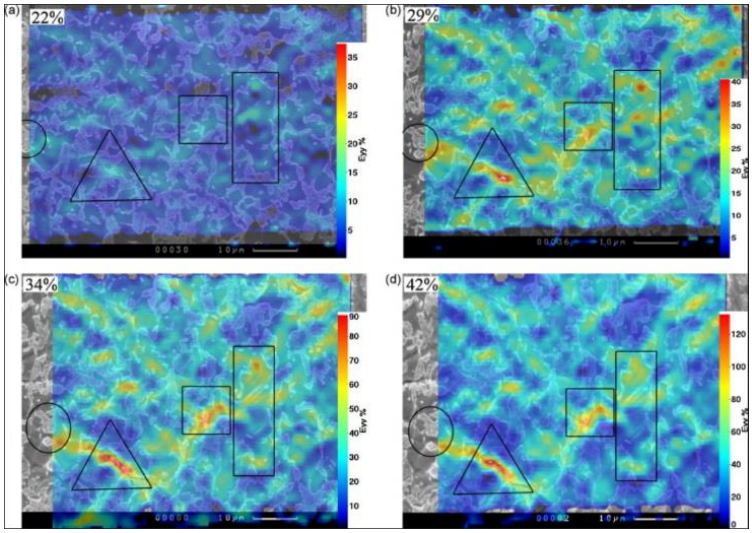

Figure 2-18 Strain partitioning in DP1000 microstructure at different local strain levels (56).

Avramovic et al. (4) studied the effect of martensite morphology and distribution on the damage accumulation in two DP600 steels with different chemical compositions but same volume fraction of martensite using ex-situ tensile test coupled with SEM and optical microscopy investigation. The DP steel with lower C, Si, Mo and Cr and higher Mn content (DP600-A) contained martensite banding parallel to the rolling direction in the mid-thickness of the sheet while the other steel microstructure (DP600-B) contained uniform distribution of the linked martensite phase as shown in Figure 2-19.

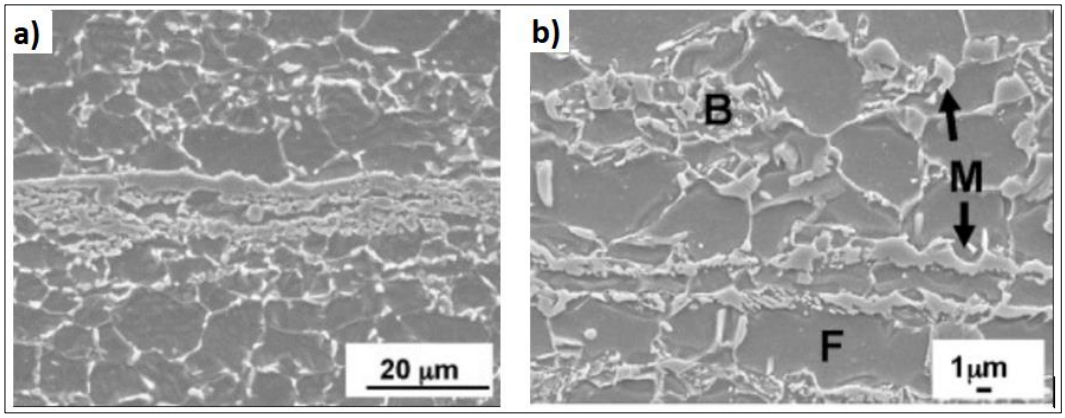

Figure 2-19 a) DP600-A SEM micrograph with martensite banding in the center, b) DP600-B SEM micrograph with uniform distribution of martensite, M:Martensite, B: bainite, F: ferrite (4).

As shown in Figure 2-20 there was a clear difference in void distribution of DP600-A as the voids were located along the center line while the voids were uniformly distributed in DP600-B. It should be noted that there was no significant difference in flow curves of two steels (4).

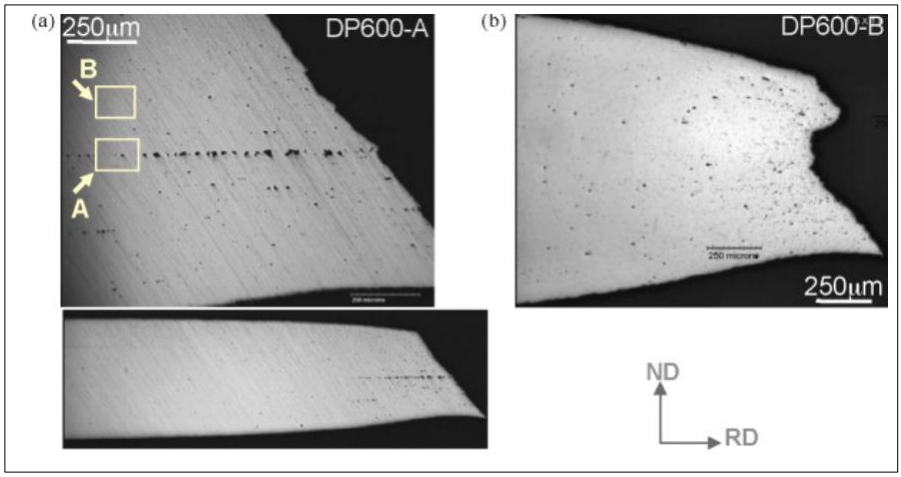

Figure 2-20 Light microscopy images of through thickness cross sections of fractured a) DP600-A and b) DP600-B tensile specimen (4).

They reported four different damage mechanisms in DP600-A including martensite-ferrite interface decohesion, martensite cracking, separation of martensite particles and nucleation of micro-voids on non-metallic inclusions while in DP600-B the majority of voids nucleated at ferrite-martensite interface with constant grow rate at ferrite grain boundaries and fewer voids nucleated at martensite particles (4).

Tasan et al. (57) studied the effect of band phase properties and morphology on the damage mechanisms. They compared the damage behavior of DP600 with distinctive central banding and PF steel with pearlite central banding produced by austenitizing the DP600 and furnace cooling to room temperature. Their methodology involved SEM based in-situ tensile test and DIC method. Figure 2-21 shows the local von Mises strain in each phase versus DIC average strain for the two steels.

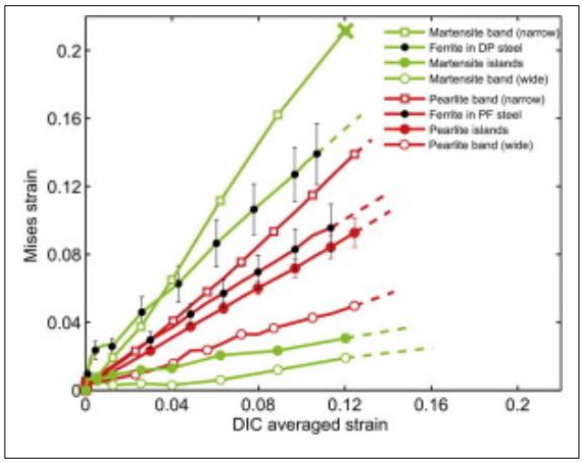

Figure 2-21 Local mises strain versus total average strain for the DP and PF steel showing local strain evolution during deformation (57).

They reported that ferrite and pearlite mixture in PF steel showed lower strain partitioning than ferrite and martensite in DP steel due to their lower strain accommodation incompatibility. In both cases the narrow part of the banding showed higher local strain than wider part of the banding and even ferrite phase. However, in the case of DP steel higher strain localization at narrow region of the bandings, led to cracking of martensite due to higher deformation incompatibility of ferrite and martensite. They concluded that in the case of PF steel shear bands can propagate through the gaps between discontinuous pearlite banding however in the case of DP steel shear band were forced to develop through the martensite banding which led to cracking of banded martensite at its narrowest section (57). Zhou et al.(58) investigated effect of 0.14 w.t. % vanadium addition on deformation and damage behavior in a DP1300 steel using macro-DIC analysis on the SEM micrographs obtained from interrupted tensile tests. Figure 2-22 compares the local strain evolution in ferrite and martensite phase in the V-added and reference DP1300 steel along RD and TD. According to Figure 2-22, addition of Vanadium led to higher deformation in martensite along both TD and RD. Besides, mechanical compatibility of ferrite and martensite improved in RD. Despite this, they reported that similar strain partitioning trend was observed between ferrite and martensite along the TD in both V-added and reference steel. The higher ductility of martensite in V-added steel was attributed to reduction of martensite carbon content and nano-hardness as the results of vanadium carbonitrides formation elsewhere (59).

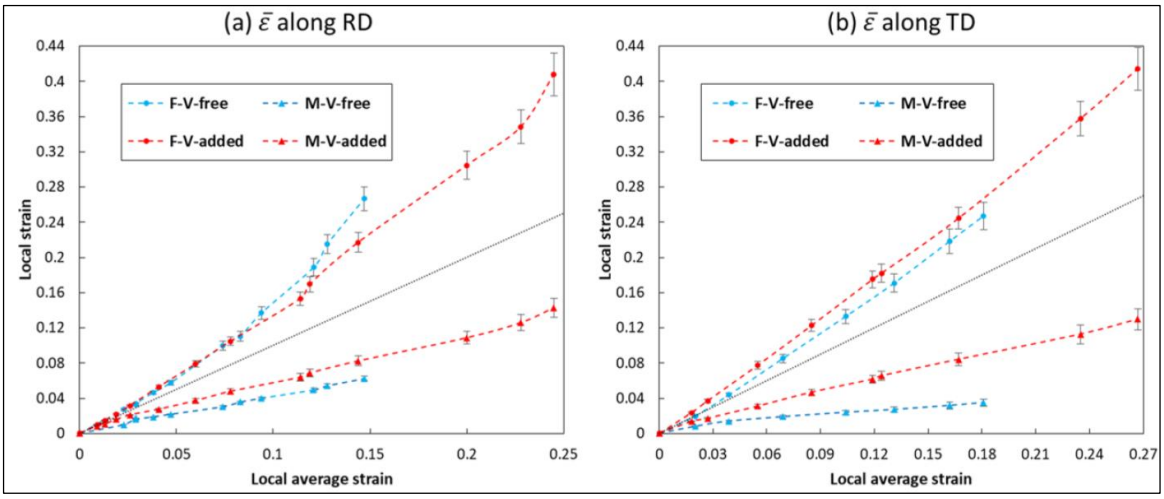

Figure 2-22 local median equivalent strain in martensite and ferrite along a) RD and b) TD as function of overall average strain in a 0.14 w.t% V-added DP1300 steel (58).

2.3 Two dimensional digital image correlation method

Apart from the commonly used strain gauge techniques various non-contact optical methods including interferometric techniques, grid method and DIC have been developed to measure surface deformation (60).

Interferometric techniques measure the deformation based on scattered light wave phase difference recorded before and after deformation and the results are presented in the form of fringe patterns. Interferometric methodology requires a vibration isolated optical platform and coherent light source. Moiré interferometry, holography interferometry and speckle interferometry are considered interferometry variations (60).

Non-interferometric techniques including DIC have less strict experimental condition requirements. DIC was first developed at University of South Carolina in the

1980s. It is an optical method that calculates displacements and strains based on tracking and comparing the surface pattern and features in a series of grey scale deformation images with the aid of numerical computing and correlation algorithm. 2D DIC offers the following advantages over interferometric methods:

(1) 2D DIC only needs one CCD camera to capture the images during deformation and there is no need for sample preparation if the sample has the random pattern on itself; otherwise the surface pattern can be easily made by spraying paints on its surface.

(2) There is no need for laser light source and natural light can be used for illumination.

(3) 2D DIC can be applied to images captured from various devices including laser scanning confocal microscope (LSCM), optical microscope, SEM, scanning tunneling microscope (STM) and atomic force microscope (AFM). Therefore it offers various resolution and measurement sensitivity (60).

It should be mentioned that 2D DIC technique also suffers some disadvantages compared to interferometric techniques including:

(1) strain measurement heavily depends on the quality of image.

(2) There must be a random grey distribution on the measurement surface

(3) 2D DIC strain measurement accuracy is lower than interferometric techniques with the current technology (60).

In general, 2D DIC method implementation can be classified into the following three different steps:

(1) sample and experimental preparation,

(2) surface image acquisition during deformation,

(3) image processing using a DIC computer software to obtain displacement and strain information (60).

The basic experimental setup of 2D DIC is shown in Figure 2-23. The specimen surface and CCD camera must be parallel to each other in order to prevent out of plane motion. Otherwise this will cause additional in-plane displacement that leads to error in calculation of actual physical point motion. Out of plane motion can be eliminated by the use of a telecentric imaging system (60).

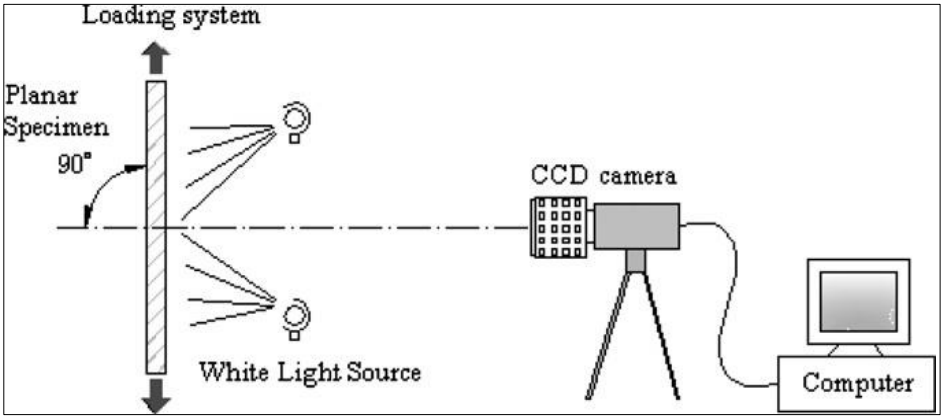

Figure 2-23 Schematic illustration of typical experimental setup for 2D DIC (60).

After image acquisition, the deformation images are fed into DIC software to calculate the strain map. The calculation area in the reference image also known as region of interest (ROI) is defined in the beginning and divided into virtual grids to calculate the displacements. Figure 2-24 shows the virtual grid superimposed on the reference image. The motion of each grid point is tracked using the red square known as subset or facet with the grid point in its center. The reason for using the square facet with multiple pixel instead of individual pixel is that a facet with wider variation of gray level can be distinguished easily from other facets in a deformed image (60).

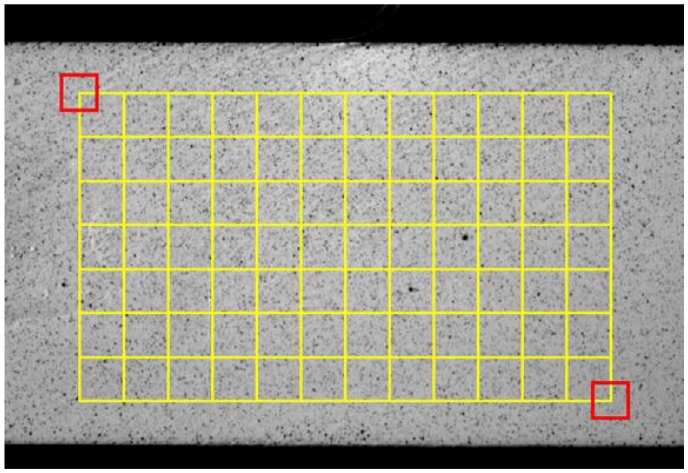

Figure 2-24 Virtual grid superimposed on a reference image (60).

Figure 2-25 shows two 15x15 pixel facets with a 2 pixel overlapping area or with a 13 pixel facet step defined as a default facet in ARAMIS software (61).

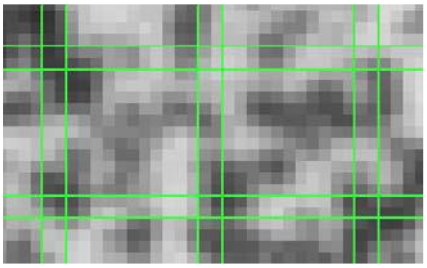

Figure 2-25 Two 15x15 pixel facets with 13 pixel facet step (61).

The similarity degree between deformed subset and reference subset is evaluated using predefined sum-squared difference (SSD) correlation criterion or cross-correlation (CC) criterion. Correlation is achieved by searching the extremum position of correlation coefficient distribution. Finding the correlation coefficient extremum determines the deformed subset position that produced the displacement vector (60).

The points around the subset center can be correlated using displacement mapping function or shape function.

Figure 2-26 shows (2M + 1) × (2M + 1) facet before and after deformation in which M= | i | and $\mathrm{p}(x_0, y_0)$ is the facet center and $\mathrm{Q}(x_i, y_j)$ is a neighboring point to the facet center (60).

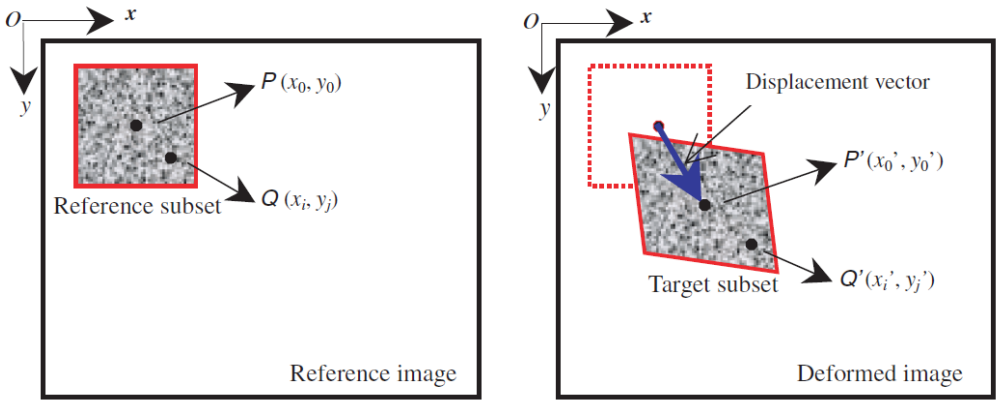

Figure 2-26 Schematic illustration of reference facet before and after deformation (60).

$Q(x_i, y_j)$ can be mapped into $Q'(x'_i, y'_j)$ using shape function as follows:

$$x'_i = x_i + \xi(x_i, y_i),\ y'_i = y_j + \eta(x_i, y_i) \quad (i, j = -M : M). \quad (2\text{-}3)$$

In the case of rigid body translation or same displacement for each point in the facet during deformation, zero-order shape function can be used:

$$\xi_0(x_i, y_j) = u\ ,\eta_0(x_i, y_j) = v \quad (2\text{-}4)$$

Obviously rigid body translation or zero-order shape function is not sufficient for showing the deformation in a facet. Therefore, first-order shape function that allows shear, rotation, normal strains, translation and their combination of the facet can be used:

$$\xi_1(x_i, y_j) = u + u_x\Delta x + u_y\Delta y,\ \eta_1(x_i, y_j) = v + v_x\Delta x + v_y\Delta y \quad (2\text{-}5)$$

More complicated deformation of a facet can be depicted by the second-order shaped function proposed by Lu et al. (62) as follows:

$$\xi_2(x_i, y_j) = u + u_x\Delta x + u_y\Delta y + \tfrac{1}{2}u_{xx}\Delta x^2 + \tfrac{1}{2}u_{yy}\Delta y^2 + u_{xy}\Delta x\Delta y$$

$$\eta_2(x_i, y_j) = v + v_x\Delta x + v_y\Delta y + \tfrac{1}{2}v_{xx}\Delta x^2 + \tfrac{1}{2}v_{yy}\Delta y^2 + v_{xy}\Delta x\Delta y. \quad (2\text{-}6)$$

In the equation (2-3), (2-4) and (2-6), $\Delta x = x_i - x_0$, $\Delta y = y_i - y_0$,u, v are the x- and y- displacement components of reference facet center, $p(x_0, y_0)$, v_x, v_y, u_x, u_y are reference facet first order displacement gradients and v_{xx}, v_{xy}, v_{yy} u_{xx}, u_{xy}, u_{yy} are the reference facet second order displacements gradients (60).

2.3.1 Microscopic DIC

As mentioned in the previous section 2D DIC technique offers various resolution and strain measurement sensitivity since it can be applied to the images that captured from various devices with different magnification and resolutions. In this section some of macroscopic DIC applications in different research fields is briefly reviewed and then the most important micro-scale patterning method that can be applied to in-situ tensile test under SEM are discussed.

Kang et al. (22) showed the effect of tempering heat treatment on the strain distribution between martensite and ferrite region in DP600 steel using micro-DIC analysis on deformation image series obtained from in-situ tensile tests under SEM. They first developed a micro-DIC analysis methodology based on using the native microstructure revealed after metallographic etching as the speckle pattern used for DIC calculation at

McMaster University in 2005 (22). Carroll et al. (63) applied macro-DIC technique to optical microscope images obtained from a growing fatigue crack at different crack tip locations in a Hastelloy X specimen so as to find the plastic strain near the growing crack which was further linked to grain orientation obtained from electron back scattered diffraction (EBSD) results to improve their understating of fatigue crack growth behavior. Sabaté et al. (64) measured residual stress on a Microelectromechanical systems (MEMS) structure with the aid of micro-DIC analysis on the SEM micrographs. The methodology involved measuring the displacement generated from the local stress release around a hole drilled with focused ion beam (FIB) in the microstructure with inherent residual stresses and fitting the displacements obtained from micro-DIC to analytical solution for finding the residual stress.

Micro-DIC technique with the aid of AFM can be used to analyze the structure reliability or mechanical performance of microelectronic devices and interconnections under actuations such as thermal loading or electrostatic force which is very important for functional control and design of the microsystems (65, 66). For example Sun et al. (65) applied micro-DIC analysis on AFM images captured from a microelectronic device to achieve in-plane deformation field in a micro-thermoelectric cooler between its heating and cooling stages.

Distortion of AFM images due to the nonlinear motions or drift of AFM piezoelectric scanner, creep effects or scanner hysteresis is considered the great

disadvantage of micro-DIC analysis with AFM and its correction has been investigated in many researches (67-69).

It should be noted that the later technique requires bringing a probe or tip very close or on the surface of the sample which is not suitable for biological materials (70). Deformation at sub-cellular or cellular level can be measured using digital volume correlation with the aid of fluorescence confocal microscopy which can show the three dimensional morphologies and interaction of cells as expected in vivo rather than two dimensional environment so as to study the biochemical and mechanical signaling in directing cellular behaviors (71).

2.3.2 Micro-scale patterning methods used for in-situ tensile testing under SEM

DIC sample requires high contrast, isotropic and random patterns to track them and to compare them in a series of gray scale deformation images to calculate displacement and strain using the correlation algorithms. Macro-scale patterning such as using toner powder, paint spraying and airbrushing are not applicable to micro-scale 2D DIC method due to the fact that they cannot produce the required small ROI size (72). The pattern produced with metallographic etching have been used as a speckle pattern in several studies for local strain measurement using macro-DIC analysis method on the deformation micrographs obtained from SEM based in-situ tensile testing on metallic samples (22, 52, 56, 57, 73). However, there is a need for applying patterns in cases when an EBSD map must be superimposed on

the deformation surface (74, 75) or the produced microstructure as the results of etching does not have the enough features with the required size that can be tracked by DIC software. In this section two important general patterning methods which can be applied on the in-situ tensile testing specimens including nano particle patterning and FIB patterning are discussed. Further information regarding micro-scale patterning can be found elsewhere (72).

2.3.2.1 Nanoparticle patterning:

Nanoparticle patterning is a cost effective and fast patterning process that produces the speckle patterns in minutes. As shown in Figure 2-27, the produced pattern yields high contrast and wide speckle pattern distribution in backscatter and secondary electron images. Nano particle agglomeration and controlling pattern location are the main challenges of this method application. It should be noted that although large agglomerates are needed to break up with ultrasonic cleaner, some clumping is preferred to create a random pattern (72).

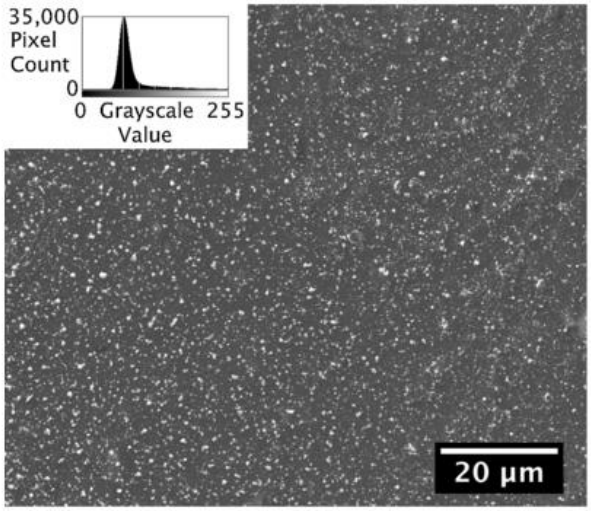

Figure 2-27 SEM micrograph showing 100 nm Au nanoparticle deposited on a 6061-T6 polished surface (72).

Decreasing drying time leads to better quality of nanoparticle speckle pattern. Longer drying times cause re-agglomeration and non-homogeneous dispersion of nanoparticles as most of the nanoparticles settle at the evaporating droplet contact line and cause phenomena known as ‘coffee ring’ effect. Various techniques including spin coating, heating, angling and heating were studied to decrease the drying time. Substrates with high surface energy produce better pattern quality than substructures with low surface energy since nanoparticle droplets have lower contact angle on them which causes faster drying process of nanoparticles. Aluminum and its alloys form an oxide layer immediately after exposure. The surface energy of the initially formed oxide layer is high and nanoparticles dry quickly on them. However, the surface energy of the oxide film degrades as it absorbs water molecules from atmosphere which results in higher contact angle of nanoparticles and their lower drying process. Using small nanoparticle droplet and freshly polished substrate in the case of using aluminum substrate can increase the drying rate (72).

2.3.2.2 FIB patterning:

FIB can be used to produce speckle patterns suitable for micro-scale 2D DIC. The advantage of using FIB as a patterning method is its ability to produce exact desired pattern with high repeatability. However, the produced patterns or holes can act as stress riser which makes them an inappropriate choice for the SEM based in-situ testing coupled with

EBSD analysis since they degrade the crystallographic measurements. The surface damage can be avoided by using the electron beam instead of gallium ions in the expense of increasing the processing time by the factor of 5 in the case of using SEM with tungsten filament. In general FIB patterning is considered to be an expensive and time-consuming method as generating 35 × 35 μm area takes 4 hours (72).

3 Experimental procedure

3.1 Material

The QP980 cold rolled steel sheet has a thickness of 1 mm. Chemical composition of the QP980 steel used in this research is shown in Table 3-1. This steel contains close to 1.5% manganese to suppress the carbide precipitation during the partitioning process and approximately 2% manganese to improve the austenite stability.

Table 3-1 Chemical composition of QP980 steel.

Fe	C	Mn	Si	Al	P	S
Balance	0.206	1.962	1.474	0.037	0.008	0.002

3.2 Metallography

Metallography samples were cut using Fadal VMC 4020 CNC vertical machining center and cold mounted in epoxy. They were ground and polished to a 0.04 μm finish. Grinding and polishing procedure was summarized in Table 3-2.

Table 3-2 Grinding and polishing procedure used for preparation of metallography samples.

	step	Surface	lubricant	Force (N)	Time (min)
Grinding	1	SiC paper #400	Water	25	2:20
	2	SiC paper #600	Water	25	2:20
	3	SiC paper #800	Water	25	2:20

	5	SiC paper #1000	Water	25	2:20
	6	SiC paper #1200	Water	15	3:00
Polishing	7	MD-Dac, 9 µm diamond suspension	Green	20	6:00
	8	MD-Dur, 6 µm diamond suspension	Green	20	6:00
	9	MD-Nap, 1 µm diamond suspension	Green	20	15:00
	10	MD-chem, 0.04 µm colloidal silica suspension (OPS)	-	15	1:10

Green lubricant mentioned in Table 3-2 is the water-based lubricant containing 70% ethylene glycol, 20% glycerol and 10% ethanol, which provides best combination of materials removal and surface finish.

After each step, samples were first cleaned with deionized water and then cleaned immediately with ethanol followed by drying with hot air stream. Samples were then etched for 10 s in 2% nital to reveal the microstructure.

3.3 Tensile tests:

Tensile tests were performed according to ASTM E8/E8M − 16a on subsize tensile specimens machined in rolling direction (RD) and transverse direction (TD) with the geometry shown in Figure 3-1 using MTS 810 Material Testing System operated with 8800 series systems from Instron with 100kN load cell. Tensile tests were conducted 3 times each in TD and RD at room temperature with constant speed of 1 mm/min or nominal strain rate of 6.5×10^{-4} s^{-1}.

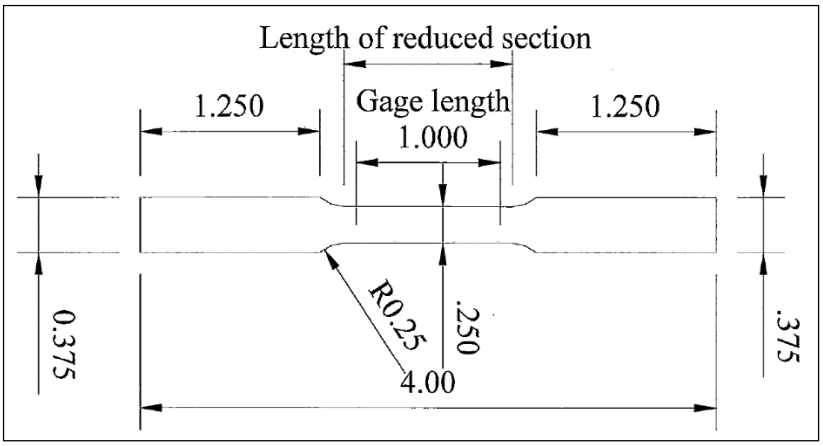

Figure 3-1 Subsize tensile specimen geometry used for tensile tests.

3.4 Fractography:

Fractography was performed on the fractured subsize and hourglass shape tensile specimens using JEOL 6610 LV SEM.

3.5 Microscopic digital image correlation

The hourglass shape sample geometry used for in-situ tensile testing under SEM is shown in Figure 3-2.

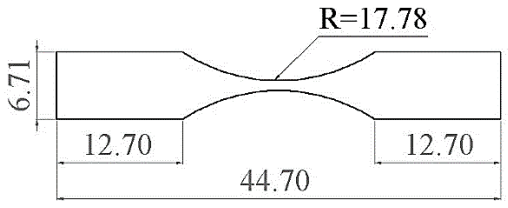

Figure 3-2 Geometry of hourglass shaped specimen used for in-situ tensile testing under SEM (mm).

The procedure of SEM in-situ tensile testing used for obtaining microscopic local strain map is summarized in Figure 3-3.

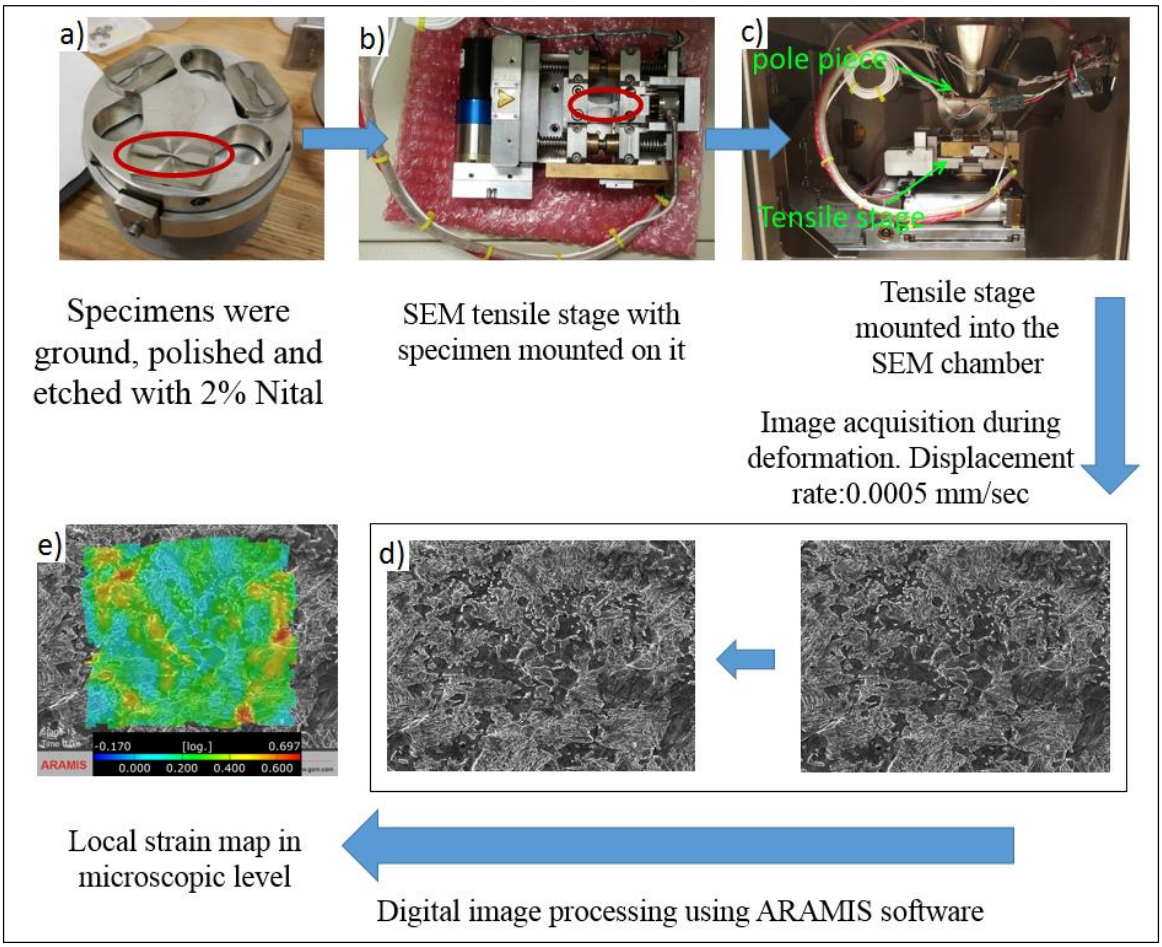

Figure 3-3 Experimental procedure performed on QP980 hourglass specimen for obtaining DIC microscopic strain map.

Hourglass shape specimens were sectioned using Fadal VMC 4020 CNC vertical machining center. As shown in Figure 3-3 hourglass shaped specimens were glued on the jigs (depicted with red oval) and then mounted on the automatic Struers polishing machine to be ground and polished. The polishing and grinding procedure used in preparing of in-situ SEM tensile testing samples is summarized in Table 3-2. Samples were then detached

from the jigs and cleaned with Acetone. Finally, they were etched with 2% nital solution. No speckle pattern was applied on the samples surface and the microstructure revealed through the etching step was used as the speckle pattern needed for DIC calculations. Specimens were then subjected to uniaxial tensile test at room temperature using MTII/Fullam SEM Tensile Tester under SEM JEOL 6610 LV with the constant speed of 0.0005mm/sec. Figure 3-3 b shows the SEM tensile stage outside the SEM chamber with hourglass shape tensile specimen mounted on it (shown with red oval). One disadvantage of working with MTII/Fullam SEM tensile tester is the required high working distance of SEM during image acquisition step. As seen from Figure 3-3 c, there is a possibility of SEM pole piece collision with the tensile stage if the distance between them decreases more than a specific amount. The lowest possible working distance while the tensile tester is mounted on SEM is 21 mm which is more than twice the general working distance of SEM JEOL 6610. This leads to lower resolution and quality of image compared to the condition which the image is captured at working distance within the range from 10 to 12 mm. The in-situ tensile testing SEM micrograph were taken at 1500x-3000x magnification with 12-15 accelerating voltage, 21-22 mm working distance and the 37-40 μm spot size. Higher number of images were captured in the post uniform elongation region compared to uniform elongation since most of the damage and high level of deformation and strain localization occurs after uniform elongation ends. Figure 3-4 shows displacement vs. stage number curve for a typical deformation image series. Note that necking usually occurs after 0.45mm displacement and fracture occurs after 0.7mm displacement.

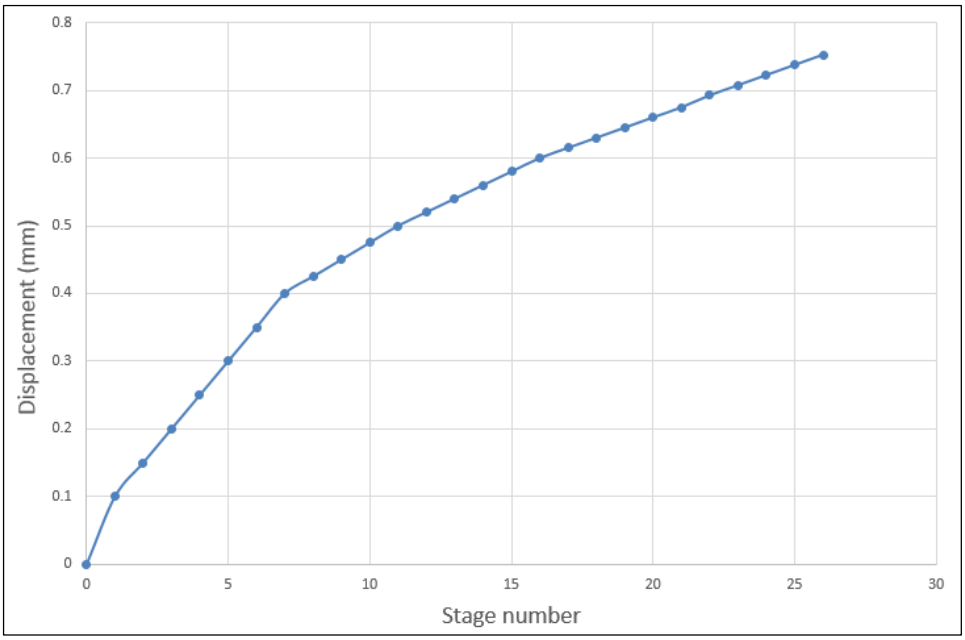

Figure 3-4 Typical displacement-stage number curve for a deformation image acquisition process on an hourglass shape QP980 steel specimen.

Finally, the obtained deformation images were converted into grey scale and fed into the ARAMIS software to calculate local strains in the constituent phases of the QP980 steel microstructure (Figure 3-3 d).

3.6 XRD analysis:

The retained austenite volume fraction was determined using Bruker D8 DISCOVER with DAVINCI design diffractometer equipped with Vantec 500 (MiKroGap TM technology) area detector and Cobalt Sealed Tube Source (λ_{avg}= 1.79026 Å) operated at 35 kV and 45 mA. Samples were scanned over the 2-theta range from 45 to 127 degrees. Measurement Centre Version 4.2 software was used to collect the 2D frames which were

integrated to 1D data with the aid of DIFFRAC.EVA Version 4.0 software. The data were then displayed and analyzed in Topas Version 4.2 to calculate the retained austenite volume fraction. The X-ray beam size and exposure time used to measure the retained austenite volume fraction were 0.5 mm and 40 min/measurement respectively. In order to measure the retained austenite volume fraction 3 samples were cut with the dimension of 2×2 cm using Fadal VMC 4020 CNC vertical machining center and mounted in epoxy through the thickness. Table 3-3 shows the final surface conditions of the samples used for determination of retained austenite volume fraction in QP980 steel. Each measurement was conducted two times.

Table 3-3 Final surface condition of the specimen used for retained austenite volume fraction measurement.

# sample	Final surface condition
1	polished to a 1µm finish
2	polished to a 0.04 µm finish
3	Etched with 2% nital for 10 s after polishing to 0.04 µm finish

In order to investigate TRIP phenomena in QP980 steel, ex-situ tensile test coupled with XRD was conducted on the surface of hourglass shape tensile specimen (Figure 3-2) after manually polishing with 400 and 600 grit silicon carbide abrasive paper the both sides. Specimen was pulled in a uniaxial tension using MTII/Fullam SEM tensile tester at room temperature and with constant speed rate of 0.0005mm/sec. Each retained austenite measurement was conducted three times. The X-ray beam size was decreased from 0.5mm to 0.3mm at local true strains higher 0.7 in order to improve the accuracy of the

measurements with decreasing the width and thickness of the deformation region in hourglass shape specimen during tensile tests. X-ray exposure time was increased from 40min/measurement to 80min/measurement at local true strains higher than 0.53 by which point the retained austenite volume fraction decreased to less than 2%. Local true strains in hourglass shape specimen for ex-situ tensile test coupled with XRD were calculated using the thickness and width of the specimen measured with AZ 100M Nikon Stereoscope after each interrupted tensile test. Locations of the retained austenite measurements were shown with the cross sign on the load-displacement curve obtained from the SEM tensile tester (Figure 3-5). As can be seen from the Figure 3-5 four measurements were conducted in the uniform elongation region and three measurements were conducted in the post uniform elongation region.

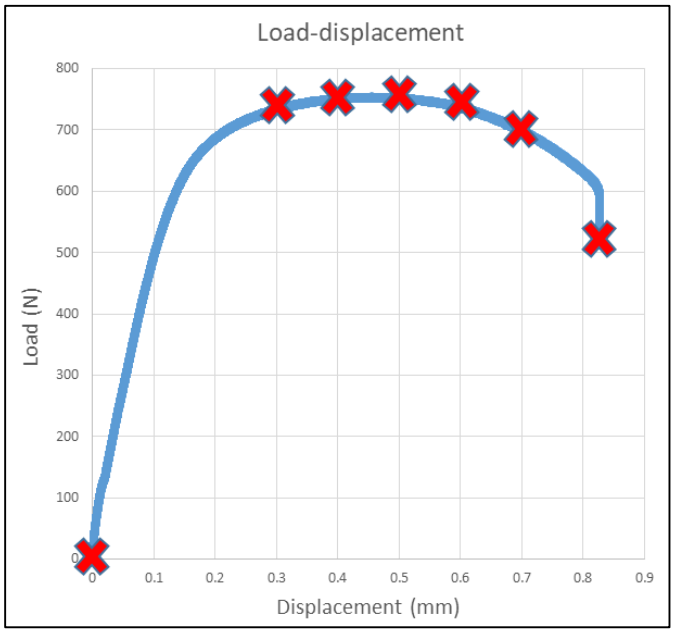

Figure 3-5 Load-displacement curve of QP980 hour-glass shaped specimen. Locations of tensile test interruptions were shown with the cross sign on the curve.

3.7 Ex-situ tensile test coupled with EBSD

The hourglass sample shown in Figure 3-2 was used to investigate TRIP phenomena in QP980 steel during deformation. The specimens were ground and polished according to procedure described in Table 3-2. The interrupted tensile tests were conducted using the MTII/Fullam SEM tensile tester outside the SEM with the constant speed of 0.0005 mm/sec at room temperature. All the measurements were performed in the uniform deformation region. Total true strain of each EBSD map in tension direction was obtained using the ImageJ software. EBSD maps were collected using the JEOL 7000 FESEM microscope equipped with Aztec software. The operating parameters were 70° tilt, 50 nm step size, 20 kV accelerating voltage, 15 mm working distance and 45.5×34.1 µm and 90.9×68.2 µm scan areas. At true strain levels lower than 7%, 4×4 EBSD camera binning mode, 70-80 Hough resolution, 5.5-8 ms exposure time and gain number of 4-11 were used to perform the EBSD analysis. However, at true strains higher than 7%, 2×2 EBSD camera binning mode, 50-60 Hough resolution, 20-21 ms exposure time and grain number of 7-8 were used to order to increase pattern quality to compensate for pattern degradation associated with lattice distortion and deformation. Obtained EBSD patterns were analyzed using the Tango EBSD post processing software embedded in HKL CHANNEL 5 system.

3.8 Nano-hardness

Nano-hardness measurements were carried out using Anton Paar nanoindentation tester (UNHT) at 2500 μN. The nano indents were applied with diamond Berkovich indenter at room temperature. The applying force was increased with constant rate of 15000 μN/min and the indentation depth was recorded simultaneously. 1×1 cm sample was cut using Fadal VMC 4020 CNC vertical machining center from QP980 steel sheet, cold mounted in epoxy and was ground and polished with the procedure described in Table 3-2. The sample was then lightly etched with 2% nital solution. Nano indentations were performed in the form of both grid indentation as a statistical method and single point indention which targeted the retained austenite blocks. The indent grid consisted of an array of 6×6 indents with horizontal and vertical spacing of 4 μm between them. 17 single indents were applied on the nano-hardeness sample to measure the retained austenite blocks.

4 Results and discussions:

4.1 Microstructure:

Figure 4-1 shows an SEM micrograph of QP980 steel. The microstructure consists of ferrite, martensite islands and blocks which are confirmed to be retained austenite by EBSD analysis. Figure 4-2 shows an EBSD Quality Map collected from a QP980 sample. Martensite and ferrite are shown in the form of band contrast and retained austenite is shown with the red color. Zero solution areas that did not produce any EBSD pattern are shown with black color. Martensite appears with lower band contrast compared to ferrite due to the lattice distortion and lower pattern quality. Retained austenite blocks are distributed inside ferrite, within martensite regions and at their interfaces. Retained austenite in QP980 steel also exists in the form of films located between martensite laths which cannot be detected with EBSD analysis due to their submicron size. It has however been detected by TEM analysis elsewhere (76). Existence of ferrite in the microstructure indicates the intercritical annealing step in the heat treatment process. Carbide precipitation should not ideally happen during the partitioning process; however, according to Figure 4-1, there are some regions inside martensite that show evidence of carbide precipitation, which indicates tempering of martensite. Existence of carbide precipitates can be attributed to exposure of QP980 to partitioning times higher than the range in which carbon partitioning happens between martensite and austenite during industrial quench and partitioning process.

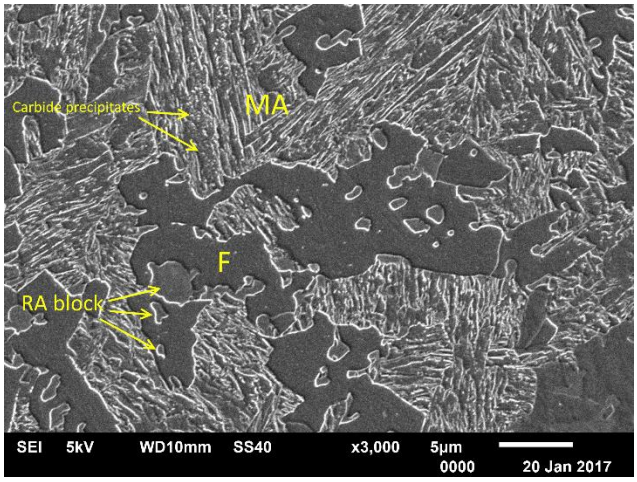

Figure 4-1 SEM image of QP980 steel microstructure consists of Martensite regions containing film-shape retained austenite (MA), Ferrite (F), retained austenite blocks (RA) and carbide precipitates.

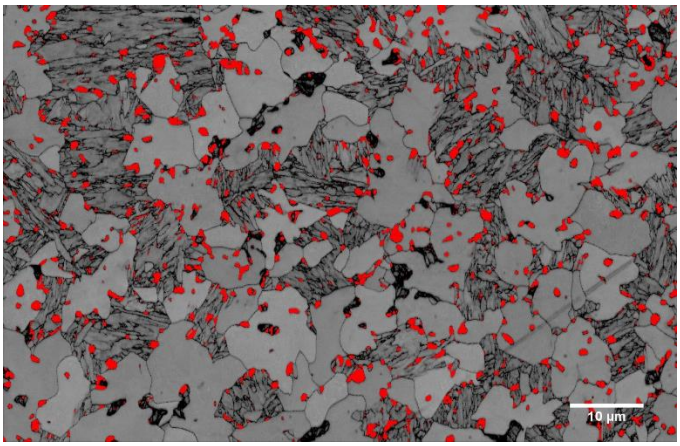

Figure 4-2 QP980 EBSD map, Ferrite and martensite are shown with the band contrast and Red color corresponds to retained austenite phase.

QP980 steel suggested heat treatment cycle and phase diagram are shown in Figure 4-3 and Figure 4-4 respectively. Heat treatment cycle was received from General Motors R&D Center while the phase diagram was calculated by Thermo-Calc using the chemical composition of the steel.

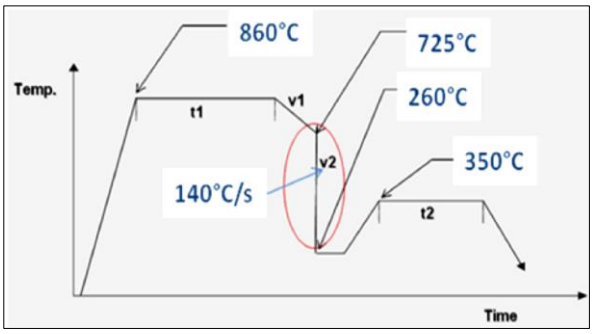

Figure 4-3 QP980 steel predicted heat treatment cycle.

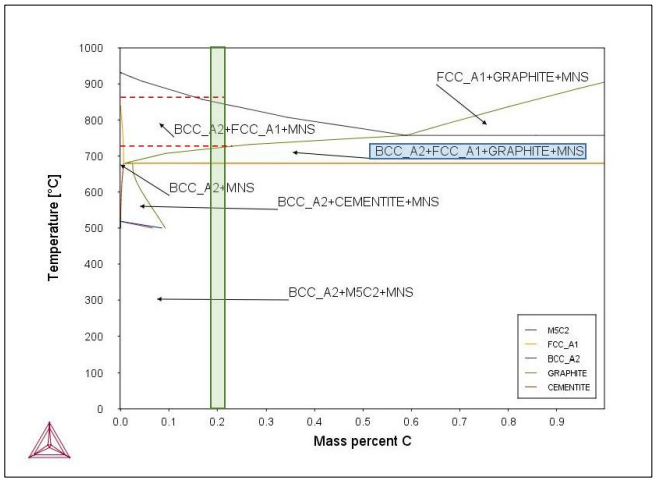

Figure 4-4 QP980 steel phase diagram calculated with Thermo-Calc.

Using the equation 2-2 and chemical composition of QP980 steel, M_S temperature was calculated to be 387 °C. By comparing heat treatment cycle and phase diagram and considering carbon concentration of QP980 to be 0.2wt%, it can be concluded that the heat treatment starts at a temperature in the austenite region very close to intercritical annealing region in order to produce fine austenite grains followed by cooling slowly into the intercritical region in which ferrite grains grow on austenite grain boundaries. Material is then quenched to 260°C which is below the martensite start (387 °C) in order to produce a

certain amount of martensite. This is followed by the partitioning step at 350°C during which carbon enrichment of austenite occurs and in some regions carbide precipitates form instead of partitioning as mentioned earlier. Finally, material is cooled to room temperature.

The result of retained austenite volume fraction measurements on the QP980 samples is shown in Table 4-1.

Table 4-1 Retained austenite volume fraction measured on the QP980 samples.

Sample	Retained austenite volume fraction %
polished to a 1μm finish	8.7
polished to 0.04 μm finish	8.1
Etched with 2% nital after polishing to 0.04 μm finish	8.7

It is found that the effect of surface condition investigated within the range mentioned in Table 4-1 on the retained austenite volume fraction measurement is small and the average retained austenite volume fraction of QP980 was calculated to be 8.5% which is in a good agreement with the values reported in the literature (77, 78).

Table 4-22 shows the volume fraction of all constituent phases in QP980. Figure 4-5 shows an optical microscope image captured through the thickness of the QP980 steel. Volume fraction of ferrite is considerably higher at the regions close to edges of the sample or surfaces of the QP980 steel sheet as shown with blue arrows. The thickness of this region or layer is estimated to be between 40 and 80 μm. There are also regions in the mid-thickness that contain higher volume fraction of Martensite as depicted with red arrows. Volume fraction of ferrite was measured to be 33% using ImageJ and SEM

micrographs taken from the thickness. Six images were taken from the edge to the center of the sample which each of them covering 128×96 μm of the thickness surface. The ferrite areas were colored and measured with ImageJ. The highest volume fraction of ferrite was recorded at the closest image to the edge with a volume fraction of 39.7% and the lowest volume fraction of ferrite was recorded at the image taken from the mid-thickness of the sample with a volume fraction of 28.6%. Finally, volume fraction of martensite was calculated by subtracting the sum of the ferrite and retained austenite volume fraction from the whole.

Table 4-2 Volume fraction of different phases in QP980 steel.

Phase	Volume fraction wt. %
Retained austenite	8.5
Ferrite	33
Martensite	58.5

Figure 4-5 Optical microscope image captured from the thickness of the QP980 steel. Blue and red arrows show regions with higher volume fraction of ferrite and martensite respectively.

The average initial retained austenite volume fraction measured on the EBSD ex-situ tensile test samples was 6% which is in the good agreement with the work of other researchers who measured QP980 retained austenite volume fraction using EBSD (77, 79, 80). It should be noted that EBSD measured retained austenite is 2.5 wt.% lower than the XRD measured value which can be since film-like retained austenite cannot be detected by ESBD analysis due to their submicron size and capability limitation of EBSD analysis instrument itself.

4.2 Tensile properties of QP980 steel:

Engineering and true stress-strain curves for QP980 steel in rolling direction (RD) and transverse direction (TD) are shown in the Figure 4-6 and Figure 4-7 respectively.

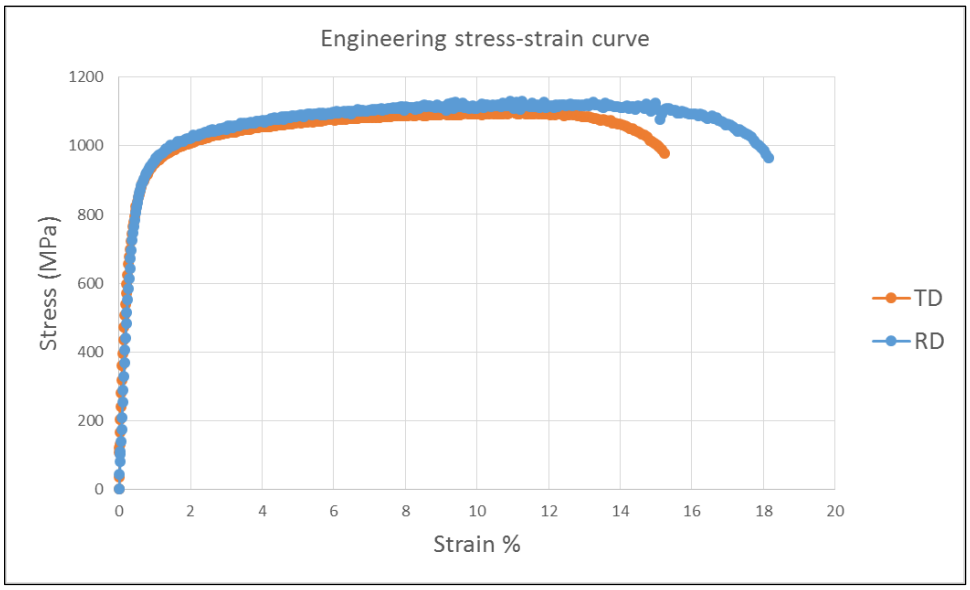

Figure 4-6 Engineering stress-strain curve of QP980 steel.

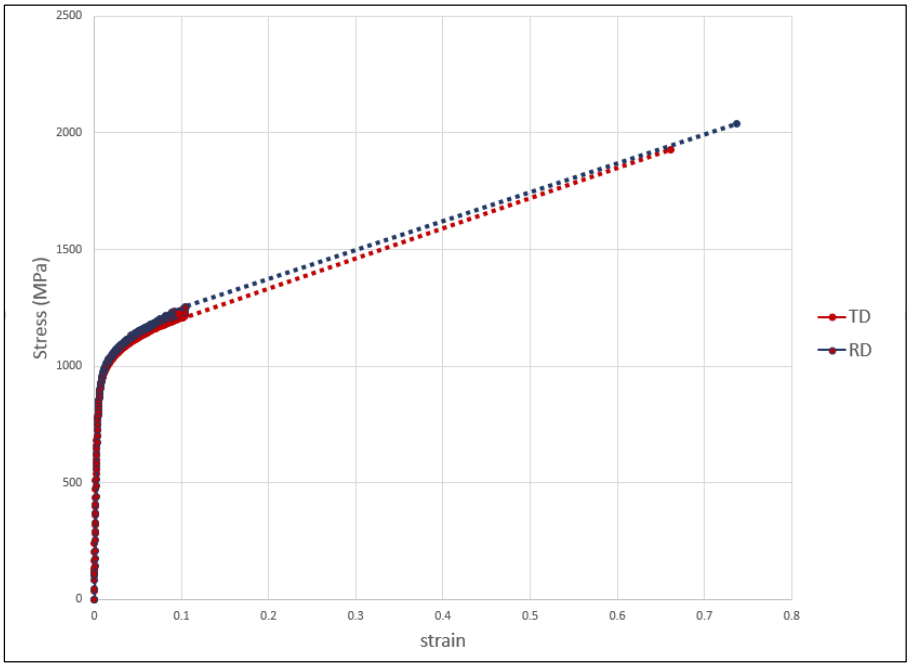

Figure 4-7 True stress-strain curve of QP980 steel in RD and TD.

QP980 steel shows higher uniform and post uniform elongation in RD compared to TD. The average tensile properties of QP980 steel calculated from three samples are summarized in Table 4-3. The high true strain value at the point of failure indicates that QP980 steel undergoes substantial necking and post uniform deformation which will be discussed in more detail in section 4.6 and 4.7.

Table 4-3 Tensile properties of QP980 steel measured in TD and RD.

	Tensile strength (MPa)	Uniform elongation %	Post uniform elongation%	Total elongation %
RD	1128	11.5	7.0	18.5
TD	1094	10.4	5.0	15.4

4.3 Fracture surface:

Ductile fracture and shear fracture are the two dominant fracture types and there is no evidence of quasi cleavage or cleavage fracture in the QP980 steel studied here. Figure 4-8 shows the fracture surface of subsize tensile sample in TD.

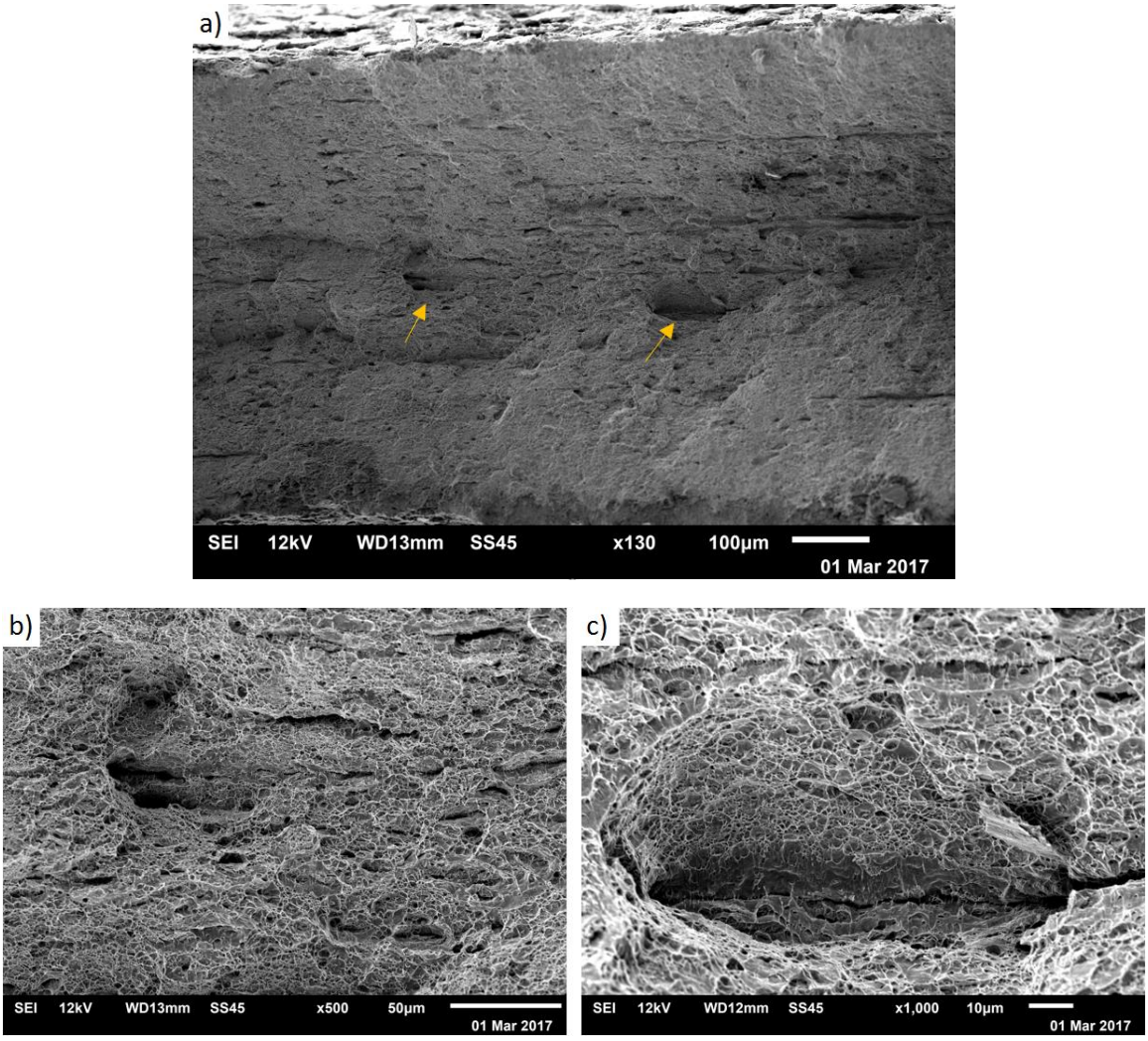

Figure 4-8 Fracture surface of QP980 at a magnification of a)130, b) 500 and c)1000x.

There are areas around the mid-thickness section of the sample that show evidence of the formation of large voids and also cracks aligned parallel to rolling direction. Formation of voids and cracks at the mid-thickness can be attributed to the higher volume fraction of martensite in those areas which leads to crack propagation in martensite or detachment of large martensite clusters. Deformation behavior of martensite phase will be

fully discussed in section 4.7. Figure 4-8 b and c show the areas which are depicted with yellow arrows in Figure 4-8 a at higher magnification. They show that the fracture surface including the surface inside a large void are covered with dimples which confirms the ductile fracture behavior of QP980 steel and shows evidence of high local deformation associated with the formation of large voids.

Figure 4-9 shows fracture surface of hourglass shape tensile specimen used for SEM based in-situ tensile test. Like Figure 4-8, there are large voids on the fracture surface of subsize tensile specimen far from the edges. Three locations were specified on the fracture surface. Location A and B which are close to edges of the fracture surface confirmed the formation of shear dimples. Figure 4-9 c, which is captured at higher magnification compared to other SEM images from the fracture surface, shows dimples with different sizes formed on the fracture surface of QP980. This variety of dimple sizes which ranges from micron to submicron size exists all over the fracture surface.

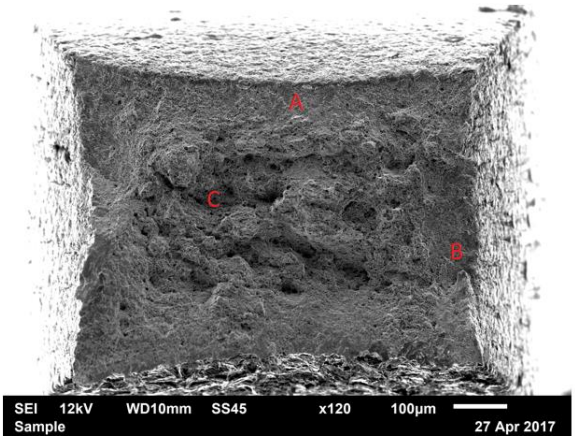

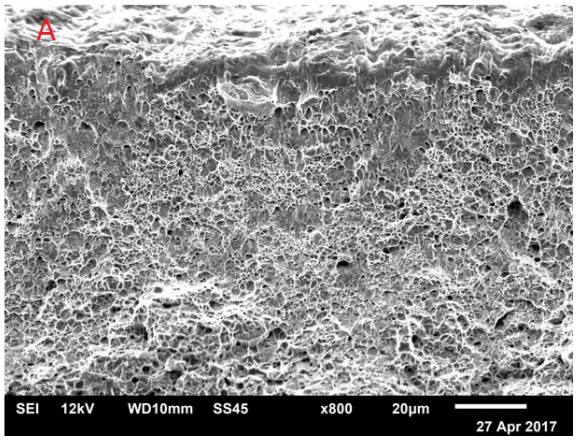

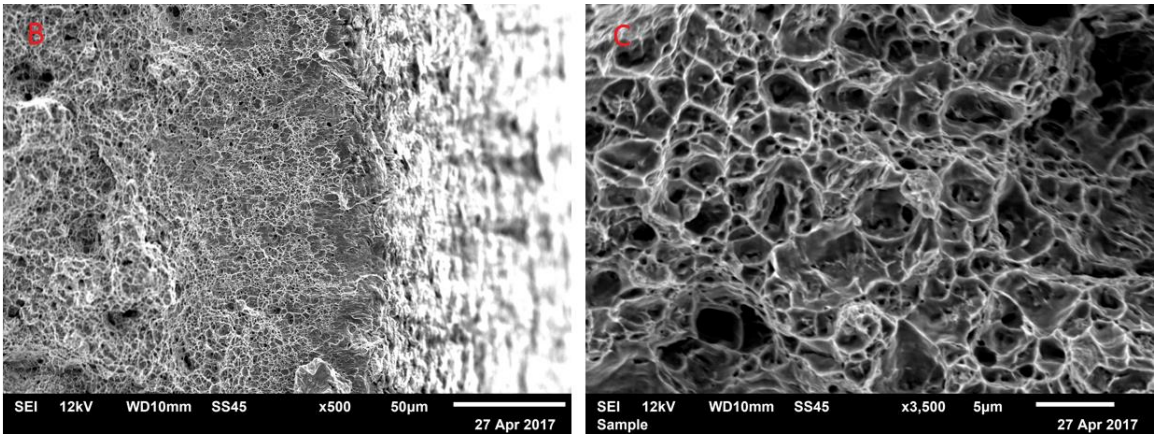

Figure 4-9 Fracture surface of hourglass shape tensile specimen used for in-situ tensile test under SEM.

4.4 Transformation Induced Plasticity (TRIP) effect:

The TRIP phenomena in QP980 steel was studied using two methods including ex-situ tensile tests coupled with XRD and EBSD analysis. XRD analysis coupled with tensile testing was employed to study TRIP effect in retained austenite phase in general. Although XRD method can detect film-like retained austenite which cannot be detected with EBSD method, it does not reveal the nature of the TRIP effect in retained austenite blocks during deformation. Therefore, EBSD analysis coupled with tensile testing was employed to investigate the TRIP effect in the individual retained austenite blocks in the terms of its extent and rate. Finally, a comparison was made between the results obtained from the above mentioned methods.

4.4.1 Tensile testing coupled with XRD:

Table 4-4 shows retained austenite volume fraction measured using ex-situ tensile tests coupled with XRD. According to Table 4-4, the initial retained austenite volume fraction without deformation measured on the surface of hourglass shape specimen is in the good agreement with the value measured with XRD on the thickness of QP980 steel samples discussed in section 4.1.

Table 4-4 Retained austenite volume fraction as a function of true strain measured with XRD method.

	Displacement (mm)	True strain	RA volume fraction (%)	Transformed RA fraction (%)
Uniform deformation	0	0	8.4	0
	0.3	0.07	6.0	29
	0.4	0.14	4.8	43
	0.5	0.22	3.6	58
Post uniform deformation	0.6	0.36	2.6	69
	0.7	0.53	1.6	81
	fracture	0.77	0.6	93

Figure 4-10 shows fraction of RA that is transformed and the residual RA volume fraction as a function of true strain. According to Table 4-4 and Figure 4-10 most of the retained austenite transforms to martensite during the uniform elongation stage rather than

during post uniform deformation since 58% precentage of RA transfoms to martensite before necking commences and only 35% of RA transforms after necking. 7 % of RA, which is equal to a RA volume fraction of 0.6%, remains untransfomed at fracture.

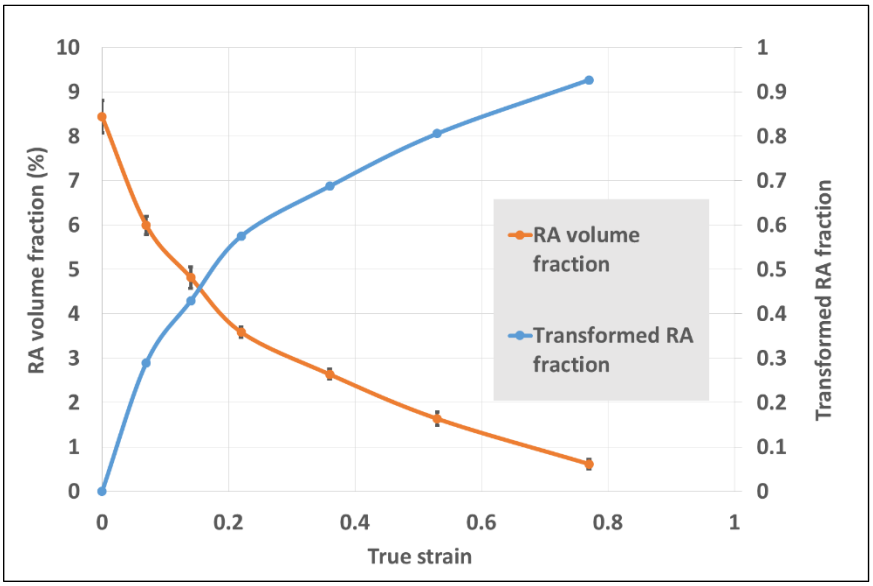

Figure 4-10 Retained austenite volume fraction and transformed retained austenite fraction as a function of true strain.

4.4.2 Tensile testing coupled EBSD analysis:

Figure 4-11 shows the EBSD maps collected on a sample at the same location at different strain levels during the uniform deformation stage. Martensite and ferrite are shown using band contrast and retained austenite phase is shown with red color. Black areas are zero solution regions which did not yield any EBSD pattern. Yellow circles in Figure 4-11 a and b show transformation sequences in retained austenite blocks.

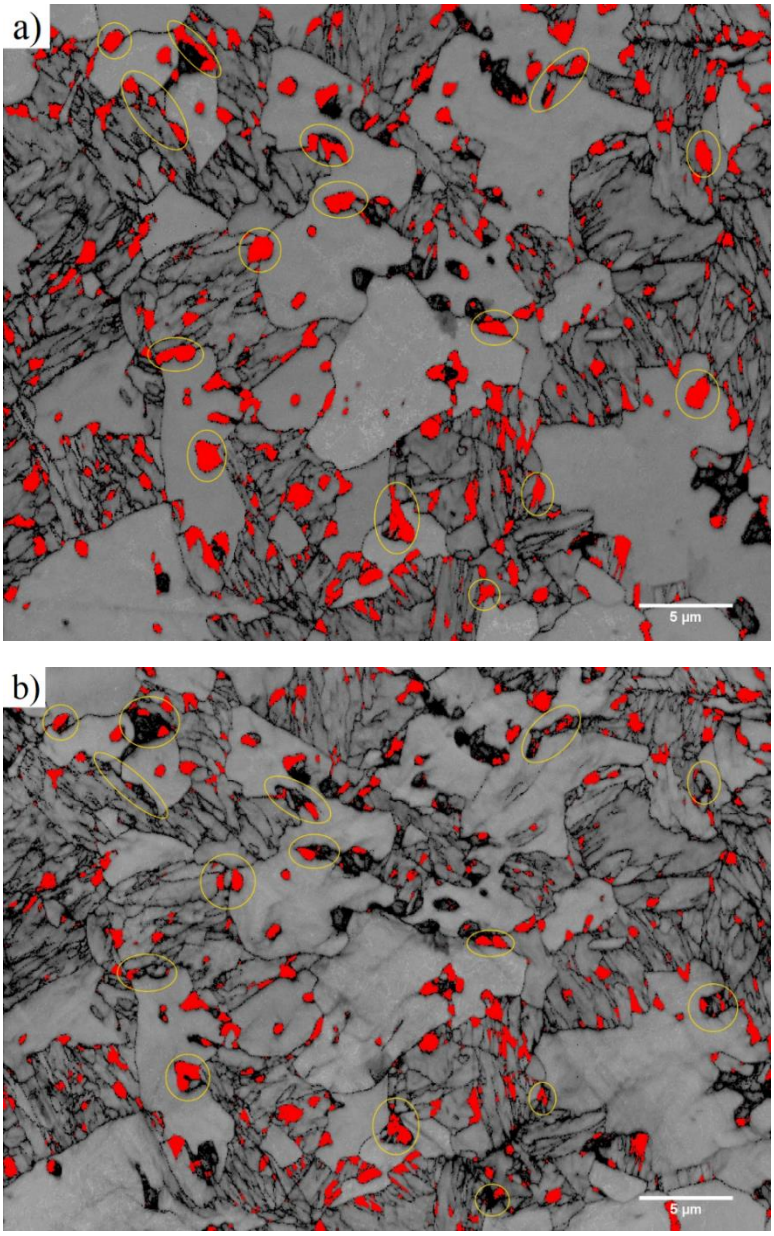
a)
5 µm
b)
5 µm

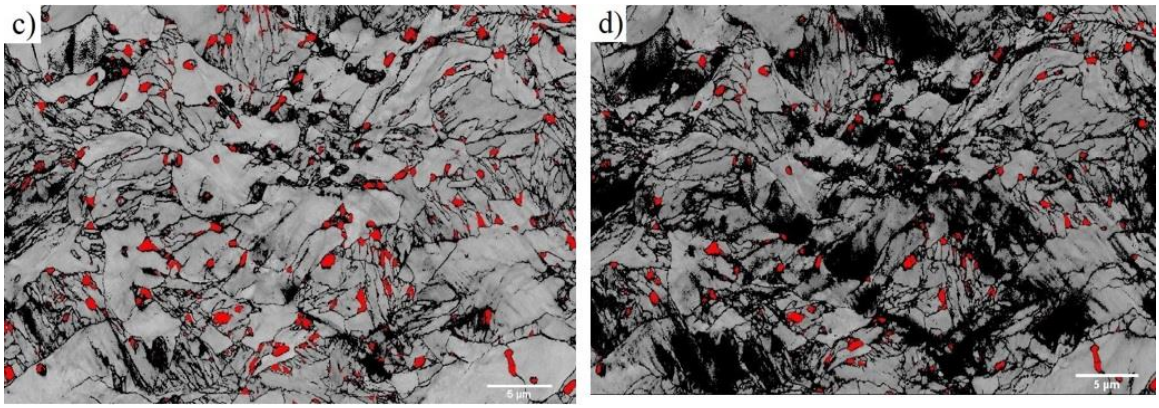

Figure 4-11 EBSD map (band contrast plus retained austenite phase) on the same location at total true strains of a) 0, b) 0.07, c) 0.13 and d) 0.21.

Table 4-5 summarizes the blocky retained austenite, ferrite and martensite together and zero solution phase fraction at each strain. Zero solution volume fraction for the undeformed and deformed sample at total true strain of 7% are 9.1% and 8.3% respectively. These values are in the acceptable and excellent range even after deformation that causes lattice distortion and pattern degradation. It should be noted that the camera exposure time, camera gain and Hough resolution changed from 5.5 ms to 8 ms, 11 to 4 and 70 to 80 respectively from the first image to second image during pattern acquisition and this change led to improvement of EBSD map quality by decreasing the zero solution volume fraction by 0.8%. Despite this, as it can be seen from the Figure 4-11 c) and d) the zero solution volume fraction increases at higher total strain which makes the EBSD map quality inappropriate to track the TRIP effect in retained austenite blocks. Some retained austenite blocks that transform to martensite during deformation are shown with yellow circles in Figure 4-11 a) and b). For the first two images, high volume fraction of transformed

retained austenite blocks were replaced with martensite instead of producing zero solution areas and the volume fraction change in retained austenite and martensite with respect to previous initial EBSD map which are 2% and 2.8% respectively are close to each other. This result shows the acceptable accuracy of EBSD analysis in investigating TRIP phenomena in this range of deformation. The TRIP phenomenon does not happen all at once in the retained austenite blocks and they tend to transform gradually. However, it should be noted that in some of the indicated blocks the transformation is almost complete. Retained austenite blocks located inside the ferrite or at the martensite-ferrite interfaces experience TRIP effect at early stage of plastic deformation due to the higher deformation occurring at those areas. It is worth mentioning that there are blocky retained austenite particles located inside the martensite region which can transform to martensite during deformation and they can lead to work hardening of the martensite phase. According to the XRD results reported in section 4.4.1, 93% of retained austenite had transformed to martensite by the fracture point which include the blocky and film-like retained austenite located within martensite regions.

Table 4-5 Volume fraction of ferrite and martensite, retained austenite and zero solution at different total true strain levels.

phase	Volume fraction in EBSD map %			
	Stage1 (total true strain: 0.00)	Stage2 (total true strain: 0.07)	Stage3 (total true strain: 0.13)	Stage 4 (total true strain: 0.21)
Ferrite and martensite	84.1	86.9	78.1	58.6

Retained austenite	6.8	4.8	2.8	1.4
Zero solution	9.1	8.3	19.0	40

According to Table 4-55 zero solution values reached 19 % and 40% at total true strains of 0.13 and 0.21 respectively. Total true strain of 0.21 corresponds to the point of necking. As can be seen from the Figure 4-11 d) higher deformation areas at total true strain of 0.21 are covered with zero solutions which makes it impossible to track the transformation behavior of retained austenite blocks by this method. Despite this, it should be noted that most of the retained austenite that remained at total true strain of 13.8% and 21.5% tended to have a fine microstructure.

Noise reduction can be performed to clean up the zero solutions areas. This can be performed based on the number of nearest neighbors (NN) value. NN value can range from 1 to 8 and NN value of 5 means only zero solution points that have 5 or higher indexed neighbor points will be filled with the average of orientation of those neighbor points (81). Figure 4-12 shows the effect of noise reduction with NN value of 5 and 1 on the zero solution reduction on the EBSD maps collected at total true strain of 0.13 and 0.21. According to Figure 4-12 a_2 and b_2 noise reduction with NN value of 5 mostly leads to zero solution removal at grain boundaries in martensite islands which also exist in the initial EBSD map without any deformation. It also leads to shrinking the large zero solution areas.

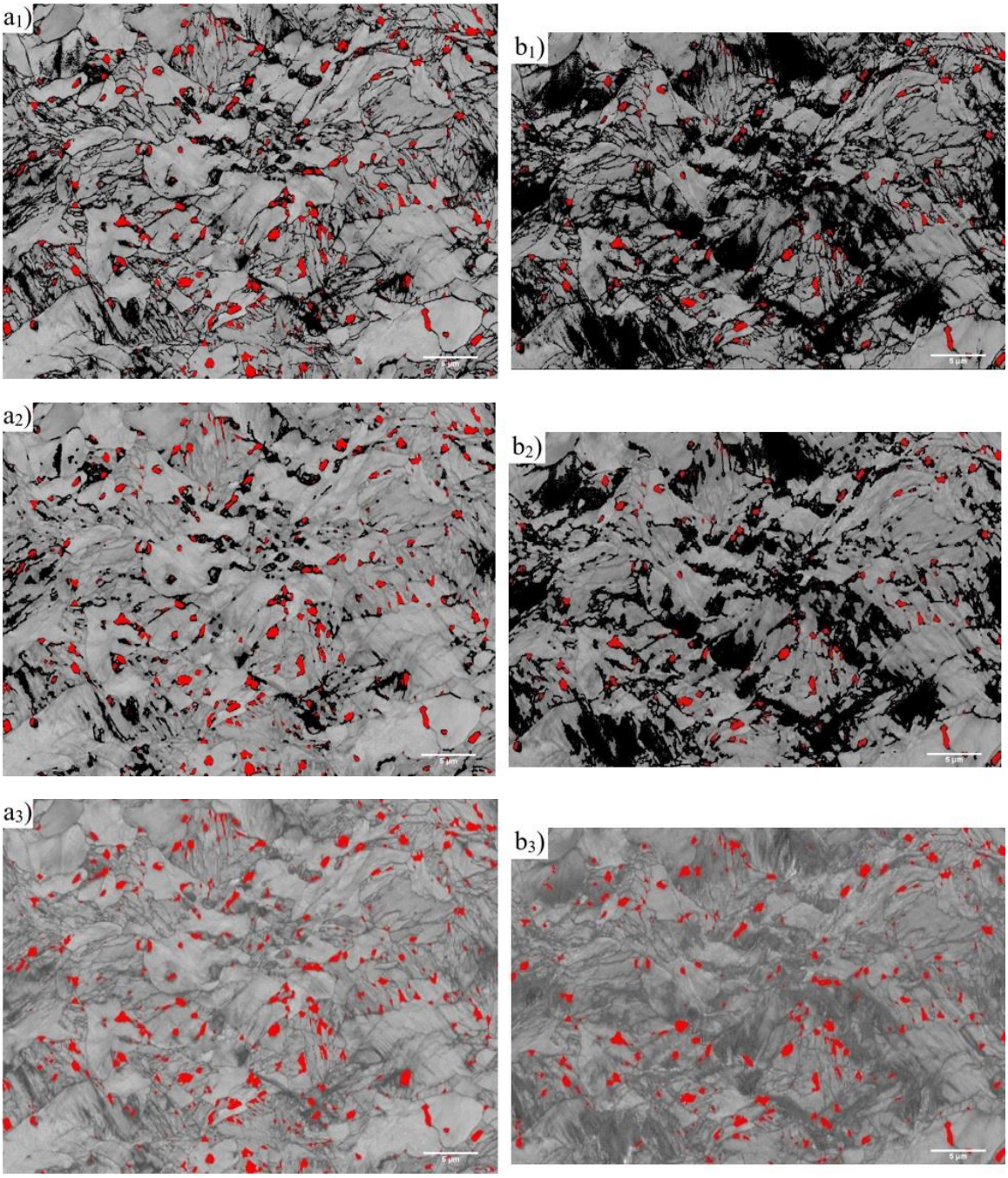

Figure 4-12 Effect of noise reduction with NN value of 1 and 5 on zero solution reduction at two different strain level, a_1=total true strain=0.13 without noise reduction, a_2= total true strain=0.13 and NN=5, a_3= total true strain=0.13 and NN=1, b_1=total true strain=0.21 without noise reduction, b_2=total true strain=0.21 and NN=5, b_3=total true strain=0.21 and NN=1.

According to Table 4-6 noise reduction with NN value of 5 leads to a relative increase in retained austenite volume fraction of 3% and 14% in RA volume fraction with respect to its initial value without noise reduction in the case of EBSD maps with total true strain of 0.13 and 0.21 respectively.

Noise reduction with NN value of 1 eliminates all zero solutions and results in a relative increase of 50% and 142% in RA volume fraction with respect to its initial value without noise reduction at total true strain of 0.13 and 0.21 respectively. As can be observed from Figure 4-12 a_3) and b_3) although noise reduction with NN value of 1 on the two EBSD maps lead to zero solution volume fraction of zero, the previously black areas appear as a very low quality band contrast areas which is more pronounced at total true strain of 0.21. It should be noted that obtaining EBSD map without zero solution is almost impossible.

In conclusion, noise reduction with NN=1 was not considered useful in tracking TRIP effect in retained austenite blocks in this experiment due to the high percentage of produced artifacts and low quality band contrast. Although NN=5 can provide some indication of the nature of the zero solutions, no noise reduction was performed on the obtained EBSD maps to avoid the risk of producing artifacts.

Table 4-6 Effect of noise reduction with NN value of 5 and 1 on the phase volume fraction at total true strain of 0.13 and 0.21.

phase	Volume fraction in EBSD map %					
	Stage3 (total true strain: 0.13)			Stage 4 (total true strain: 0.21)		
	Without noise reduction	With noise reduction		Without noise reduction	With noise reduction	
		NN=5	NN=1		NN=5	NN=1
Ferrite and martensite	78.1	87.3	95.8	58.6	67.7	96.6
Retained austenite	2.8	2.9	4.2	1.4	1.6	3.4
Zero solution	19.0	9.8	0	40	30.7	0

4.4.3 Comparison between XRD and EBSD results:

Table 4-7 compares retained austenite volume fraction measured with XRD and EBSD analysis. As mentioned earlier the retained austenite volume fraction measured with EBSD analysis is lower than the value measured with XRD, which was attributed to capability limitation of EBSD which cannot detect fine microstructure of film-like retained austenite. According to Table 4-7 a relative decrease in volume fraction of retained austenite with respect to the initial undeformed condition measured with each method is the same at true strain of 0.07. However, the relative decrease in retained austenite volume fraction measured with EBSD analysis increases more than that measured with XRD as the

strain level increases which can be attributed to increasing the zero solution volume fraction due to deformation and distortion in crystal lattice. This result confirms the accuracy of EBSD analysis in the range of 0-0.07 true strain for investigating the TRIP effects in retained austenite blocks in QP980 steel. As mentioned in the Section 4.5.1, TRIP effect in retained austenite blocks were successfully detected in the range of 0-0.07 true strain and transformed retained austenite blocks were replaced with martensite instead of producing zero solutions areas.

Table 4-7 Comparison between retained austenite volume fraction obtained with XRD and EBSD analysis at different strain levels.

	Displacement	XRD			EBSD		
		True strain	RA volume fraction %	Relative decrease in RA volume fraction %	Total true strain	RA volume fraction %	Relative decrease in RA volume fraction %
Uniform deformation	0	0	8.4	0	0	6.8	0
	0.3	0.07	6.0	29	0.07	4.8	29
	0.4	0.14	4.8	43	0.13	2.8	58
	0.5	0.22	3.6	57	0.21	1.5	77
Post-unifrom deformation	0.6	0.36	2.6	69	-	-	-
	0.7	0.53	1.6	81	-	-	-
	0.8	0.77	0.6	93	-	-	-

4.5 Damage micromechanism:

Figure 4-13 shows SEM micrographs obtained from in-situ tensile tests coupled with SEM to investigate damage micromechanisms in QP980 steel. Each image is taken in the same region at increasing strain. Figure 4-13 c with the local true strain of 0.2 corresponds to the point of necking. Cracking sequences in ferrite, martensite and retained austenite was shown with red, yellow and green arrows respectively. Formation of circular voids as the result of ferrite cracking were shown with the blue circles in the Figure 4-13 h.

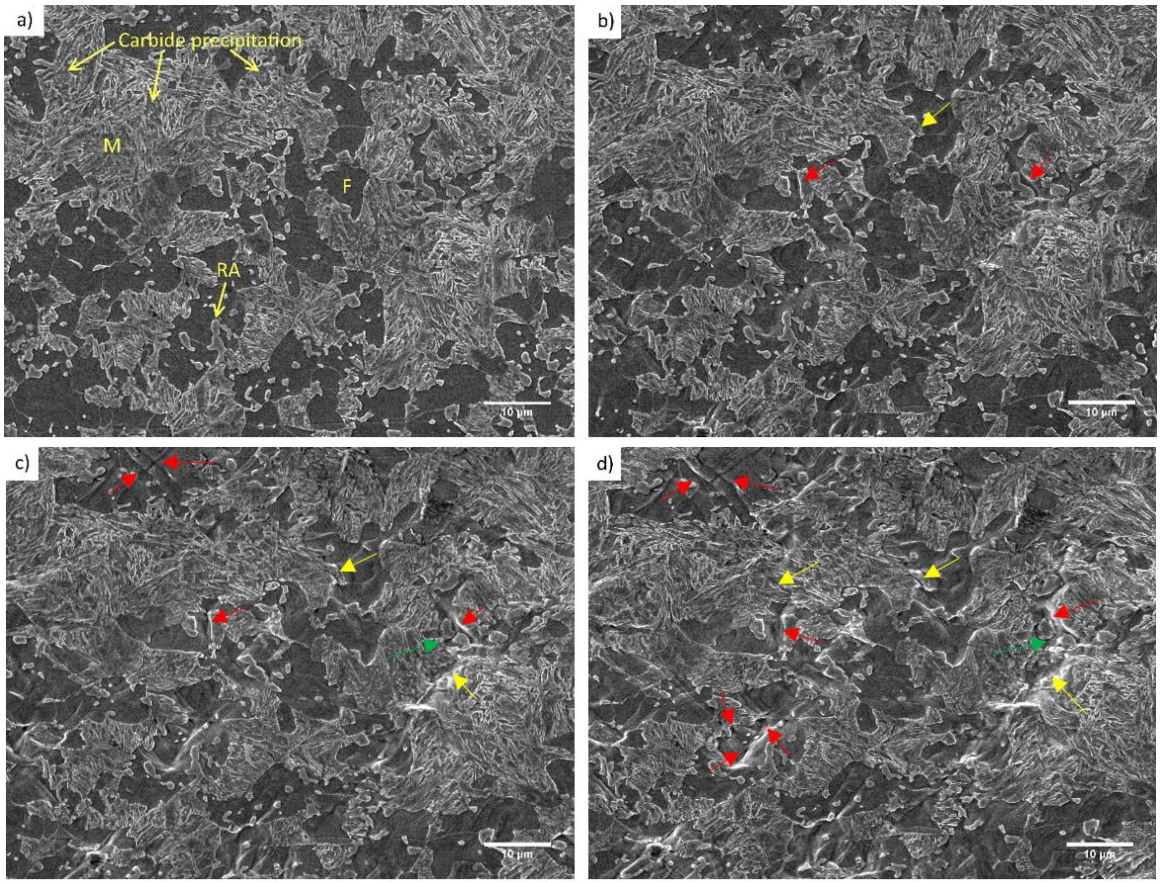

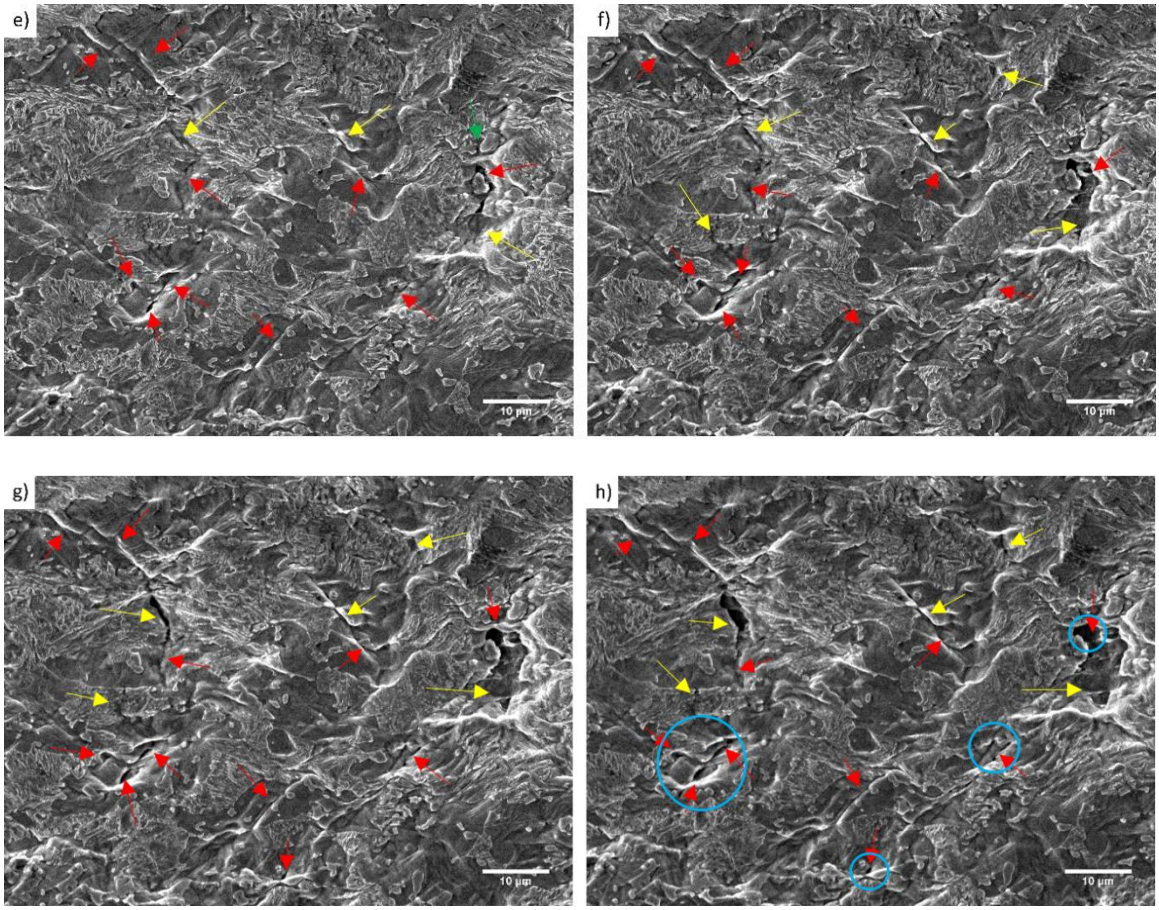

Figure 4-13 SEM based in-situ tensile test micrograph showing damage evolution in QP980 microstructure in local true strain of a) 0, b) 0.13, c) 0.20, d) 0.30, e) 0.44, f) 0.52, g) 0.57, h) 0.62.

According to Figure 4-13 e, f, g and h most of the damage has the form of narrow cracks and surface roughening is aligned in bands formed approximately at 45 degree with respect to loading axis which can be attributed to the stress localization due the shear band formation. According to Figure 4-13 martensite and ferrite cracking happens at approximately the same global strain level; however, damage growth is faster in martensite and it leads to the formation of relatively large cavities. As it can be seen in Figure 4-13 h

crack propagation in martensite causes a separation with the length of approximately 10 µm. Damage occurring in ferrite appears as circular voids (depicted by blue circle in Figure 4-13 h, Figure 4-14 e, Figure 4-15 c, d and e) growing during tensile deformation or narrow cracks. Figure 4-13 e, d, Figure 4-14 b, c, d, e, Figure 4-15 b, c, d and e, contain evidence of the first cracking in the large angular blocky retained austenite (larger than 3 µm in length and 1 µm in width) in a brittle manner at regions experiencing strain localization starting from early stage of necking or uniform deformation (those regions are shown with green arrows). This suggests the probability of their early transformation to martensite. According to EBSD results discussed in section 4.5.2, some of the retained austenite blocks are almost completely transformed to martensite even at local true strain of 0.07. Moreover, as the XRD results (section 4.5.1) showed that retained austenite transformation rate is higher during uniform deformation. Although EBSD results could not confirm the damage evolution as the results of cracking of transformed large retained austenite blocks due to the severe pattern degradation at the point of necking this result suggests the probability of large retained austenite cracking due to their transformation to martensite. It should be noted that despite the cracking of large retained austenite blocks, they usually do not play the key role in crack propagation due to their smaller size and lower volume fraction compared to other phases. Besides, smaller blocky retained austenite particles tend to move with ferrite and martensite islands during deformation without showing cracking although they may transform to martensite during deformation as shown in Figure 4-11 b. Cracking of blocky retained austenite is not associated with significant

amount of deformation compared to ferrite and martensite which will be examined more closely in section 4.6. Figure 4-14 shows a deformation image series in which large blocky retained austenite located at ferrite grain boundary started cracking from early stage of necking and finally separated into 5 parts in a brittle manner. Figure 4-14 b with the local true strain of 0.21 corresponds to the point of necking.

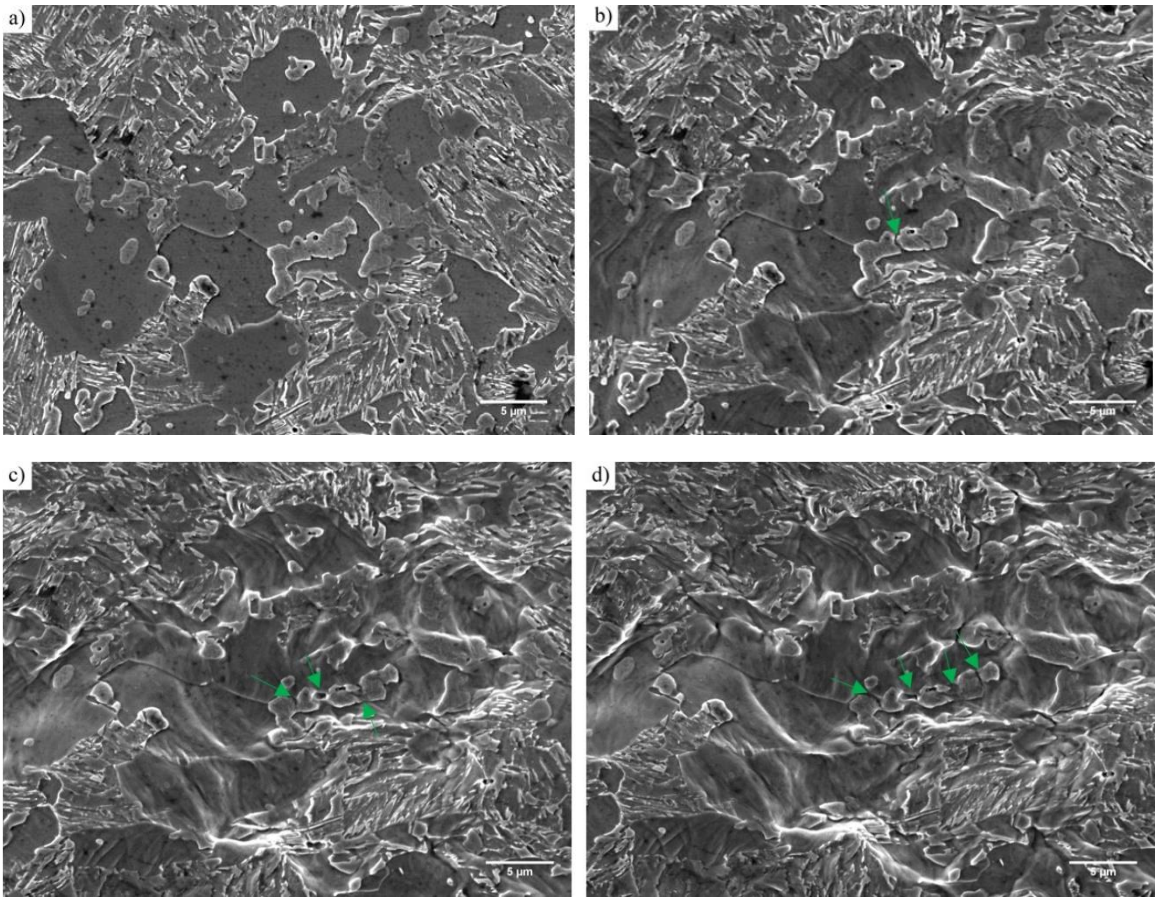

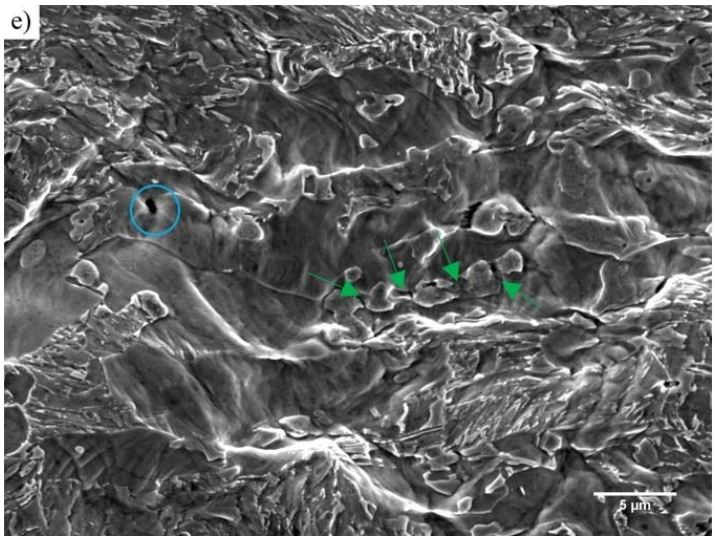

Figure 4-14 SEM micrograph showing damage evolution as the results of large retained austenite cracking located at ferrite grain boundary at local true strain of a) 0, b) 0.21 , c) 0.43, d) 0.54, e) 0.61, blue circle show occurring of circular void in ferrite.

Figure 4-15 shows another example of damage evolution as a result of brittle cracking in large retained austenite blocks that started to occur during uniform deformation at local true strain of 0.1 as shown in Figure 4-15 b. As can be observed, even the ferrite grain which was confined within the retained austenite block could not deform and started to crack simultaneously with large retained austenite block cracking. Another feature that is worth mentioning in this deformation image series, is the growth of a circular void in the very narrow ferrite region confined between two small retained austenite blocks due to subjecting this region to high strain localization as shown in Figure 4-15 c, d and e.

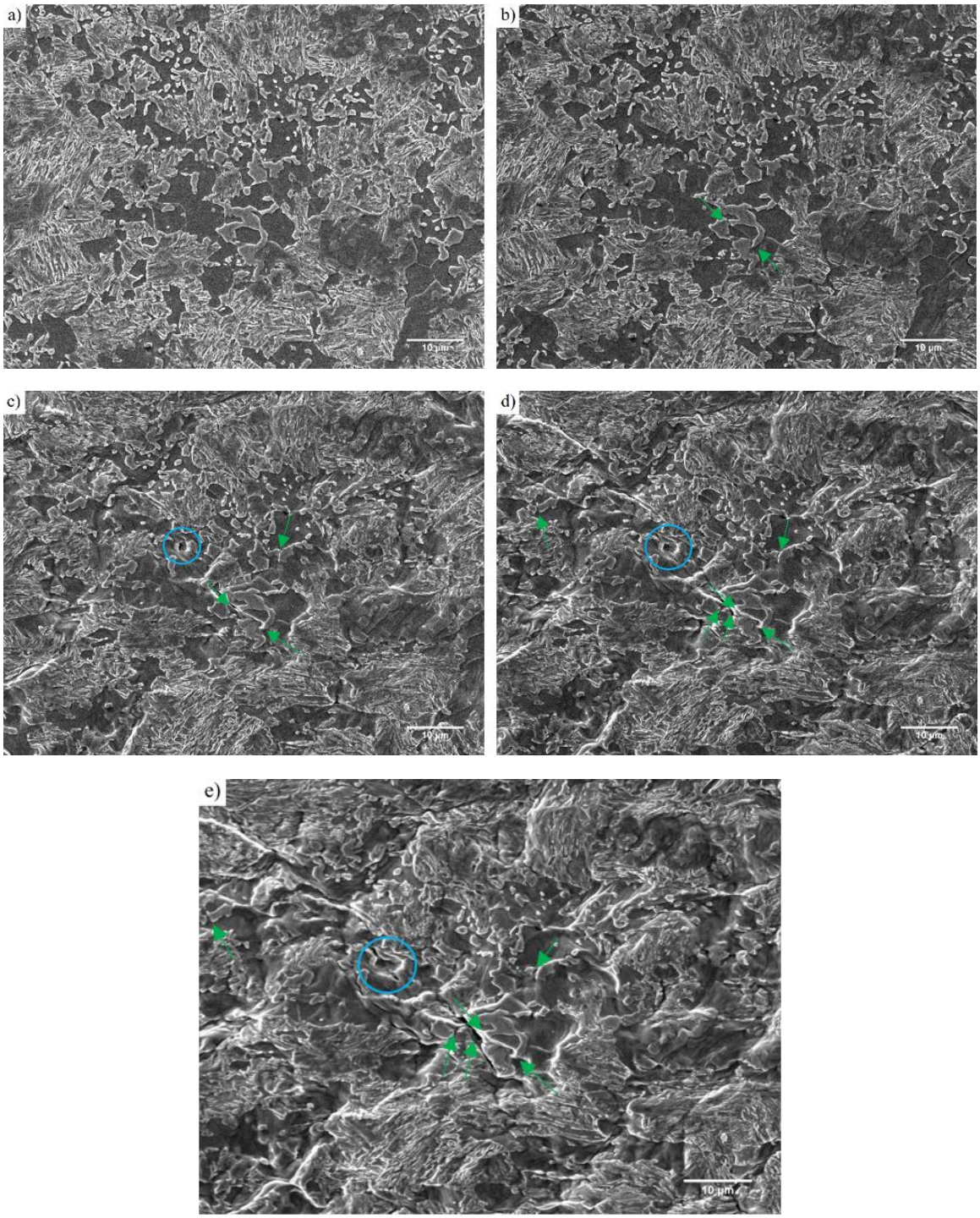

Figure 4-15 Brittle cracking of large retained austenite blocks depicted with green arrows at local true strain of a) 0, b) 0.1, c) 0.30, d) 0.41, e) 0.52. Blue circles showing circular void nucleation sequences in ferrite.

In summary, ferrite and martensite in QP980 undergo substantial deformation and cracking starts at an approximately same total strain level in both phases. However, damage growth rate is faster in martensite which leads to the formation of large cavities, while damage in ferrite appears as narrow cracks and relatively smaller circular voids. Large and angular retained austenite blocks show evidence of brittle cracking in regions experiencing strain localization which initiates during the uniform deformation stage or at an early stage of necking; however, they are not playing a key role in damage propagation due to their small size and low volume fraction. No evidence of interface or particle cracking was observed in small retained austenite blocks and they tend to move with ferrite and martensite during deformation even though they may transform to martensite.

4.6 Micro DIC Results:

Local deformation behavior of each phase has been quantified using the μ-DIC technique. Three image series obtained from different samples were fed to the ARAMIS software to achieve local strain maps to find the strain partitioning between the constituent phases during deformation. The true strain values in this section were reported in the form of ε_x which represents deformation parallel to the loading direction. The first image series consisted of 27 in-situ tensile test images. To get a good strain map from ARAMIS software the amount of deformation in each step should be small enough so that the software can track the facet during deformation; otherwise there will be blank regions in the strain map

or the map could be lost in the worst scenario where the software cannot find any correlation. The same situation occurs when new features like cracks form in the deformation images which appear as a blank region in the strain map. Local true strain tends to increase with higher rate at post uniform deformation. Therefore, there is a need to capture more photos during post-uniform elongation in order to capture strain evolution within the phases. Among the 27 images in the first image series which were fed into ARAMIS, 9 images were captured during uniform elongation and 18 images were captured during post uniform elongation. Figure 4-16 shows average global true strain measured with ARAMIS software in X direction (ε_x) versus stage number.

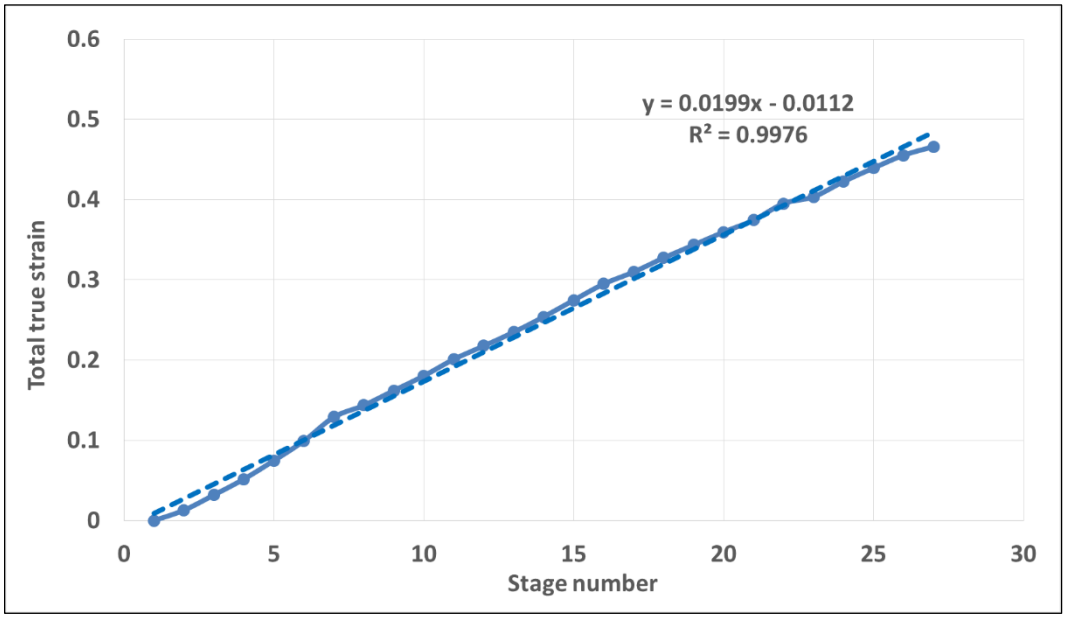

Figure 4-16 Local true strain measured with DIC versus stage number for the first deformation image series.

As seen from Figure 4-16 each step captured small and approximately the same amount of deformation so as to avoid emerging blank regions in the strain map. Also, there

was a linear relationship between global strain and stage number. Each deformation image captured approximately 0.02 total true strain. Facet size and step size were 90 and 80 pixels or 1.5 and 1.3 μm respectively. No interpolation was performed on the strain maps. Figure 4-17 shows strain maps achieved from first image series at different strain levels. Ferrite areas shows higher local true strain values compared to martensite regions and retained austenite blocks. Strain localization tends to occur in regions where ferrite is confined within martensite or retained austenite. Although there are some locations in martensite that show strain values between 0.02-0.07 at total true strain of 0.4 (Figure 4-17 d) and have the dark blue color as the region experiencing lowest strain compared to other locations, there are other regions in martensite that experience strain values between 0.4 and 0.8 shown with green and yellow colors which is close to the average ferrite region strain levels. The noticeable amount of deformation in martensite can be attributed to two important factors including the relatively low carbon content of martensite due to the partitioning and tempering process and TRIP effect that happens in both film-like and blocky retained austenite which are embedded inside martensite. According to Figure 4-17 c and d at higher total strain levels the co-deformation of ferrite and martensite is more pronounced as there are regions in ferrite and martensite that show same strain level, appearing with the green color. Blank regions in the Figure 4-17 c and d appeared as the results of crack propagation and surface roughening that cause features with high brightness in the deformation images.

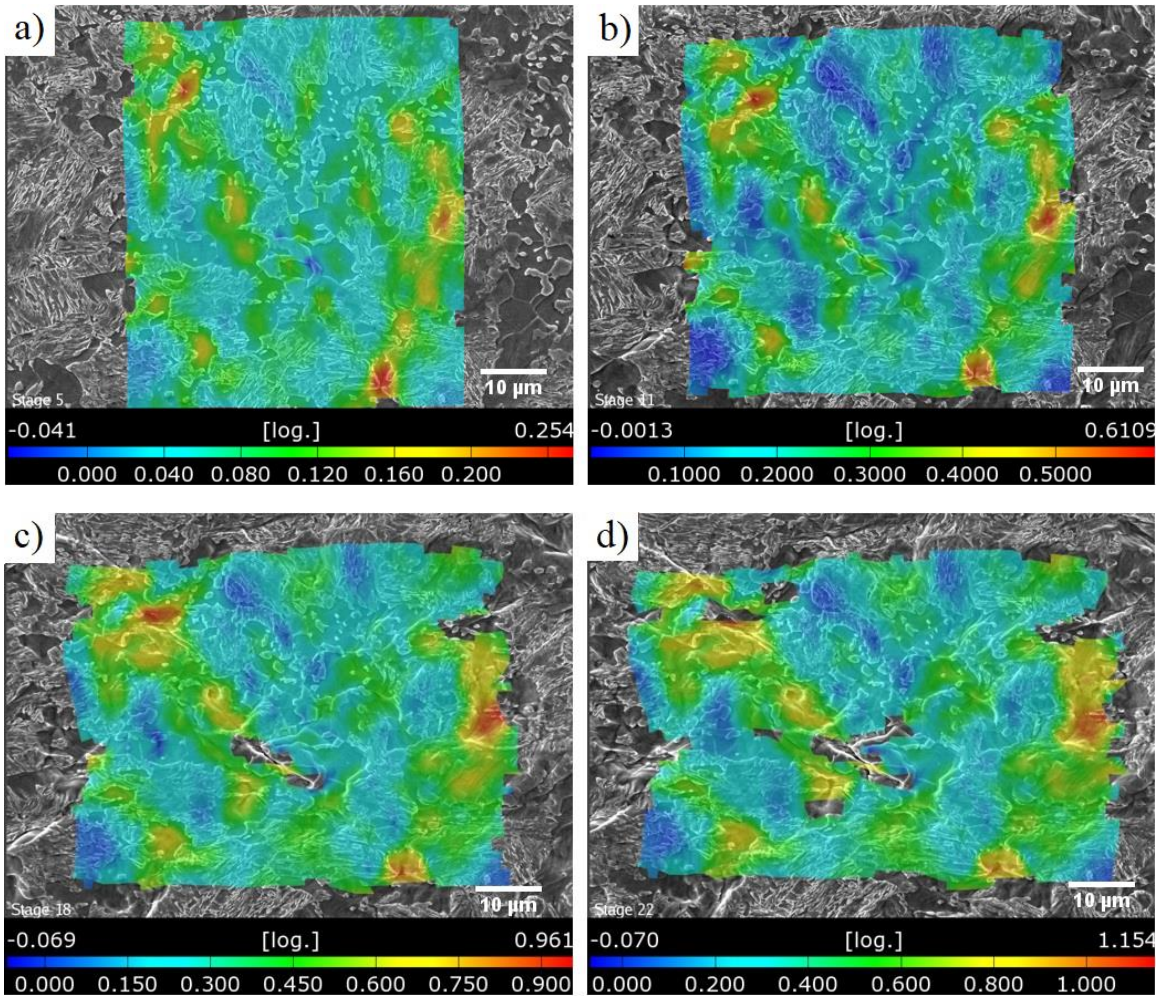

Figure 4-17 Strain partitioning between different constituent phases at average local true strain of a) ε_x=0.07, b) ε_x=0.20, c) ε_x= 0.33 and d) ε_x= 0.40.

Figure 4-18 compares total true strain values measured with ARAMIS software and ImageJ software in each deformation stage. To calculate the total true strain using ImageJ, two features were selected at upper, middle and lower section of the deformation image and the distance between them was measured. Those points were selected in a way that could capture the highest deformation value by remaining in the closest possible location

to the edge of the image at the final deformation stage. The total true strain was measured by calculating average of total strain value measured from each two point. According to Figure 4-18, these two values are close to each other up to stage number 16 as the relative difference between them remains under 1%. However, the relative difference starts to increase after stage 16 and reaches 11% at the final stage which can be related to emergence of blank regions in the strain map due to cracking and appearance of new features like roughening. It should also be noted that separation as a result of cracking is included in the total strain measured with ImageJ even though it is not an actual material strain. Therefore, the real total strain value of this deformation image series is located somewhere between the values measured with ARAMIS and ImageJ. The total strain values measured from ARAMIS calculations were reported until stage 22 while the difference between ARAMIS and ImageJ remain under 5%. Figure 4-17 d corresponds to stage 22. According to Figure 4-15 e which shows the SEM micrograph of stage 27, high amount of surface roughening and cracks led to emerging blank regions strain map and consequently significant error in strain calculations.

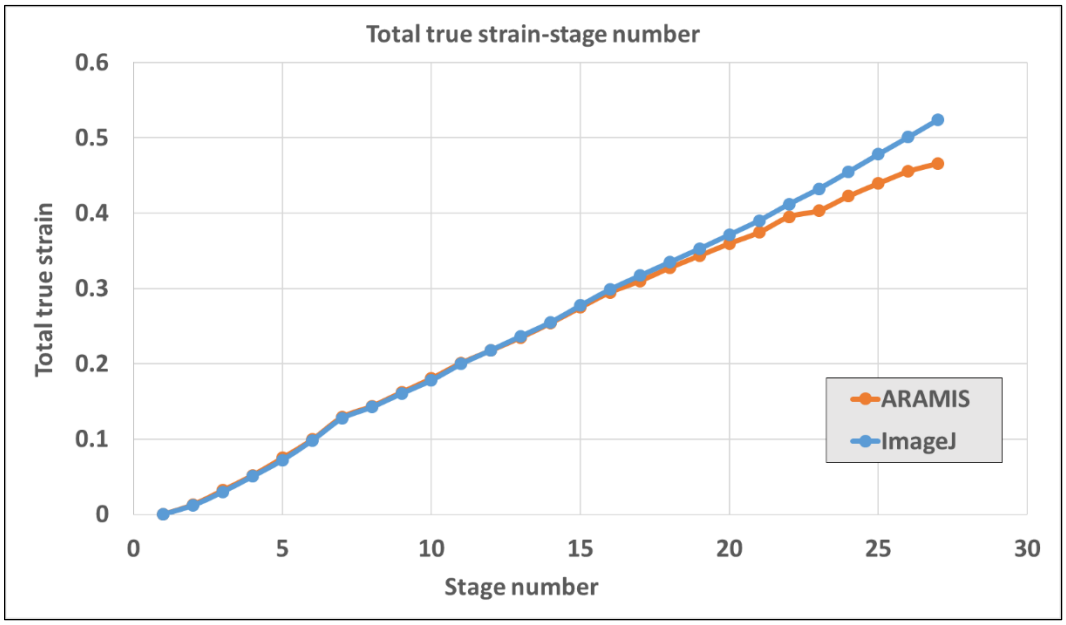

Figure 4-18 Comparison between total true strain measured with ARAMIS and ImageJ software for first deformation image series.

In order to study the strain evolution in each constituent phases, 100 points in martensite, 70 points in ferrite and 15 points in retained austenite were randomly selected to calculate average local strain in each phase in each stage during deformation as shown in Figure 4-19.

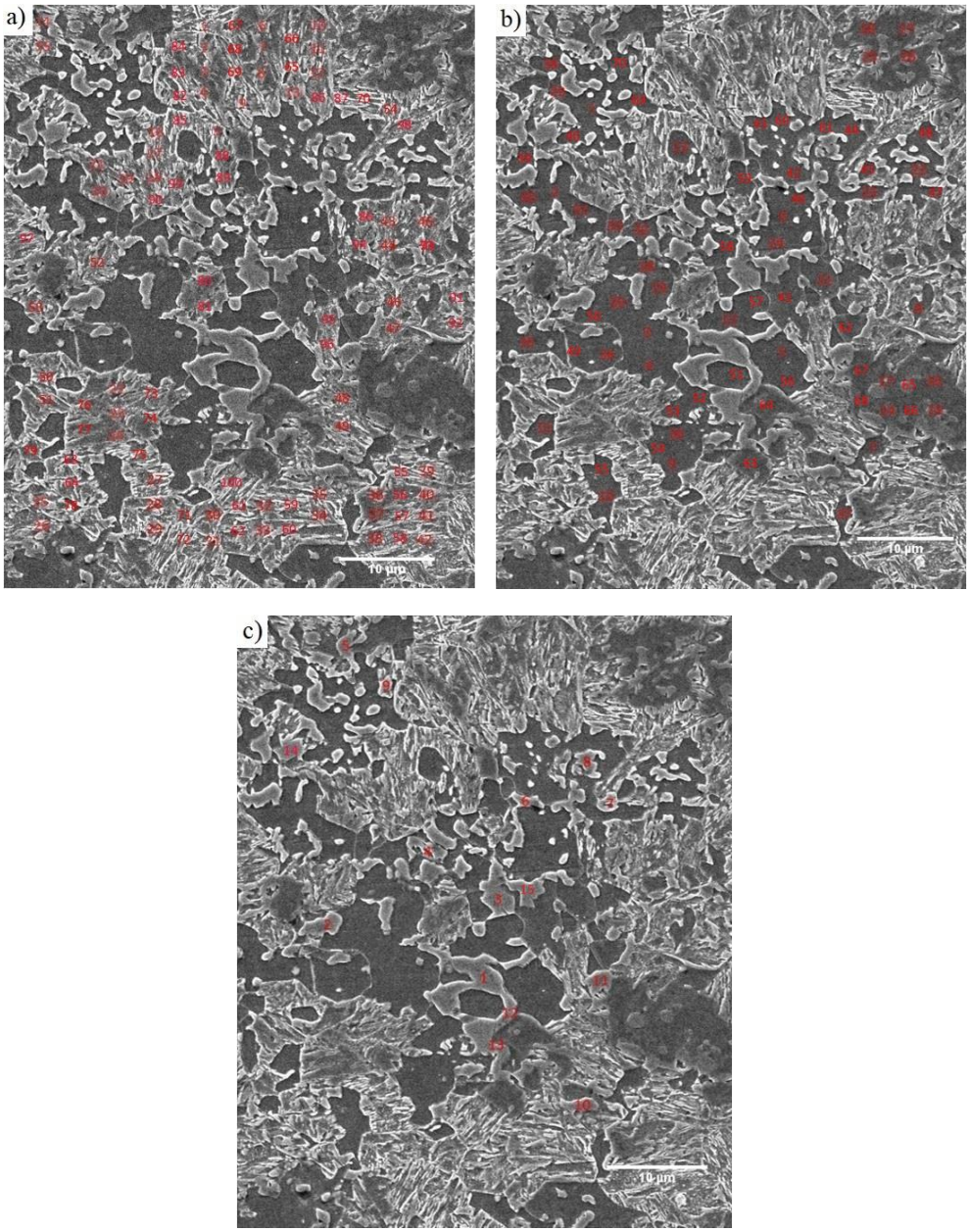

Figure 4-19 Selected points in a) ferrite, b) martensite and c) retained austenite phase to calculate average local strain in each phase.

Figure 4-20 shows two retained austenite blocks which in one of them (Figure 4-20 a) there are facets that are fully located inside retained austenite blocks and the other one

(Figure 4-20 b) shares the facets between itself and ferrite grains. It is worth mentioning that facets which were fully inside retained austenite blocks were selected to perform the strain measurement. Correlation between the facets cannot be achieved by reducing the facet size in order to increase the accuracy of blocky retained austenite local true strain measurement due to the inadequate quality and magnification of the image series.

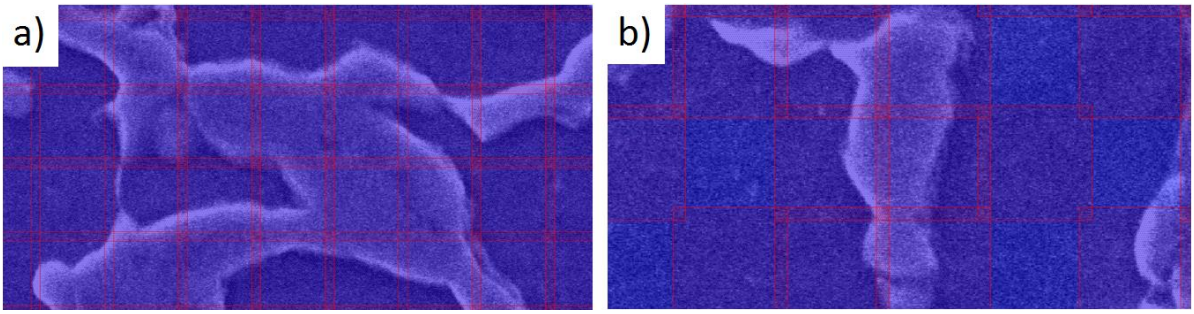

Figure 4-20 Blocky retained austenite a) covered with facets fully located inside it, b) shares the facets with adjacent ferrite grains.

Ferrite and blocky retained austenite volume fraction were measured to be 33.1 % and 10.2% respectively using ImageJ software as shown in Table 4-8.

Table 4-8 Phase volume fraction of the first deformation image series.

Phase	Volume fraction (%)
Ferrite	33.1
Martensite	56.6
Blocky retained austenite	10.2

Martensite region volume fraction was calculated by subtracting the ferrite and blocky retained austenite volume fraction from the whole. The representability of the selected points was investigated by comparing the total strain achieved with the weighted

average of the local strain in each phase using their volume fraction and total strain obtained from the whole strain map as shown in Figure 4-21.

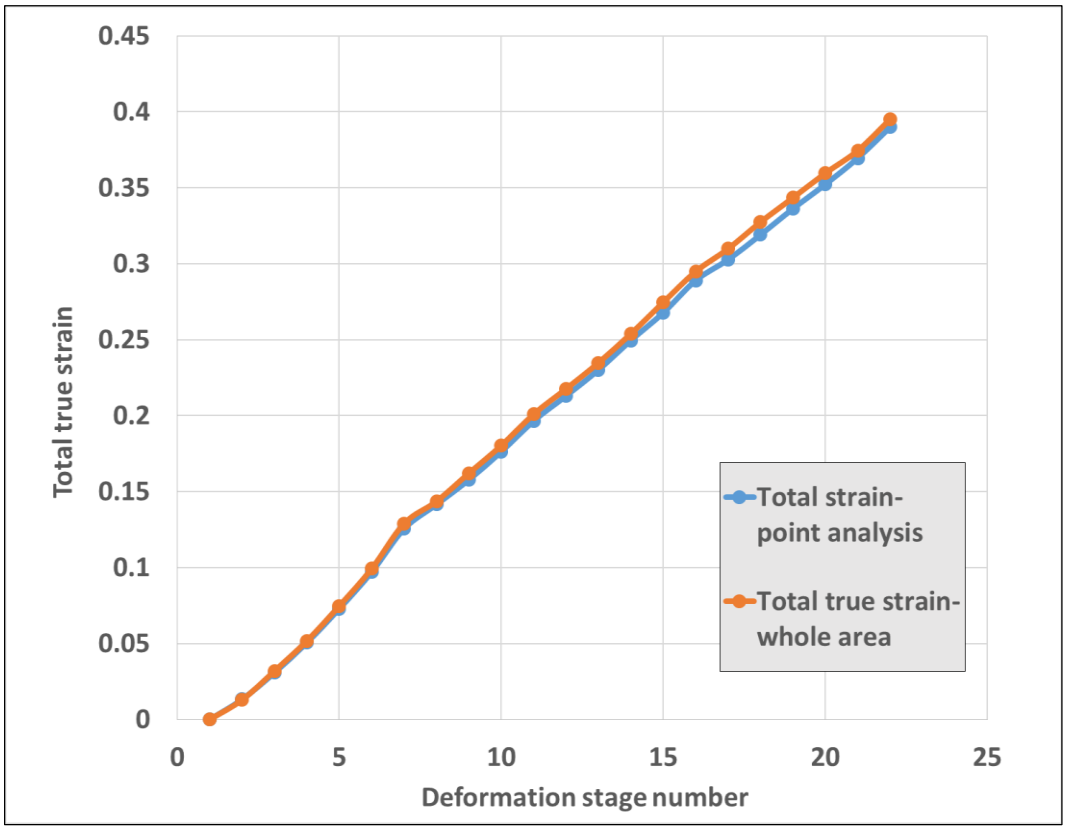

Figure 4-21 Comparison between total true strain obtained from point analysis and the whole strain map for the first deformation image series.

According to Figure 4-21, the values achieved from point analysis is close to the total strain obtained from the strain map as the relative difference of those values remained below 3%.

Figure 4-22 shows average local strain in each phase obtained from point analysis versus total true strain. Local true strains in each phase were reported until a total strain value of 0.4, i.e. up to stage number 22, where the difference between total strain measured

with ImageJ and ARAMIS remained under 5%. According to Figure 4-22, ferrite exhibits significantly higher strain accommodation capability than blocky retained austenite and martensite. The average of ferrite to martensite and martensite to retained austenite local true strain ratios calculated up to a total true strain of 0.4 was 1.7 and 1.5 respectively. The average local true strain at total true strain of 0.14 and 0.4 in each constituent phases are shown in Table 4-9.

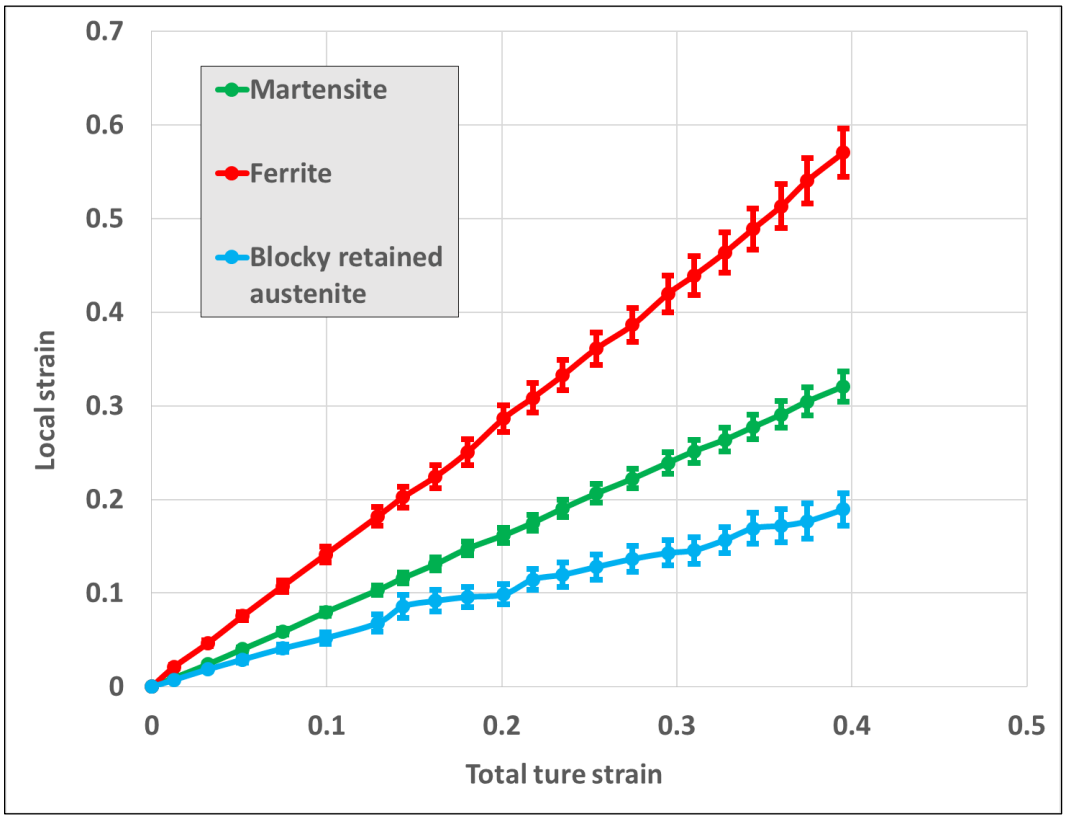

Figure 4-22 Strain partitioning between ferrite, martensite regions and blocky retained austenite during deformation.

According to Table 4-9 the relative increase in local true strain in ferrite and martensite phase from total true strain of 0.14 to 0.4 is approximately equal and higher than

in blocky retained austenite. The lower amount of relative increase in local true strain in blocky retained austenite compared to ferrite and martensite can be attributed to the effect of its transformation to martensite. According to XRD results (section 4.5.1), at total true strain of 0.14, 43% of retained austenite transformed to martensite. Transformed retained austenite percentage reached 69% at total true strain of 0.36. Poling et al. (82) measured carbon percentage of blocky retained austenite and martensite phase in QP980 steel using APT. Results showed that blocky retained austenite contained 1.28 wt. % of carbon while the martensite phase contained 0.037 wt. % of carbon. Therefore, it should be noted that martensite achieved from TRIP effect in retained austenite blocks shows different mechanical behavior compared to martensite in undeformed QP980 due to the difference in their carbon content.

Table 4-9 Local true strain at two different global strain level in the different constituent phases.

phase	Local true strain		Relative increase in true strain %
	Total strain= 0.14	Total strain=0.4	
Martensite	0.13	0.32	146
Ferrite	0.23	0.57	147
Blocky retained austenite	0.9	0.19	111

Figure 4-23 shows cumulative distribution of local strain values in ferrite, martensite regions and blocky retained austenite at the same total strain level of the strain maps shown in Figure 4-17. Strain values in ferrite tend to be distributed over a wider range

compared to martensite and blocky retained austenite which is more pronounced at higher total strain levels. Strain values in blocky retained austenite reaches its maximum values at lower strains compared to other phases.

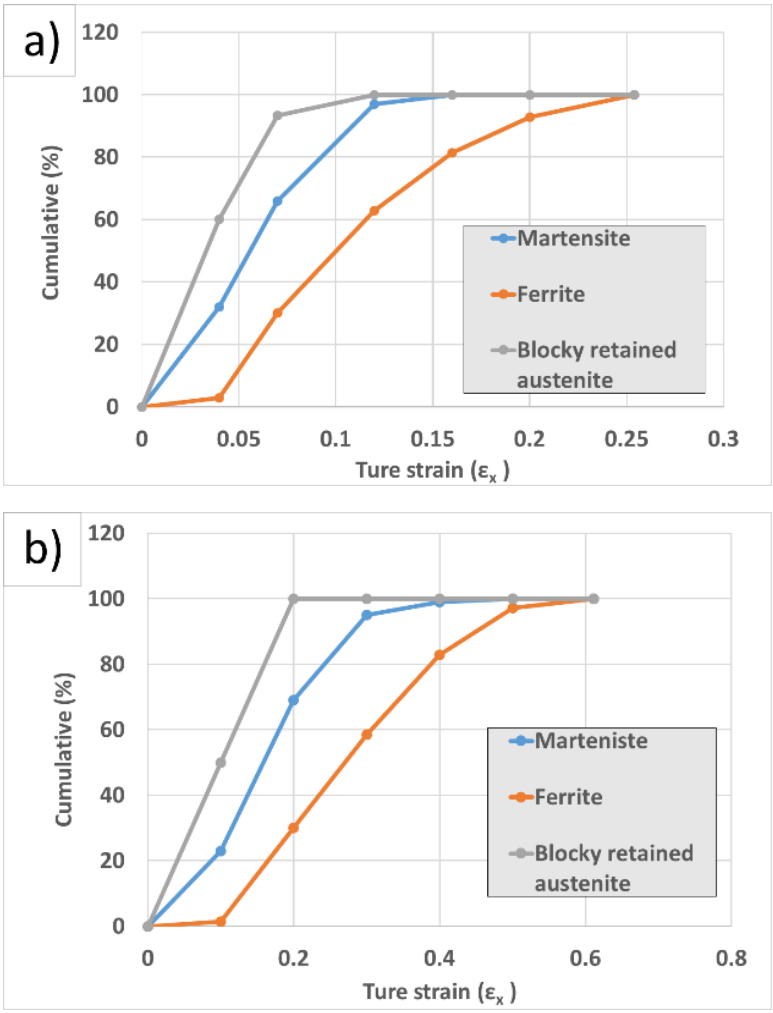

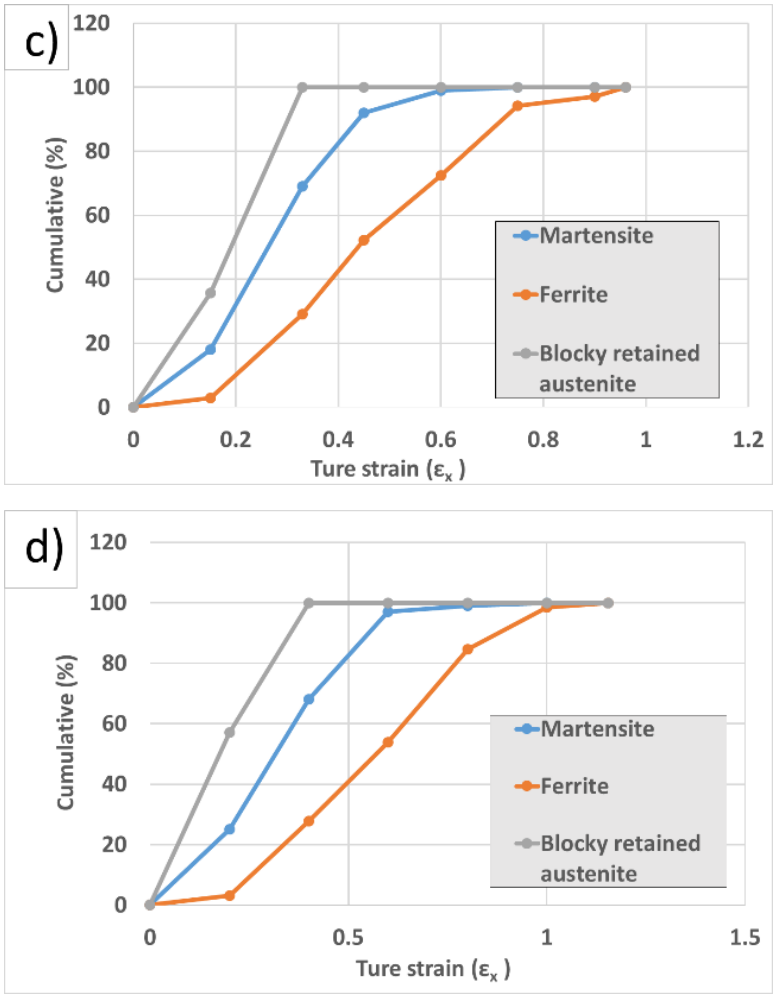

Figure 4-23 Cumulative strain percentage for ferrite, martensite and blocky retained austenite at total true strain of a) 0.08, b) 0.20, c) 0.33, d) 0.40.

The percentage of strain values for each phase above the total strain or average strain of the phases are shown in Table 4-10. Distribution of strain values with respect to average strain in both ferrite and martensite remain approximately the same at each strain level. Retained austenite strain values remain below the average strain at different strain levels except the total strain of 0.07 at which according to EBSD and XRD analysis only

29% of retained austenite transforms to martensite. Martensite also shows slightly higher strain values above the average at total strain of 0.07 which can be affected by the higher deformation capability of retained austenite embedded at martensite region.

Table 4-10 Percentage of the strain values for each phase above the total strain at different strain levels.

phase	Percentage of strain values above the average at different total strain levels			
	Total strain= 0.07	Total strain= 0.20	Total strain= 0.33	Total strain= 0.40
Ferrite	70	70	71	72
Martensite	34	31	31	32
Retained austenite	7	0	0	0

The first deformation image series had a blocky retained austenite volume fraction of 10.2% which was 20% higher than the total volume fraction of retained austenite calculated with XRD. Another image series with higher volume fraction of martensite, lower volume fraction of blocky retained austenite with the same magnification compared to first image series was fed to ARAMIS software to investigate the effect of martensite volume fraction on its deformation capability. It should be mentioned that the second deformation image series was captured from a different sample.

Figure 4-24 shows the strain maps achieved from second deformation image series which consists of 23 SEM micrographs. Facet size and step size used for the calculation of strain map was 90 pixels (1.5 µm) and 80 pixels (1.3 µm) respectively. Strain partitioning

measurements for this deformation image series were performed until stage 14 at which point the total true strain measured with ARAMIS was 0.35 and the difference between total true strain measured with ARAMIS and ImageJ was less than 5%. According to Figure 4-24 a and b at lower total strain levels strain localization mostly happens in the ferrite regions. However, at higher strain levels strain localization occurs at martensite regions as well. It should be noted that the hot spot formed at total true strain of 0.26 (figure c) is approximately aligned at 45 degree with respect to loading axis which may suggest the occurrence of strain localization due to shear band formation. Although low carbon martensite phase in QP980 steel can accommodate high strain levels which is comparable with strain values in ferrite regions, strain localization in martensite can lead to formation of large voids with the approximate dimension of 10 µm, especially in the locations with higher martensite volume fraction as it is shown in Figure 4-13 f.

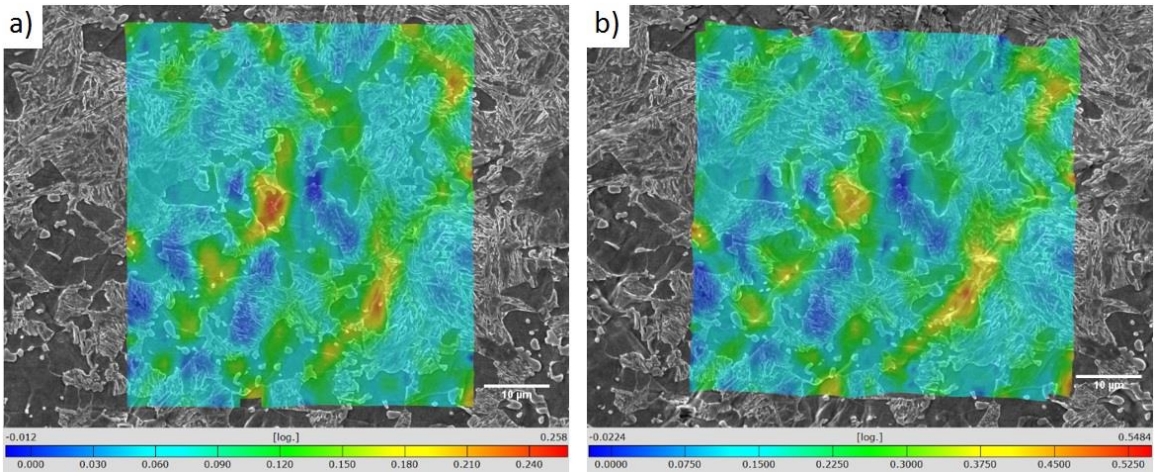

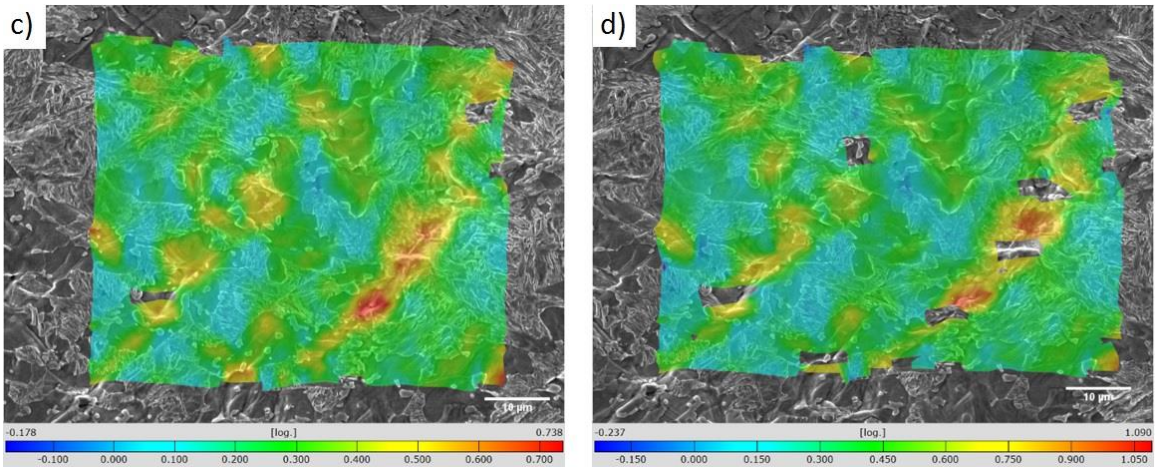

Figure 4-24 Strain evolution in the constituent phases at total true strain of a) ε_x=0.08, b) ε_x=0.18, c) ε_x=0.26, d) ε_x=0.35.

According to Figure 4-13 e-f, higher strain levels leads to formation of voids in martensite regions which makes the strain mapping impossible. Figure 4-25 shows the comparison between total strain measured with ARAMIS and ImageJ. The difference between total strain measured with ARAMIS and ImageJ software ranges between 0 and 0.16 until stage 14 where the relative difference between total true strain measured with the two above mentioned methods remains less than 5%.

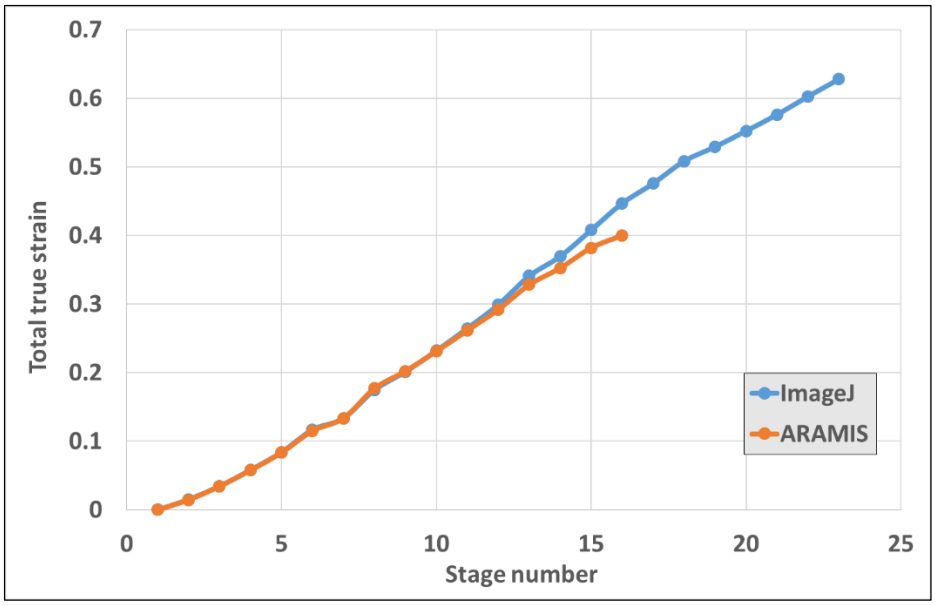

Figure 4-25 Comparison between total true strain measured with ARAMIS and ImageJ software.

Table 4-11 shows volume fraction of the phases in strain map region measured with ImageJ. Volume fraction of martensite is 7.8% more than average volume fraction of martensite. However, the volume fraction of blocky retained austenite is more than two times less than volume fraction of blocky retained austenite compared to the first image deformation.

Table 4-11 Phase volume fraction of the second deformation SEM image series.

phase	Volume fraction
Ferrite	31.2
Martensite	64.4
Blocky retained austenite	4.4

Strain evolution in ferrite and martensite in the second strain map was investigated using the point analysis in which 63 points and 32 points were randomly selected in martensite and ferrite respectively as shown in Figure 4-26. To select the points, an 11×17 grid was superimposed on the strain map area of the deformation image series and the grid points located inside martensite and ferrite were selected for strain measurements. No point was selected in blocky retained austenite particles due to their small size and low volume fraction that needs lower facet size to measure the pure strain accommodation capacity of them which is not affected by the deformation of the adjacent phases.

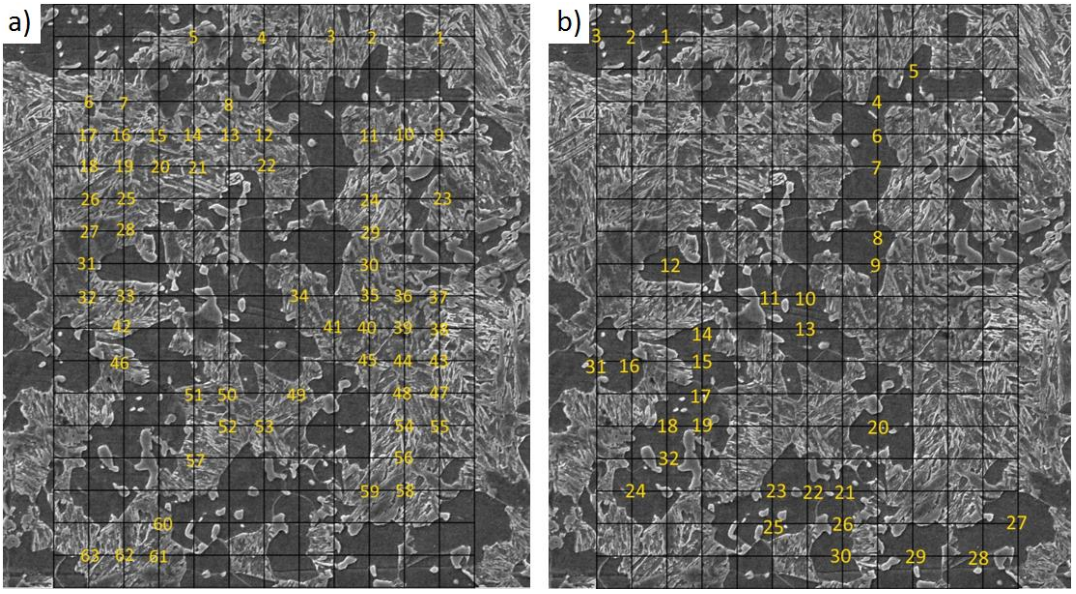

Figure 4-26 Randomly selected points in ferrite and martensite for strain measurements in second deformation image series.

The average local true strain values in ferrite and martensite obtained from the first and second deformation image series are compared in Figure 4-27. Martensite local true strain values in first and second strain map are approximately the same for total strain values lower than 0.1. However, martensite regions in second strain map experiences higher

local strains compared to the martensite phase in first strain map at total strains above 0.1. This difference is more pronounced at higher strain levels where the strain localization happens in martensite regions in the second strain map. This can be attributed to the 7.8% higher volume fraction of martensite in second strain map compared to first strain map.

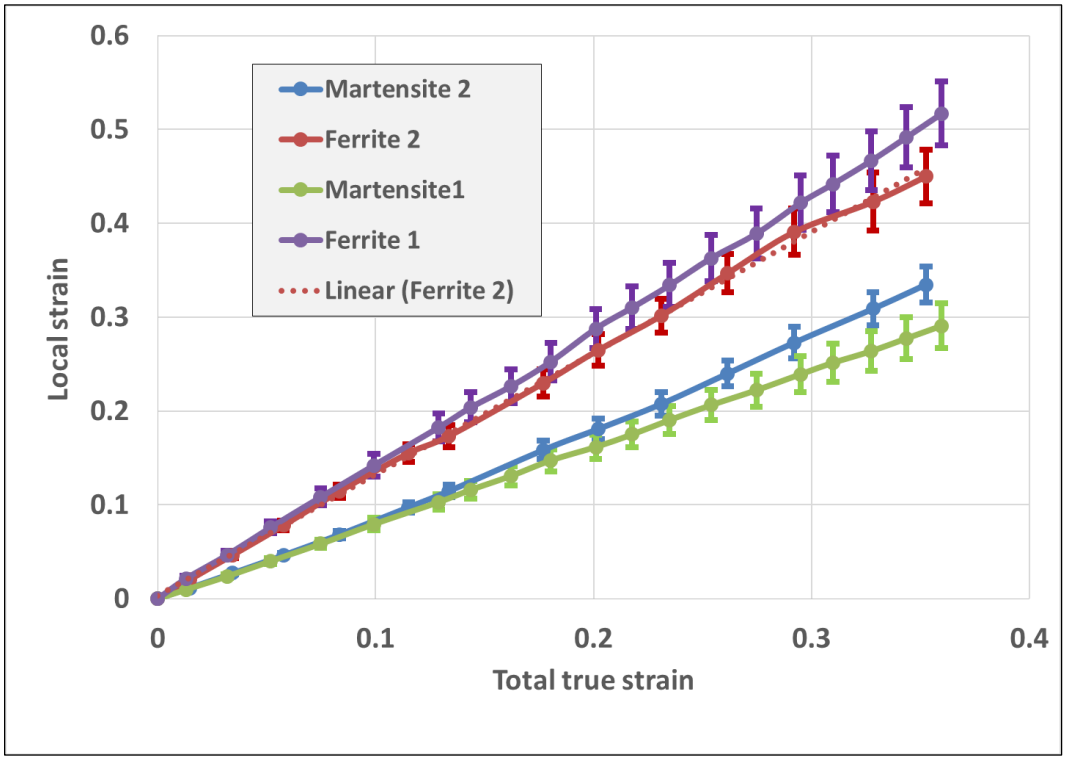

Figure 4-27 Comparison between local true strain values in ferrite and martensite obtained from first and second strain maps. Martensite 1 and ferrite 1 denote strain values achieved from the first strain map. Martensite 2 and ferrite 2 were obtained from the second strain map.

Table 4-12 compares strain values in ferrite and martensite phase at total true strain of 0.33 in the first and second image series. The relative difference in local true strain of martensite and ferrite in first and second strain maps are 19% and -6% respectively. Despite strain localization in the martensite region in the second strain map, ferrite accommodates

lower strain compared to the first strain map. This can be related to fewer places in the second strain map in which a relatively small volume of ferrite is confined within a martensite region that leads to strain localization in ferrite. In addition, martensite accommodates considerable amount of deformation itself.

Table 4-12 Average local true strain in ferrite and martensite at total true strain of 0.33 in first and second strain maps.

Phase	Average local true strain		Relative difference
	First strain map	Second strain map	
Martensite	0.26	0.31	19%
Ferrite	0.47	0.42	-11%

Table 4-12 and Figure 4-28 show the distribution of local true strain values in ferrite and martensite at total true strain of 0.08 and 0.35.

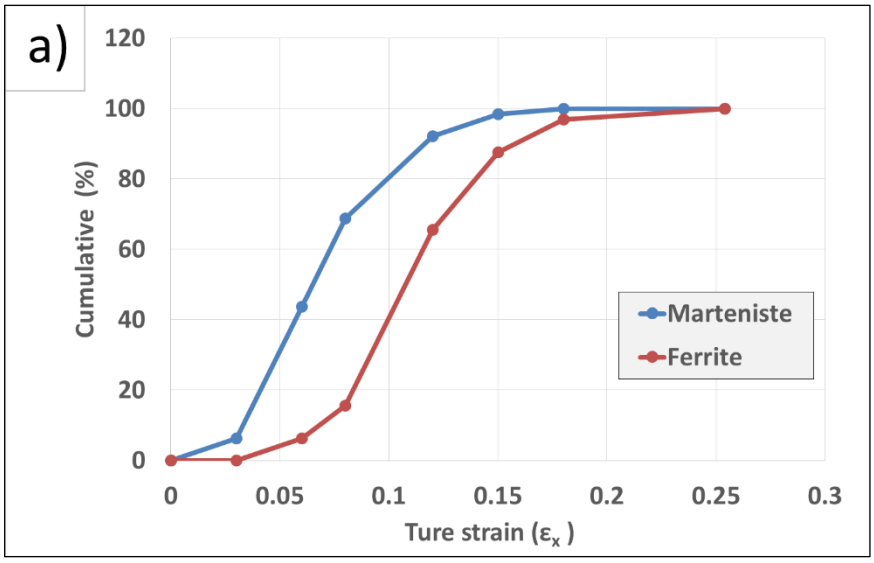

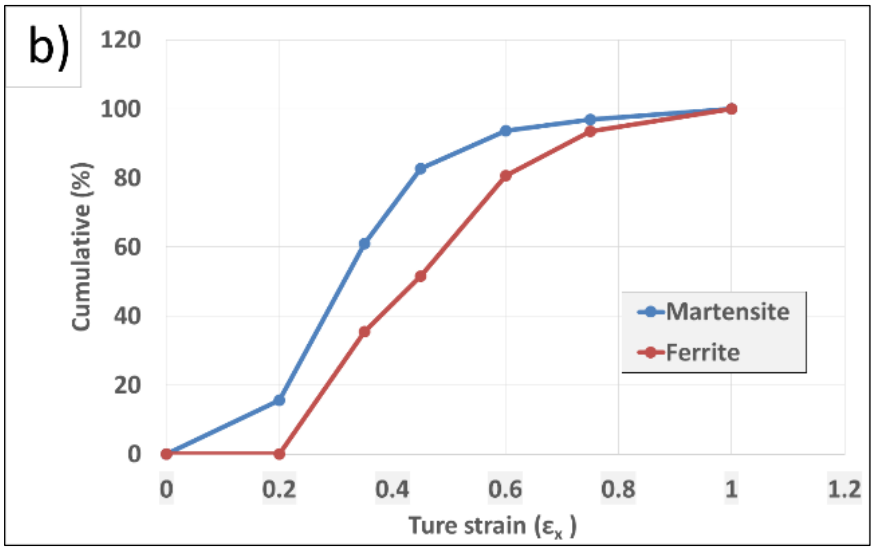

Figure 4-28 Cumulative strain distribution in ferrite and martensite at total true strain of a) 0.08 and b) 0.35.

In addition, martensite and ferrite strain distributions are closer together after a total strain of 0.35 compared to the case after a total strain of 0.08. This suggests that strain partitioning is initially quite high but there is increased homogenization as deformation proceeds. Table 4-13 shows cumulative strain values percentage for ferrite and martensite below the average strain at total strain of 0.08 and 0.35. This increased from 15% at total strain of 0.08 to 35.4% at total strain of 0.35. This is another way to demonstrate that that at the higher total strain of 0.35 there the strain differential between martensite and ferrite has reduced.

Table 4-13 Ferrite and martensite local strain values below the total average strain at total strain of 0.08 and 0.35.

Phase	Percentage of strain values below the average	
	Total true strain= 0.08	Total true strain=0.35
Ferrite	15.6%	35.4%
Martensite	68.7%	60.9%

SEM deformation image series used in first and second strain maps were captured at a magnification of 1500x. Local true strain in blocky retained austenite was successfully measured until a total strain of 0.4 in first strain map due to its higher volume fraction compared to the average volume fraction of retained austenite and also their large size which enabled the retained austenite blocks to accommodate the appropriate size facets and makes it possible to track the facets in blocky retained austenite during deformation.

Another image series was captured at a magnification of 3000x in order to investigate the micromechanical behavior of blocky retained austenite in more detail. The third deformation image series consisted of 24 images. Strain measurements with ARAMIS software were performed until stage 9 where the difference between total strain measured with ARAMIS software and ImageJ remained under 5%. The facet size and step size used for the calculation of strain maps were 60 pixel (1 μm) and 50 pixel (83 μm) respectively. Figure 4-29 compares total true strain measured with ARAMIS and ImageJ software. The difference between two measurements remains less than 0.01 until stage number 9.

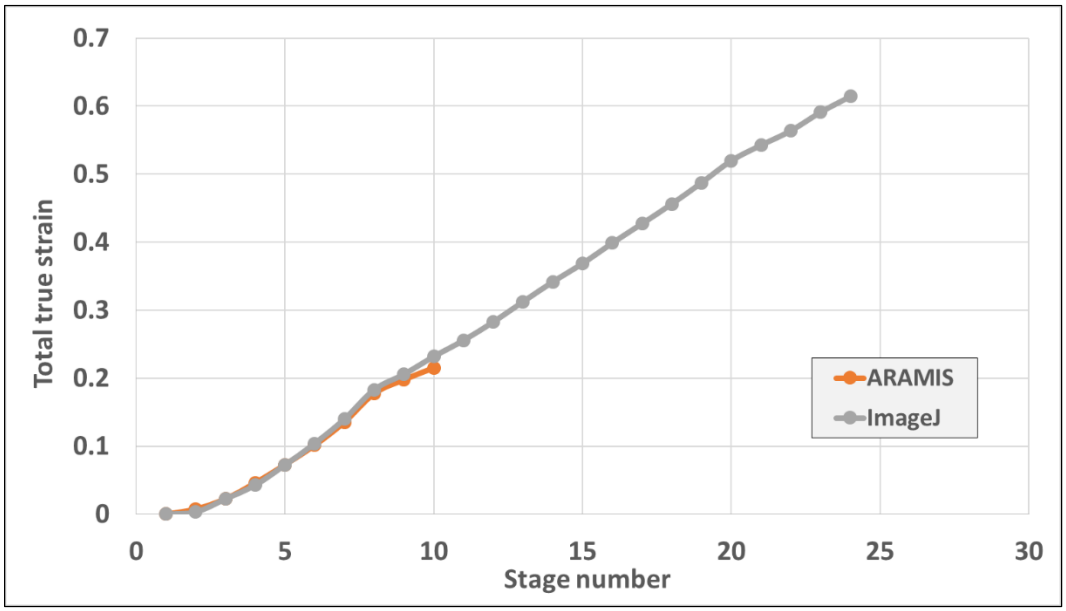

Figure 4-29 Comparison between total true strain measured with ARAMIS and ImageJ software.

Figure 4-30 shows local strain map achieved from ARAMIS software at total true strain of 0.07 and 0.2. Three locations where strain localization occurred around them are specified in Figure 4-30 a and b. Location 1 shows the ferrite phase confined within the three large and angular retained austenite blocks. Location 2 shows the ferrite phase located between a circular retained austenite block and martensite region and finally Location 3 shows a ferrite grain surrounded with two martensite regions that are perpendicular to the loading direction. According to Figure 4-30 b), stress localization in the large blocky retained austenite located at the left side of ferrite phase at location 1 led to its cracking. The local true strain in the cracked blocky retained austenite was measured to be 0.16 and 0.05 at the right and left part. There is a possibility of non-uniform carbide distribution in the large blocky retained austenite that led to its non-uniform deformation behavior.

Deformation in circular retained austenite block up to true strain of 0.24 led to the stress relaxation at the retained austenite block without showing any sign of cracking and strain level in ferrite phase at location 2 remained lower than ferrite phase at location 1 in Figure 4-30 b. Ferrite phase at location 1 continued to deform which led to strain localization up to 0.5 and strain values in the isolated martensite region located at the left side of the ferrite grain remained less than 0.07. According to Figure 4-14 which shows the deformation location at total true strain of 0.61, large blocky retained austenite located at the left side of ferrite phase at location 2 fractured in a brittle manner into 5 parts.

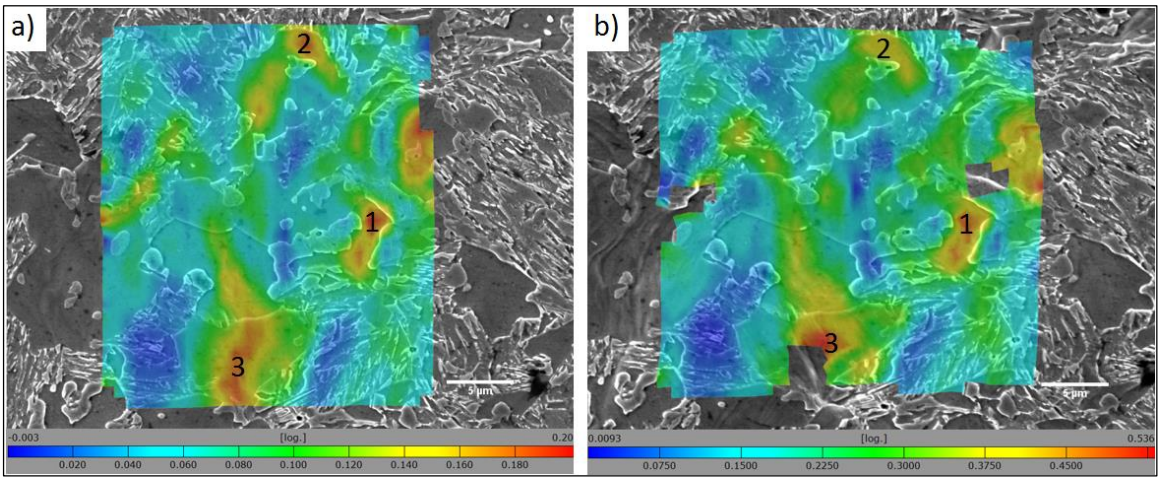

Figure 4-30 Strain partitioning between the constituent phases at local true strain of a) 0.07 and b) 0.20.

Phase volume fraction of the strain map region measured with ImageJ is shown in Table 4-14. Volume fraction of ferrite in the strain map region is 6.6 % higher than the average volume fraction of ferrite in the steel.

Table 4-14 Phase fraction of constituent phases at strain map area measured with ImageJ.

Phase	Volume fraction %
Martensite	50.7
Ferrite	39.6
Blocky retained austenite	9.7

In order to compare the local strain values obtained from third strain map with local strain values of the two previous maps, 54 points in martensite, 37 points in ferrite and 12 points in blocky retained austenite were randomly selected to calculated average strain level of each phase in each deformation stage as shown in Figure 4-31.

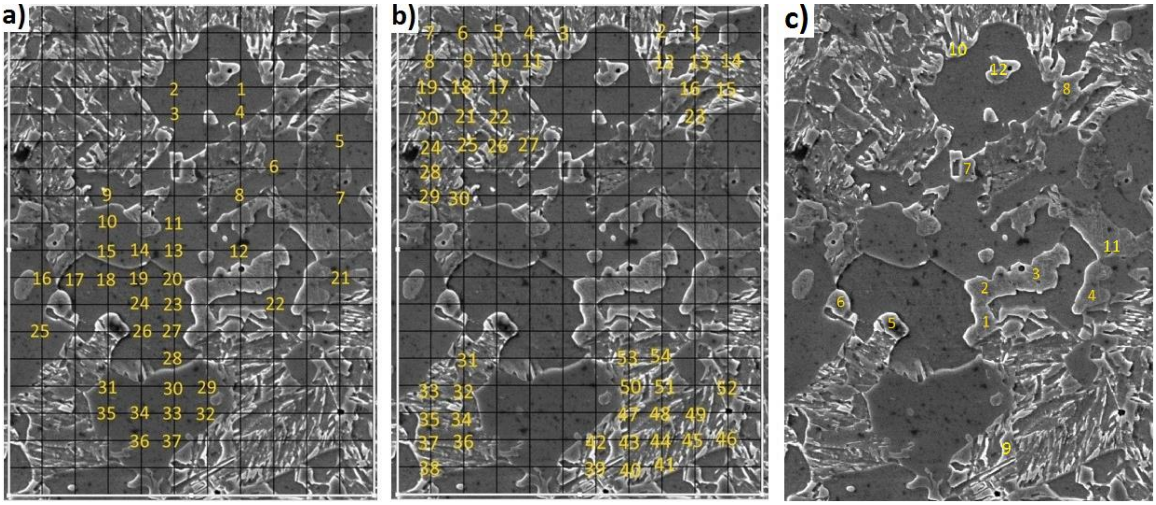

Figure 4-31 Randomly selected points in a) ferrite, b) martensite and c)blocky retained austenite used to calculated the average local strain in each phase in each deformation stage.

Figure 4-32 compares total true strain obtained in each deformation stage using point analysis and phase fraction of each phase with the total true strain obtained from the

whole strain map. The difference of two graphs values remains under 5% which confirms the representability of the data points.

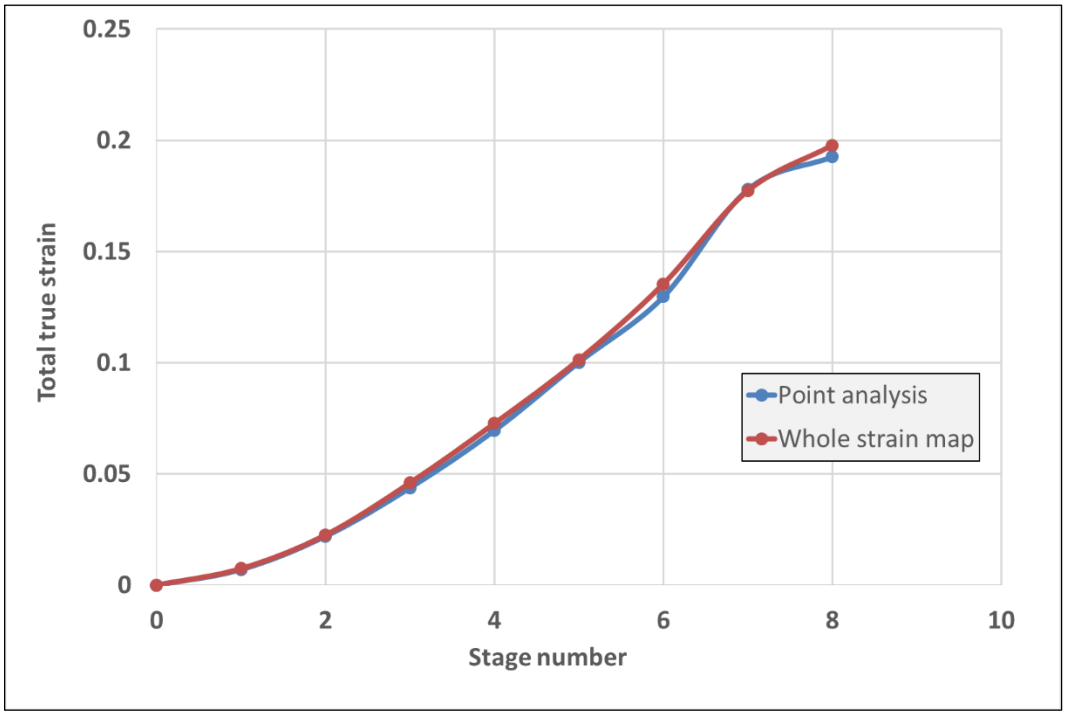

Figure 4-32 Comparison between total true strain obtained from point analysis and whole strain map.

Figure 4-33 compares the average local true strain values in ferrite, martensite and blocky retained austenite in third strain map with average true strain values of previous maps in the range of total strain less than 0.2.

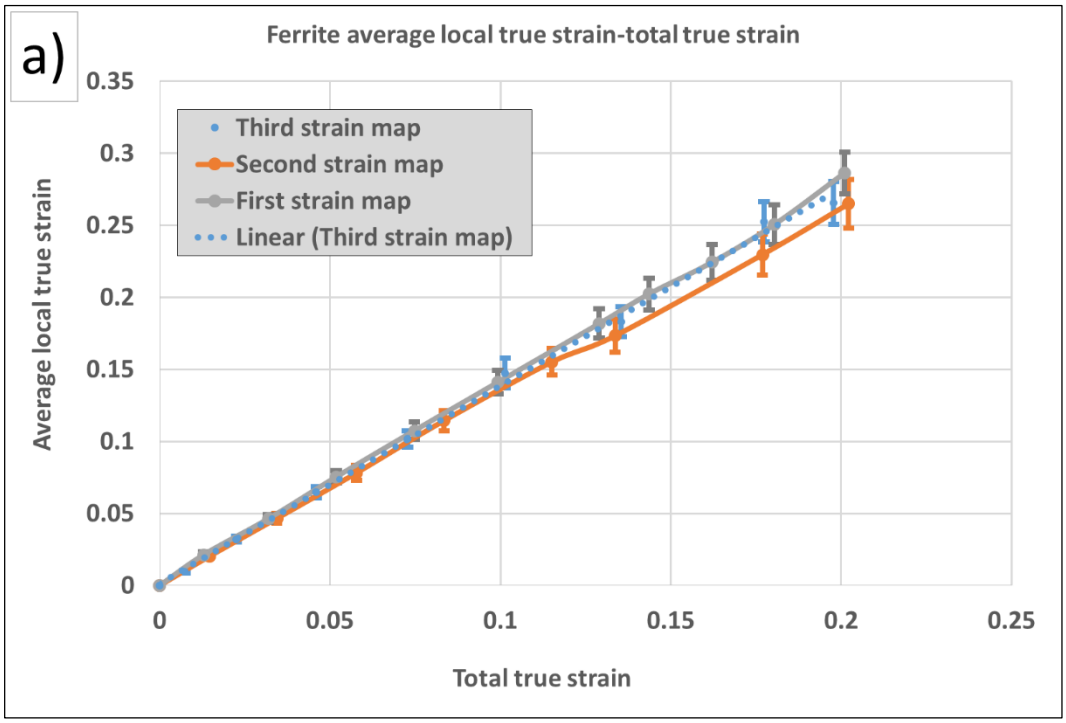
a)
Ferrite average local true strain-total true strain
Third strain map
Second strain map
First strain map
Linear (Third strain map)
Average local true strain
Total true strain
0.35
0.3
0.25
0.2
0.15
0.1
0.05
0
0
0.05
0.1
0.15
0.2
0.25

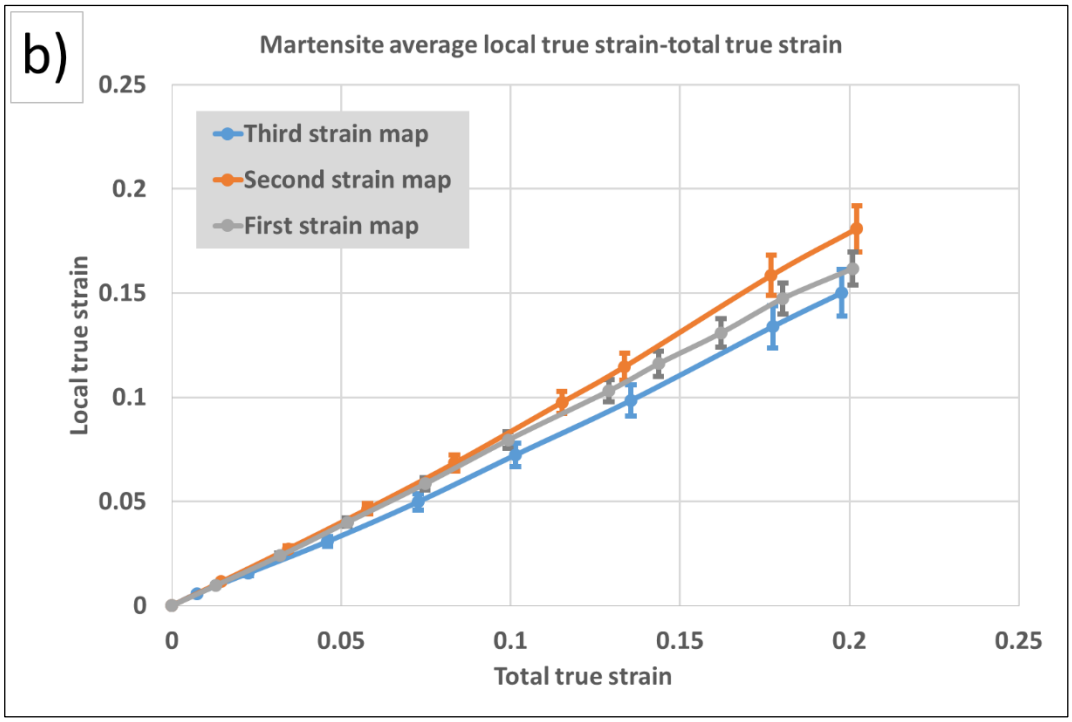
b)
Martensite average local true strain-total true strain
Third strain map
Second strain map
First strain map
Local true strain
Total true strain
0.25
0.2
0.15
0.1
0.05
0
0
0.05
0.1
0.15
0.2
0.25

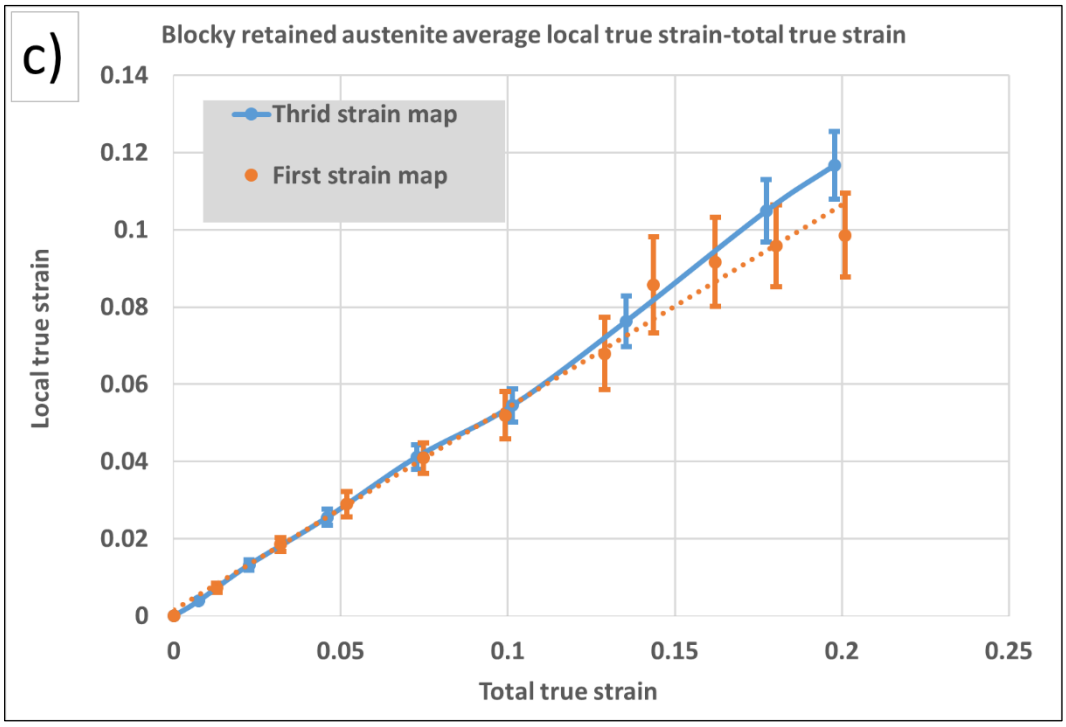

Figure 4-33 Comparison between average local true strain measure in a) ferrite, b) martensite and c) blocky retained austenite at different strain maps until true strain of 0.2.

Ferrite phase showed similar average local true strain value in first and third strain map however it showed a lower average local strain value at second strain map where the volume fraction of martensite was higher as discussed before. Martensite showed the lowest average local true strain at third strain map which contained 7.8 % less martensite than the second strain map. The difference between average local true strain in martensite in second and third strain map reached to 0.03 at total true strain of 0.2. Blocky retained austenite showed similar average local true strain value until total true strain of 0.1 in first and third strain map. The average local true strain in Blocky retained austenite in first strain map

started to deviate from its value in third strain map with can be related to the magnification of deformation images that affected the quality of strain map.

Figure 4-34 shows the evolution of the average local true strain ratio of ferrite to martensite, ferrite to blocky retained austenite and martensite to blocky retained austenite.

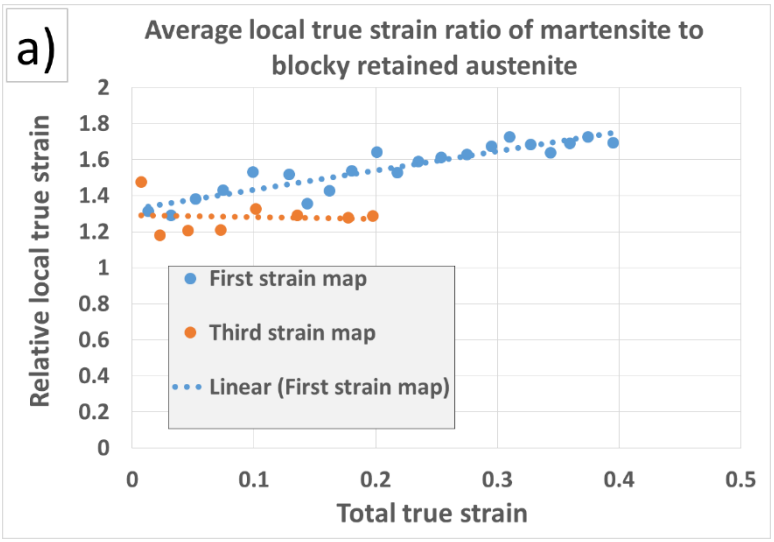

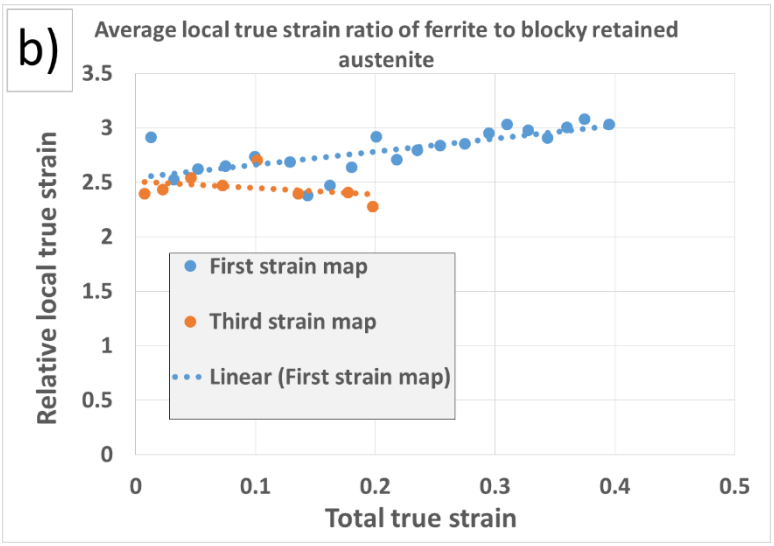

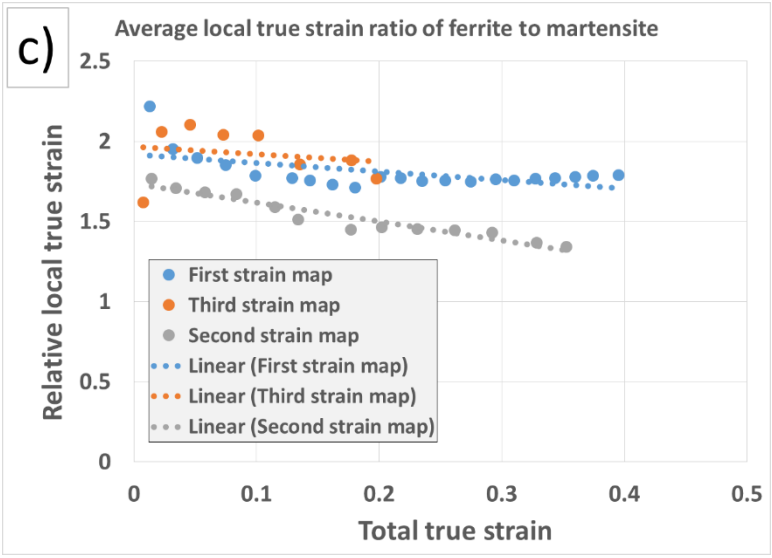

Figure 4-34 A comparison between average local true strain ratio of a) martensite to blocky retained austenite, b) ferrite to blocky retained austenite and c) ferrite to martensite for the different obtained strain maps.

According to Figure 4-34 a and b, the ratio of the ferrite and martensite deformation to blocky retained austenite deformation starts to increase in the first strain map at total strains higher than 0.2 or post uniform deformation which can imply the lower deformation ability of retained austenite blocks due their transformation to martensite at total strain higher than 0.2. The deformation ratio of ferrite and martensite to blocky retained austenite at third strain map are approximately constant. As shown in Figure 4-34 c, the ratio of deformation of ferrite to martensite decreases in all of the strain maps which indicates the tendency of martensite to deform at higher total strains when the stress concentration in martensite started to decrease as the result of deformation. This tendency is more pronounced at higher volume fraction of martensite in second strain map.

Figure 4-35 shows the average of local true strain ratios of different constituent phases obtained from all deformation stages. Ferrite to retained austenite strain is highest with a ratio of 2.7 while martensite to retained austenite has the lowest ratio of 1.5.

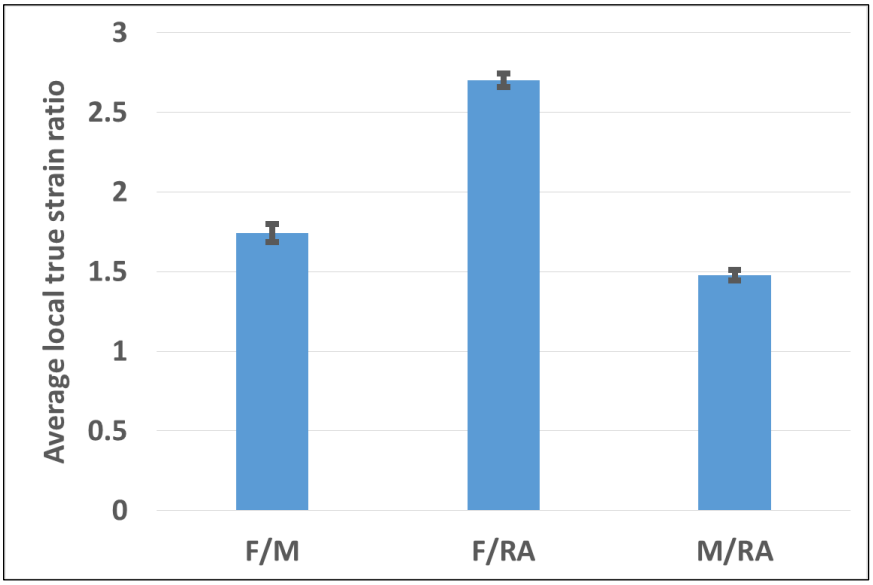

Figure 4-35 Average of local true strain ratios of the constituent phase obtained from whole deformation stages. F/M, F/RA and M/RA denote ferrite to martensite, Ferrite to blocky retained austenite and martensite to blocky retained austenite ratios.

In summary, micro-DIC analysis of QP980 steel SEM deformation micrographs revealed that martensite undergoes significant deformation such that there are regions in the strain maps that show the same local true strains in ferrite and martensite. Micromechanical behavior of the ferrite and martensite phases is found to depend on volume fraction of each phase such that locations with higher volume fraction of martensite show higher ratio of ferrite to martensite local true strains. Strain localization occurred mostly at regions where ferrite grains were confined within retained austenite blocks and

martensitic regions. Martensite was more involved in strain accommodation at total true strains higher than 0.1 as the ratio of average local true strain of ferrite to martensite started to decrease beyond this point. This is more pronounced in strain maps obtained from the region with a higher martensite volume fraction. Ratios of ferrite and martensite average local true strain to that of retained austenite start to decrease after local true strain of 0.2 which indicates the influence of TRIP effect on deformation ability or work-hardening of retained austenite blocks. As expected ferrite shows the highest local true strains while retained austenite blocks has the lowest. The ratio of average local true strain of ferrite to martensite and martensite to ferrite obtained from all strain maps were calculated to be 2.7 and 1.5 respectively.

4.7 Nano-hardness:

Nano-hardness measurements were performed to correlate the amount of plastic deformation in constituent phases to their strength. Figure 4-36 shows optical micrograph of grid indentation performed on the QP980 sample.

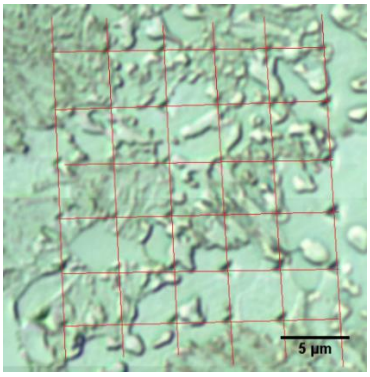

Figure 4-36 Optical micrograph showing nano-indents in the array of 6×6 performed on QP980 steel sample.

Only indents which are located fully inside a given phase are selected for measurements. 21 points out of 36 indents were therefore taken into account for nano-hardness measurement. Unfortunately, there was no point located inside blocky retained austenite. Therefore, single point analysis was conducted on the sample for which 3 out of the 17 points are located inside the blocky retained austenite. 6 points out of the 17 points which are located inside the ferrite and martensite instead of retained austenite blocks were selected for calculating the average nano-hardness value in ferrite and martensite. The low yield of the single point analysis can be related to the small size of the retained austenite blocks and the low accuracy of the nano-indentation device. The retained austenite blocks were not large enough to accommodate the nano-indents and the device did not have the accuracy to perform the indents inside the retained austenite blocks. Figure 4-37 shows retained austenite blocks in which nano-hardness measurement were successfully conducted using the single indent measurement method.

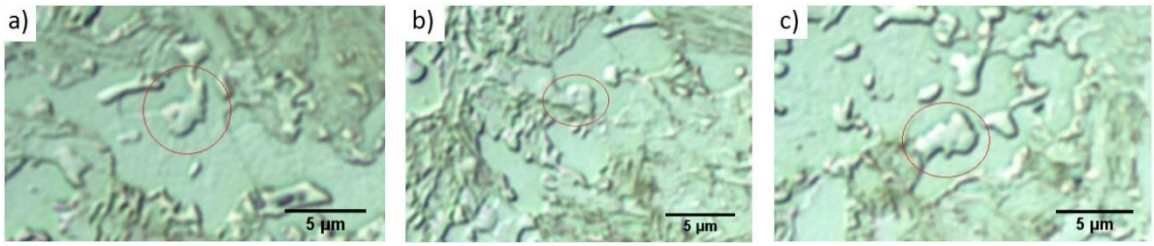

Figure 4-37 Optical images shows three retained austenite blocks which the nano-hardness measurement successfully implemented on them. The retained austenite blocks which measurement conducted are shown with red circle.

Figure 4-38 shows nano-hardness values of the constituent phases in QP980 steel. Retained austenite nano-hardness values are significantly higher than in ferrite and martensite. Ferrite has the lowest nano-hardness values.

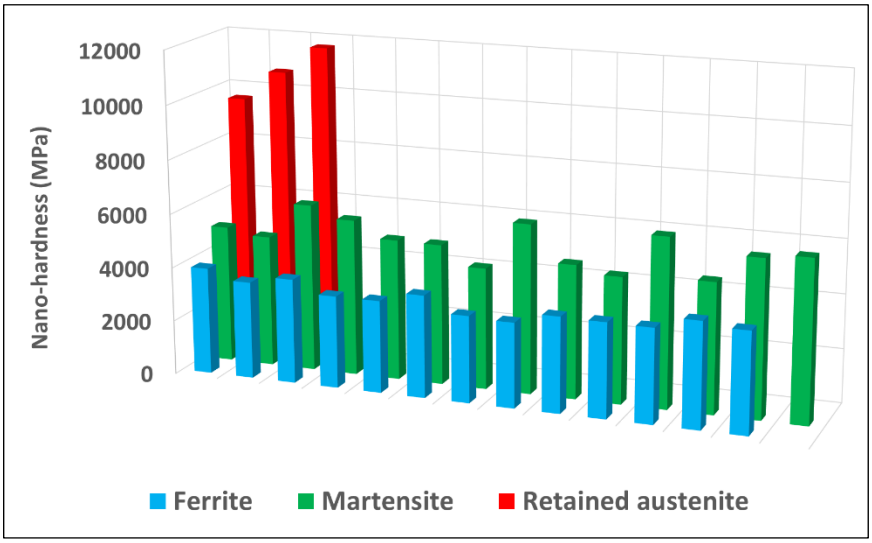

Figure 4-38 Nano-hardness values in ferrite, martensite and retained austenite blocks.

The average nano-hardness for each phase is shown in Figure 4-39. The nano-hardness value in retained austenite is three times greater than ferrite and two times greater than martensite. These results are in a good agreement with micro DIC measurement that local true strain in ferrite is 1.7 times greater than in martensite and 2.7 times greater than that in retained austenite. The higher nano-hardness value in retained austenite can be attributed to its significantly higher carbon content than martensite carbon content as discussed earlier. The higher standard error in blocky retained austenite average nano-hardness value compared to other phases is due the lower number of measurements performed on it.

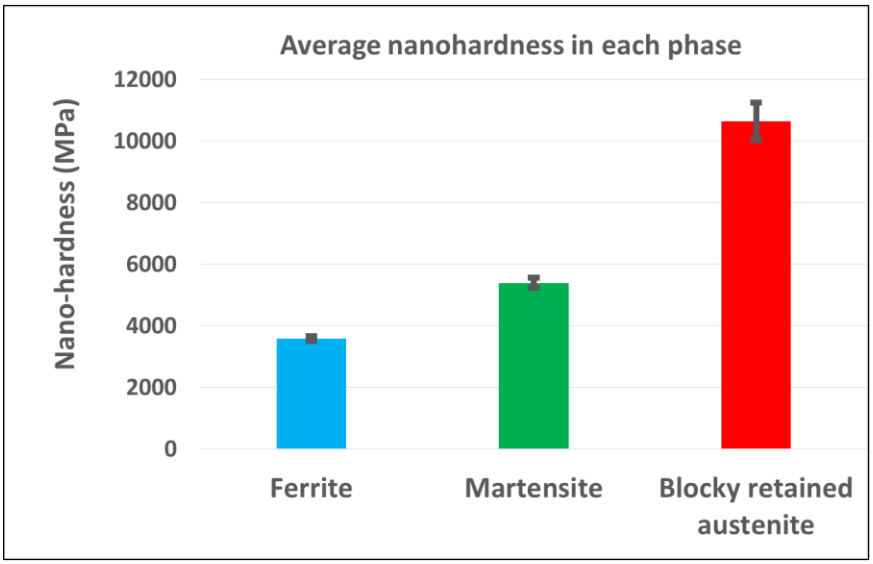

Figure 4-39 Average nano-hardness value ferrite, martensite and blocky retained austenite.

4.8 Comparison the outcome of this research with related studies in literature

Carbon content of martensite in QP980 steel was measured to be 0.037 wt. % using APT (82). The low carbon content of martensite can be related to the effect of both carbon partitioning from martensite to austenite and undesirable carbide precipitation as a result of tempering in some martensite regions. Mazinani et al. (21) reported that a DP steel subjected to quench and tempering heat treatment showed higher fracture strain and considerably lower amount of voids after fracture compared to the quenched condition with the same amount of martensite volume fraction according to the optical micrograph obtained from fractured samples. They reported that banded martensite with carbon

concentration lower than 0.1% showed little or no strain partitioning between martensite and ferrite while banded martensite with martensite carbon concentration greater than 0.33% remained almost elastic in strain levels lower than 15%. Although the carbon content in martensite region in the QP980 studied here was measured to be less than 0.1%, the average ferrite to martensite local true strain ratio calculated from three different strain maps obtained from different samples was 1.7 which can be related to existence of fine film-like and blocky retained austenite that transformed during deformation in martensitic regions.

Results obtained from ex-situ tensile tests coupled with EBSD presented in section 4.4.2 show that some of the retained austenite blocks which are located at the interfaces of ferrite and martensite were completely transformed to martensite at a total true strain of 0.07, i.e. during uniform deformation, while most of the retained austenite blocks located inside martensite regions remained untransformed. According to XRD measurement results obtained from interrupted tensile tests, at the point of necking and after failure, 57% and 93% of retained austenite transformed to martensite respectively. This result implies that retained austenite particles located inside the martensite regions transformed later than retained austenite blocks located in ferrite regions and at interfaces that experienced high local strains. In other words, retained austenite blocks located at ferrite grains or martensite-ferrite interfaces show lower mechanical stability compared to retained austenite blocks at martensite regions. The influence of surrounding microstructure on mechanical stability of retained austenite was also studied by other researchers. For example, Hidalgo et al. (83)

investigated the effect of surrounding microstructure on the mechanical stability of retained austenite in Q&P steels. In that study, retained austenite volume fraction in three Q&P steels subjected to different heat treatments was measured using XRD after interrupted tensile tests. First specimen was fully austenitized, quenched to 220 °C and partitioned at 400 °C for 50 s and labeled as QP. Second specimen was subjected to tempering heat treatment at 450 °C for 1800 s after the same Q&P heat treatment and labeled as QP450 and third specimen was tempered at 700 ° C for 5 s after the same Q&P heat treatment and labeled as QP700. Among the three specimens, QP with the hardest martensite phase showed highest mechanical stability of retained austenite and QP700 with the softest martensite showed the lowest mechanical stability. They attributed this phenomenon to higher yield strength of martensite in the specimen with QP heat treatment condition which resisted the volume expansion associated with TRIP effect and also the hydrostatic pressure within the retained austenite as the results of volume expansion during martensite formation which suppressed the TRIP in retained austenite that required volume expansion in QP specimen.

It should be noted that research on Q&P and TRIP steels showed that carbon content, volume fraction and orientation of retained austenite grains also have influence on mechanical stability of retained austenite phase. In addition, film-like retained austenite tends to have higher mechanical stability compared to blocky retained austenite (49, 50).

Studies regarding the cause of strain heterogeneity in DP steels reveal that surrounding microstructure of ferrite grains has the most influence on the determination of

strain localization regions in DP steels rather than grain orientations (24, 84). According to strain maps obtained from this study (Figure 4-17, Figure 4-24 and Figure 4-30), most of the strain localization in QP980 steel occurred in locations where ferrite was confined within martensite regions or retained austenite blocks which shows lower deformation ability compared to ferrite. This result is in good agreement with the same experiments conducted on DP steels. Kapp et al. (73) investigated micromechanical behavior of DP1000 using in-situ tensile tests under SEM coupled with macro-DIC analysis. They concluded that strain localization in DP1000 microstructure occurred in ferrite channels and bays subjected to martensite constraint and located normal to the loading direction. Kang et al. (22) reported that strain localization in ferrite in DP600 steel occurs when the ferrite size is three times greater than the surrounding martensite thickness.

Microstructural damage in QP980 steel in the forms of cracks starts to occur inside both ferrite and martensite at approximately same total true strains; however, damage growth is faster in martensite leading to formation of large cavities which are more pronounced at regions containing higher volume fraction of martensite. By way of contrast, cracks formed inside ferrite remain narrow. Most of the cracks formed were aligned at approximately 45 degrees with respect to loading axis which can be attributed to strain localization due to the shear band formation. Microstructural damage in the form of small voids also observed inside ferrite grains; however, no ferrite-martensite and ferrite-blocky retained austenite interface decohesion was observed in this study. Tasan et al. (20) reported that in DP steels martensite cracking occurs in microstructures with martensite

volume fraction higher than 60% and ferrite grain size less than 10 µm in which the martensite phase appears as a fully connected networks that facilitates its early plasticity during loading. However, ferrite-martensite interface decohesion is the dominant damage mechanism in the DP steels when the martensite volume fraction is approximately between 35-65 % and ferrite grain sizes approximately between 20-75 µm. Both mechanisms are observed in microstructures with ferrite grain size smaller than 20µm and martensite volume fraction less than 45%. Although the difference between carbon content and microstructure nature of martensite regions in QP980 steel should be considered when comparing damage mechanisms in QP980 steel with DP steels, QP980 steel with martensite average volume fraction of 58.5%, fully connected martensite network and ferrite grain size between 5-20 µm possess the microstructure parameters close to values reported for martensite cracking damage mechanism which is dominant as the damage mechanism in QP980 steel.

As mentioned earlier among the retained austenite blocks located inside ferrite grains, the larger and angular ones showed evidence of brittle cracking that starts to occur during uniform deformation or early stage of necking. Tasan et al. (54) investigated the influence of martensite distribution on damage mechanisms in DP800 steel using SEM based in-situ tensile testing experiments coupled with macro-DIC analysis. They reported that regions with lower volume fraction, blocky and heterogeneously distributed martensite accommodates more stress compared to regions with higher volume fraction and well-dispersed distribution of martensite. Stress concentration in heterogeneously distributed

martensite blocks leads to microscopic strain localization at a few ferritic grains neighboring the blocky martensite phase before full work-hardening capacity of the material is achieved. This causes failure at lower loads compared to microstructures with uniform and finer dispersion of martensite which allows more ferrite grains to contribute to strain accommodation by developing fine strain bands. As shown in Figure 4-30 a, stress localization in large and blocky retained austenite located in the region 1 led to strain localization in the adjacent ferrite grain and damage propagation in the form of small voids produced as the results of the brittle cracking of a large blocky retained austenite into 5 small parts (Figure 4-14 e). As previously mentioned although brittle cracking and damage propagation in the large blocky retained austenite was attributed to TRIP effect, no evidence of small retained austenite cracking was found during SEM in-situ tensile testing investigations in this research.

Although blocky retained austenite showed the lowest deformation ability between the other constituent phases it was found to have the highest nano-hardness compared to the other phases. Furnémont et al. (85) measured nano-hardness values in TRIP-assisted multiphase steel with chemical composition of Fe-0.2C-3Mn-1.6Si. The measured nano-hardness values for martensite, retained austenite blocks, bainite and ferrite were 16.7±1.9 GPa, 10.0±1.1 GPa, 7.0±0.8 GPa and 4.8±0.2 GPa respectively. They attributed the high nano-harness value of retained austenite to its higher carbon content which is common for TRIP-assisted multiphase steels. Although the value reported for retained austenite nano-hardeness is in the good agreement with the value reported here, the martensite nano-

hardness in that steel is more than double that measured here which can be attributed to the lower carbon content of martensite in QP980 steel due to the effect of carbon partitioning and carbide precipitation. Matsuda et al. (86) compared the nano-hardness value on a so-called auto-tempered ultra-high strength steel sheet (chemical composition of Fe-0.21C-1.5Si-2.3Mn and additional 1% Cr) with the nano-hardness values obtained from a reference steel which was fully quenched and tempered. Auto-tempering heat treatment refers to a process in which the first formed martensite is subjected to tempering heat treatment during the quenching or cooling step. The heat treat process included heating at 880 °C for 180 s, subsequently cooling to 473 °C with cooling rate of 40 °C /s and holding it at 473 °C for 90 s and finally cooling to room temperature with cooling rate of 15 °C /s. The majority of the nano-hardness values for both steels lay between 5.5-6.5 GPa which is close to the average value reported for martensite phase nano-hardness in our QP980 steel. However, the distribution of values for auto-tempered steel sheet was larger and included higher percentage of values lay between 6.5-7.5 GPa which was attributed to existence of less tempered martensite in the microstructure of auto-tempered steel.

5 Conclusions:

In this research, micro-strain partitioning was investigated to determine the micromechanisms of damage in a commercial QP980 steel sheet. The experimental approach involved in-situ tensile tests coupled with SEM followed by quantification of microstructural deformation using the micro-DIC method. TRIP was investigated using ex-situ tensile tests coupled with XRD and EBSD to understand its influence on microstructural deformation and damage. Nano-hardness was measured in each phase to correlate the level of plastic deformation with the strength of the phases. The following conclusions can be drawn from this study:

- According to the micro-DIC results, the average local true strain in ferrite is 2.7 and 1.7 times greater than that in martensite and blocky retained austenite, respectively which is in a good agreement with nano-hardness results that the strength of blocky retained austenite is three and two times greater than that in ferrite and martensite respectively. The high nano-hardness and low local true strain of blocky retained austenite can be related to its high carbon content compared to ferrite and martensite.

- According to micro-DIC results, average local true strain ratio of ferrite and martensite to blocky retained austenite started to increase after a total true strain of 0.2 or during the post uniform deformation region which indicates lower deformation ability of retained austenite blocks due to their transformation to martensite.

- The deformation ratio of ferrite to martensite decreases as the total strain increases which indicates the deformation tendency of martensite at higher total strain level when stress concentration in martensite started to decrease as the result of deformation. This phenomenon was more pronounced at regions contained higher volume fraction of martensite.

- The significant amount of deformation in martensite can be attributed to two important factors namely:
    - Relatively low carbon content of martensite due to the partitioning and tempering process, and
    - The TRIP phenomenon that happens in both film-like retained austenite between martensite laths and blocky retained austenite at martensite regions that leads to increasing the work-hardening of the martensite phase and QP980 steel in general.

- In-situ tensile test micrographs show evidences of large and angular retained austenite blocks cracking in regions experiencing strain localization. This commences during the uniform deformation stage or shortly after necking commences. This is likely triggered by their early transformation to martensite.

- According to XRD and EBSD results, the retained austenite volume fraction is reduced by 29% after a total true strain of 0.07. EBSD results confirm that some of the retained austenite blocks were almost fully transformed to martensite at a local

true strain of 0.07. XRD results show that the retained austenite fraction transformed to martensite at uniform and post-uniform deformation region were 57% and 34% respectively while 7% of retained austenite remained untransformed.

- According to micro-strain, EBSD maps and XRD results, the QP980 steel owes its high formability primarily to co-deformation of martensite and ferrite and secondarily to the TRIP effect.
- Damage in both ferrite and martensite occurs at approximately the same global strain; however, damage growth in martensite leads to larger cavities due to its higher rate than in ferrite. Despite earlier cracking of blocky retained austenite in some regions, this appears to have little impact on the final failure process.
- Ductile fracture and shear fracture are the dominant types of fracture in QP980 and there is no evidence of quasi-cleavage or cleavage failure.

6 References

1. De Moor E, Lacroix S, Clarke A, Penning J, Speer J. Effect of retained austenite stabilized via quench and partitioning on the strain hardening of martensitic steels. Metallurgical and Materials Transactions A. 2008;39(11):2586.
2. Santofimia M, Speer J, Clarke A, Zhao L, Sietsma J. Influence of interface mobility on the evolution of austenite–martensite grain assemblies during annealing. Acta Materialia. 2009;57(15):4548-57.
3. Li H, Lu X, Li W, Jin X. Microstructure and mechanical properties of an ultrahigh-strength 40SiMnNiCr steel during the one-step quenching and partitioning process. Metallurgical and Materials Transactions A. 2010;41(5):1284-300.
4. Avramovic-Cingara G, Ososkov Y, Jain M, Wilkinson D. Effect of martensite distribution on damage behaviour in DP600 dual phase steels. Materials Science and Engineering: A. 2009;516(1-2):7-16.
5. Lai Q, Bouaziz O, Gouné M, Brassart L, Verdier M, Parry G, et al. Damage and fracture of dual-phase steels: Influence of martensite volume fraction. Materials Science and Engineering: A. 2015;646:322-31.
6. Lai Q, Bouaziz O, Gouné M, Perlade A, Bréchet Y, Pardoen T. Microstructure refinement of dual-phase steels with 3.5 wt% Mn: Influence on plastic and fracture behavior. Materials Science and Engineering: A. 2015;638:78-89.
7. Sun J, Yu H. Microstructure development and mechanical properties of quenching and partitioning (Q&P) steel and an incorporation of hot-dipping galvanization during Q&P process. Materials Science and Engineering: A. 2013;586:100-7.
8. Nayak S, Anumolu R, Misra R, Kim K, Lee D. Microstructure–hardness relationship in quenched and partitioned medium-carbon and high-carbon steels containing silicon. Materials Science and Engineering: A. 2008;498(1-2):442-56.
9. Speer JG, De Moor E, Findley K, Matlock D, De Cooman B, Edmonds D. Analysis of microstructure evolution in quenching and partitioning automotive sheet steel. Metallurgical and Materials Transactions A. 2011;42(12):3591.
10. Zhao J, Jiang Z. Thermomechanical processing of advanced high strength steels. Progress in Materials Science. 2018.
11. Sun J, Yu H, Wang S, Fan Y. Study of microstructural evolution, microstructure-mechanical properties correlation and collaborative deformation-transformation behavior of quenching and partitioning (Q&P) steel. Materials Science and Engineering: A. 2014;596:89-97.

12. Bagliani EP, Santofimia M, Zhao L, Sietsma J, Anelli E. Microstructure, tensile and toughness properties after quenching and partitioning treatments of a medium-carbon steel. Materials Science and Engineering: A. 2013;559:486-95.

13. Wang L, Speer JG. Quenching and partitioning steel heat treatment. Metallography, Microstructure, and Analysis. 2013;2(4):268-81.

14. Santofimia M, Nguyen-Minh T, Zhao L, Petrov R, Sabirov I, Sietsma J. New low carbon Q&P steels containing film-like intercritical ferrite. Materials Science and Engineering: A. 2010;527(23):6429-39.

15. De Cooman BC, Speer JG. Quench and Partitioning Steel: A New AHSS Concept for Automotive Anti-Intrusion Applications. steel research international. 2006;77(9-10):634-40.

16. Takahama Y, Santofimia M, Mecozzi M, Zhao L, Sietsma J. Phase field simulation of the carbon redistribution during the quenching and partitioning process in a low-carbon steel. Acta Materialia. 2012;60(6-7):2916-26.

17. Edmonds D, He K, Rizzo F, De Cooman B, Matlock D, Speer J. Quenching and partitioning martensite—A novel steel heat treatment. Materials Science and Engineering: A. 2006;438:25-34.

18. Santofimia M, Zhao L, Petrov R, Kwakernaak C, Sloof W, Sietsma J. Microstructural development during the quenching and partitioning process in a newly designed low-carbon steel. Acta Materialia. 2011;59(15):6059-68.

19. Salehiyan D, Samei J, Wilkinson DS, editors. In-situ Characterization of Microstructural Damage in QP980 Steel. TMS Annual Meeting & Exhibition; 2018: Springer.

20. Tasan CC, Diehl M, Yan D, Bechtold M, Roters F, Schemmann L, et al. An overview of dual-phase steels: advances in microstructure-oriented processing and micromechanically guided design. Annual Review of Materials Research. 2015;45:391-431.

21. Mazinani M, Poole W. Effect of martensite plasticity on the deformation behavior of a low-carbon dual-phase steel. Metallurgical and materials transactions A. 2007;38(2):328-39.

22. Kang J, Ososkov Y, Embury JD, Wilkinson DS. Digital image correlation studies for microscopic strain distribution and damage in dual phase steels. Scripta Materialia. 2007;56(11):999-1002.

23. Joo S-H, Lee JK, Koo J-M, Lee S, Suh D-W, Kim HS. Method for measuring nanoscale local strain in a dual phase steel using digital image correlation with nanodot patterns. Scripta Materialia. 2013;68(5):245-8.

24. Han Q, Kang Y, Hodgson PD, Stanford N. Quantitative measurement of strain partitioning and slip systems in a dual-phase steel. Scripta Materialia. 2013;69(1):13-6.

25. Ghassemi-Armaki H, Maaß R, Bhat S, Sriram S, Greer J, Kumar K. Deformation response of ferrite and martensite in a dual-phase steel. Acta Materialia. 2014;62:197-211.

26. Avramovic-Cingara G, Saleh CA, Jain M, Wilkinson D. Void nucleation and growth in dual-phase steel 600 during uniaxial tensile testing. Metallurgical and materials transactions A. 2009;40(13):3117.

27. Wang C, Shi J, Cao W, Dong H. Characterization of microstructure obtained by quenching and partitioning process in low alloy martensitic steel. Materials Science and Engineering: A. 2010;527(15):3442-9.

28. Santofimia M, Zhao L, Sietsma J. Model for the interaction between interface migration and carbon diffusion during annealing of martensite–austenite microstructures in steels. Scripta Materialia. 2008;59(2):159-62.

29. Santofimia M, Zhao L, Sietsma J. Microstructural evolution of a low-carbon steel during application of quenching and partitioning heat treatments after partial austenitization. Metallurgical and Materials Transactions A. 2009;40(1):46.

30. Toji Y, Miyamoto G, Raabe D. Carbon partitioning during quenching and partitioning heat treatment accompanied by carbide precipitation. Acta Materialia. 2015;86:137-47.

31. Speer J, Matlock D, De Cooman B, Schroth J. Carbon partitioning into austenite after martensite transformation. Acta materialia. 2003;51(9):2611-22.

32. Koistinen D. A general equation prescribing the extent of the austenite-martensite transformation in pure iron-carbon alloys and plain carbon steels. acta metallurgica. 1959;7:59-60.

33. Mahieu J, De Cooman B, Maki J. Phase transformation and mechanical properties of Si-free CMnAl transformation-induced plasticity-aided steel. Metallurgical and Materials Transactions A. 2002;33(8):2573-80.

34. Mahieu J, De Cooman B, Claessens S. Galvanizability of high-strength steels for automotive applications. metallurgical and materials transactions A. 2001;32(11):2905-8.

35. Santofimia M, Zhao L, Petrov R, Sietsma J. Characterization of the microstructure obtained by the quenching and partitioning process in a low-carbon steel. Materials Characterization. 2008;59(12):1758-64.

36. Pierce DT, Coughlin D, Clarke KD, De Moor E, Poplawsky J, Williamson DL, et al. Microstructural evolution during quenching and partitioning of 0.2 C-1.5 Mn-1.3 Si steels with Cr or Ni additions. Acta Materialia. 2018;151:454-69.

37. De Moor E, Speer JG, Matlock DK, Kwak JH, Lee SB. Quenching and partitioning of CMnSi steels containing elevated manganese levels. steel research international. 2012;83(4):322-7.

38. De Moor E, Speer JG, Matlock DK, Kwak J-H, Lee S-B. Effect of carbon and manganese on the quenching and partitioning response of CMnSi steels. ISIJ international. 2011;51(1):137-44.

39. Edmonds D, He K, Miller MK, Rizzo F, Clarke A, Matlock DK, et al., editors. Microstructural features of'quenching and partitioning': a new martensitic steel heat treatment. Materials science forum; 2007: Trans Tech Publ.

40. Liu H, Jin X, Dong H, Shi J. Martensitic microstructural transformations from the hot stamping, quenching and partitioning process. Materials characterization. 2011;62(2):223-7.

41. Maheswari N, Chowdhury SG, Kumar KH, Sankaran S. Influence of alloying elements on the microstructure evolution and mechanical properties in quenched and partitioned steels. Materials Science and Engineering: A. 2014;600:12-20.

42. Kozeschnik E, Bhadeshia H. Influence of silicon on cementite precipitation in steels. Materials Science and Technology. 2008;24(3):343-7.

43. Zhong N, Wang X, Wang L, Rong Y. Enhancement of the mechanical properties of a Nb-microalloyed advanced high-strength steel treated by quenching–partitioning–tempering process. Materials Science and Engineering: A. 2009;506(1-2):111-6.

44. Zhang J, Ding H, Misra R, Wang C. Enhanced stability of retained austenite and consequent work hardening rate through pre-quenching prior to quenching and partitioning in a Q–P microalloyed steel. Materials Science and Engineering: A. 2014;611:252-6.

45. Clarke A, Speer J, Miller M, Hackenberg R, Edmonds D, Matlock D, et al. Carbon partitioning to austenite from martensite or bainite during the quench and partition (Q&P) process: A critical assessment. Acta materialia. 2008;56(1):16-22.

46. Li H, Lu X, Wu X, Min Y, Jin X. Bainitic transformation during the two-step quenching and partitioning process in a medium carbon steel containing silicon. Materials Science and Engineering: A. 2010;527(23):6255-9.

47. Kokosza A, Pacyna J. Mechanical stability of retained austenite in unalloyed structural steels of various carbon content. 2010.

48. Ryu JH, Kim D-I, Kim HS, Bhadeshia H, Suh D-W. Strain partitioning and mechanical stability of retained austenite. Scripta Materialia. 2010;63(3):297-9.

49. Blondé R, Jimenez-Melero E, Zhao L, Wright J, Brück E, Van der Zwaag S, et al. Mechanical stability of individual austenite grains in TRIP steel studied by synchrotron X-ray diffraction during tensile loading. Materials Science and Engineering: A. 2014;618:280-7.

50. Xiong X, Chen B, Huang M, Wang J, Wang L. The effect of morphology on the stability of retained austenite in a quenched and partitioned steel. Scripta Materialia. 2013;68(5):321-4.

51. Jacques P, Delannay F, Ladrière J. On the influence of interactions between phases on the mechanical stability of retained austenite in transformation-induced plasticity multiphase steels. Metallurgical and Materials Transactions A. 2001;32(11):2759-68.

52. de Diego-Calderón I, De Knijf D, Monclús M, Molina-Aldareguia J, Sabirov I, Föjer C, et al. Global and local deformation behavior and mechanical properties of individual phases in a quenched and partitioned steel. Materials Science and Engineering: A. 2015;630:27-35.

53. Sun X, Choi KS, Soulami A, Liu WN, Khaleel MA. On key factors influencing ductile fractures of dual phase (DP) steels. Materials Science and Engineering: A. 2009;526(1-2):140-9.

54. Tasan CC, Hoefnagels JP, Diehl M, Yan D, Roters F, Raabe D. Strain localization and damage in dual phase steels investigated by coupled in-situ deformation experiments and crystal plasticity simulations. International Journal of Plasticity. 2014;63:198-210.

55. Kadkhodapour J, Butz A, Rad SZ. Mechanisms of void formation during tensile testing in a commercial, dual-phase steel. Acta Materialia. 2011;59(7):2575-88.

56. Ghadbeigi H, Pinna C, Celotto S, Yates J. Local plastic strain evolution in a high strength dual-phase steel. Materials Science and Engineering: A. 2010;527(18-19):5026-32.

57. Tasan C, Hoefnagels J, Geers M. Microstructural banding effects clarified through micrographic digital image correlation. Scripta Materialia. 2010;62(11):835-8.

58. Zhou L, Samei J, Kang J, Wilkinson DS. Influence of Vanadium on Microstrain Partitioning and Evolution of Microstructural Damage in DP1300 Steel. Manuscript submitted for publication. 2018.

59. Samei J, Zhou L, Kang J, Wilkinson DS. Microstructural analysis of ductility and fracture in fine-grained and ultrafine-grained vanadium-added DP1300 steels. International Journal of Plasticity. 2018.

60. Pan B, Qian K, Xie H, Asundi A. Two-dimensional digital image correlation for in-plane displacement and strain measurement: a review. Measurement science and technology. 2009;20(6):062001.

61. Techniques GOM. Aramis v6. 1 user manual. GOM mbH. 2007.

62. Lu H, Cary P. Deformation measurements by digital image correlation: implementation of a second-order displacement gradient. Experimental mechanics. 2000;40(4):393-400.

63. Carroll JD, Abuzaid W, Lambros J, Sehitoglu H. High resolution digital image correlation measurements of strain accumulation in fatigue crack growth. International Journal of Fatigue. 2013;57:140-50.

64. Sabate N, Vogel D, Gollhardt A, Keller J, Cane C, Gracia I, et al. Residual stress measurement on a MEMS structure with high-spatial resolution. Journal of microelectromechanical systems. 2007;16(2):365-72.

65. Sun Y, Pang JH, Fan W. Nanoscale deformation measurement of microscale interconnection assemblies by a digital image correlation technique. Nanotechnology. 2007;18(39):395504.

66. Chang S, Wang C, Xiong C, Fang J. Nanoscale in-plane displacement evaluation by AFM scanning and digital image correlation processing. Nanotechnology. 2005;16(4):344.

67. Garnaes J, Nielsen L, Dirscherl K, Jørgensen J, Rasmussen J, Lindelof P, et al. Two-dimensional nanometer-scale calibration based on one-dimensional gratings. Applied Physics A. 1998;66(1):S831-S5.

68. Dirscherl K, Garnæs J, Nielsen L, Jøgensen JF, Sørensen MP. Modeling the hysteresis of a scanning probe microscope. Journal of Vacuum Science & Technology B: Microelectronics and Nanometer Structures Processing, Measurement, and Phenomena. 2000;18(2):621-5.

69. Sun Y, Pang JH. AFM image reconstruction for deformation measurements by digital image correlation. Nanotechnology. 2006;17(4):933.

70. Berfield TA, Patel JK, Shimmin RG, Braun PV, Lambros J, Sottos NR. Fluorescent image correlation for nanoscale deformation measurements. Small. 2006;2(5):631-5.

71. Franck C, Hong S, Maskarinec S, Tirrell D, Ravichandran G. Three-dimensional full-field measurements of large deformations in soft materials using confocal microscopy and digital volume correlation. Experimental Mechanics. 2007;47(3):427-38.

72. Kammers A, Daly S. Small-scale patterning methods for digital image correlation under scanning electron microscopy. Measurement Science and Technology. 2011;22(12):125501.

73. Kapp M, Hebesberger T, Kolednik O. A micro-level strain analysis of a high-strength dual-phase steel. International Journal of Materials Research. 2011;102(6):687-91.

74. Martin G, Sinclair CW, Poole WJ, Azizi-Alizamini H. Local plastic-strain heterogeneities and their impact on the ductility of Mg. JOM. 2015;67(8):1761-73.

75. Kammers AD, Daly S. Digital image correlation under scanning electron microscopy: methodology and validation. Experimental Mechanics. 2013;53(9):1743-61.

76. Min J, Hector Jr LG, Zhang L, Lin J, Carsley JE, Sun L. Elevated-temperature mechanical stability and transformation behavior of retained austenite in a quenching and partitioning steel. Materials Science and Engineering: A. 2016;673:423-9.

77. Zhao H, Zhu X, Li W, Jin X, Wang L, Jiao H, et al. Austenite stability for quenching and partitioning treated steel revealed by colour tint-etching method. Materials Science and Technology. 2014;30(9):1008-13.

78. Coryell J, Savic V, Hector L, Mishra S. Temperature effects on the deformation and fracture of a quenched-and-partitioned steel. SAE Technical Paper, 2013 0148-7191.

79. Li S, Zou D, Xia C, He J. Effect of strain rate on deformation-induced martensitic transformation of quenching and partitioning steels. steel research international. 2016;87(10):1302-11.

80. Zou D, Li S, He J. Temperature and strain rate dependent deformation induced martensitic transformation and flow behavior of quenching and partitioning steels. Materials Science and Engineering: A. 2017;680:54-63.

81. Creuziger AA, Vaudin MD. Report on VAMAS Round Robin of ISO 13067: Microbeam Analysis—Electron Backscatter Diffraction—Measurement of Average Grain Size. 2011.

82. Poling W, Savic V, Hector L, Sachdev A, Hu X, Devaraj A, et al. Combined synchrotron X-ray diffraction and digital image correlation technique for measurement of austenite transformation with strain in TRIP-assisted steels. SAE Technical Paper, 2016 0148-7191.

83. Hidalgo J, Findley K, Santofimia M. Thermal and mechanical stability of retained austenite surrounded by martensite with different degrees of tempering. Materials Science and Engineering: A. 2017;690:337-47.

84. Marteau J, Haddadi H, Bouvier S. Investigation of strain heterogeneities between grains in ferritic and ferritic-martensitic steels. Experimental Mechanics. 2013;53(3):427-39.

85. Furnémont Q, Kempf M, Jacques P, Göken M, Delannay F. On the measurement of the nanohardness of the constitutive phases of TRIP-assisted multiphase steels. Materials Science and Engineering: A. 2002;328(1-2):26-32.

86. Matsuda H, Mizuno R, Funakawa Y, Seto K, Matsuoka S, Tanaka Y. Effects of auto-tempering behaviour of martensite on mechanical properties of ultra high strength steel sheets. Journal of alloys and compounds. 2013;577:S661-S7.